Inelastic Scattering in STEM for Studying Structural and Electronic Properties of Chalcogenide-Based Semiconductor Nanocrystals

A DISSERTATION SUBMITTED TO THE FACULTY OF THE
GRADUATE SCHOOL OF THE UNIVERSITY OF MINNESOTA
BY

Aloysius Andhika Gunawan

IN PARTIAL FULFILLMENT OF THE REQUIREMENTS FOR THE
DEGREE OF DOCTOR OF PHILOSOPHY.

Advisor: K. Andre Mkhoyan

September, 2013

ACKNOWLEDGEMENT

I thank God for His guidance throughout my ups and downs in the past five years and allowing me to overcome obstacles and meet the right people along the way.

I am very grateful to have Prof. K. Andre Mkhoyan as my adviser. Setting up a new lab forced me to learn a lot from him in the beginning when he himself taught me how to polish TEM samples. His constant availability and approachability have helped me progress effectively in finishing the dissertation. I also learned a lot of valuable science and life lessons from him.

I would like to thank my committee members who provide the time and effort to lead me through the defense process.

I am fortunate to meet Dr. Ozan Ugurlu who practically taught me how to run TEM from the basics. He has been so patient with us who were at times careless with the microscope. I also value our friendship outside the work setting.

I would like to thank the collaborators who have provided samples for me and also exchanged valuable opinions. Dr. Andrew Wills who have been very kind to provide ZnSe samples, Prof. David Norris for advising me on the ZnSe projects, Boris Chernomordik who provided PbSe nanocrystals, Dr. Selin Tosun for the much appreciated opinions on solar cells, and Prof. Eray Aydil who became my secondary adviser along the way. I'd also like to express my gratitude to Dr. Richa Pandey and Prof. Russell Holmes for the collaborative projects on organic materials which I really enjoyed.

I am thankful for working with Mick Thomas and Dr. Earl Kirkland during my visit to Cornell University for experimenting with the aberration-corrected microscope. Dr. Kirkland is also influential in laying the groundwork for the *Multislice* codes which I used to simulate images and further modify myself as part of my projects.

I would like to express special thanks to the whole Mkhoyan group members for creating the unique environment. Anudha Mittal for helping the initial computing setup, Andrew Wagner for being the glorified technician that he likes to call himself, Dr. Jong Seok Jong for his inspiration, Prashant Kumar for the meaningful discussions and badminton, and Michael Odlyzko for the deep conversation about TEM whether it was at the office or gym.

I am grateful for the staffs in the Characterization Facility for providing constant support of guidance and maintenance particularly Dr. Jason Myers.

I thank Dayne Plemmons and Woolim Choi who have helped me as undergraduate researchers.

I would like to express my gratitude for people I have met during my stint at University of Minnesota. Reetam Chakrabarti, Shameek Bose, Tjahjono Tjandra, Andrew Yongky, Han Seung Lee, and Han Zhang.

Lastly, I would like to thank my wife, Sophie, who has supported me throughout these years.

To my family

ABSTRACT

Transmission electron microscopy (TEM) relies upon elastic and inelastic scattering signals to perform imaging and analysis of materials. TEM images typically contain contributions from both types of scattering. The ability to separate the contributions from elastic and inelastic processes individually through energy filter or electron energy loss spectroscopy (EELS) allows unique analysis that is otherwise unachievable. Two prominent types of inelastic scattering probed by EELS, namely plasmon and core-loss excitations, are useful for elucidating structural and electronic properties of chalcogenide-based semiconductor nanocrystals. The elastic scattering, however, is still a critical part of the analysis and used in conjunction with the separated inelastic scattering signals. The capability of TEM operated in scanning mode (STEM) to perform localized atomic length scale analysis also permits the understanding of the nanocrystals unattainable by other techniques.

Despite the pivotal role of inelastic scatterings, their contributions for STEM imaging, particularly high-angle annular dark field STEM (HAADF-STEM), are not completely understood. This is not surprising since it is currently impossible to experimentally separate the inelastic signals contributing to HAADF-STEM images although images obtained under bright-field TEM mode can be analyzed separately from their scattering contributions using energy-filtering devices. In order to circumvent such problem, analysis based on simulation was done. The existing TEM image simulation algorithm called *Multislice* method, however, only accounts for elastic scattering. The existing *Multislice* algorithm was modified to incorporate (bulk or volume) plasmon inelastic scattering. The results were verified based on data from convergent-beam electron diffraction (CBED), electron energy loss spectroscopy (EELS), and HAADF-STEM imaging as well as comparison to experimental data.

Dopant atoms are crucial factors which control optical, electronic, and also magnetic properties of semiconductors. Their location inside the materials has become more important with the miniaturization of devices. The precise determination of the position, however, poses a great challenge. Imaging using HAADF-STEM has proven adequate for locating heavy dopant atoms buried in relatively light matrix, particularly using aberration-corrected microscopes. The imaging method has been unsuccessful in detecting dopant atoms with similar atomic number as the matrix. Inelastic core-loss or inner-shell electronic excitations using EELS offer a unique solution when simultaneous imaging and EELS acquisitions are performed. The dopant atoms that are invisible in the images due to the small atomic number differences can be detected via spatial correlation with EELS core-loss data. Three types of samples with varying concentration of Mn dopant atoms in ZnSe nanocrystals were used to confirm such method. Precise locations of the dopant atoms on planes perpendicular to electron beam propagation could be determined although not all of the dopant atoms were detected due to limitations in experimental conditions.

Another important type of chalcogenide-based nanocrystals is PbSe which is useful for solar cells. Colloidal method commonly used to synthesize the nanocrystals leave oleic acid capping ligands as surface passivation and size stabilizer. These ligands have critical roles in controlling electrical and optical properties of an individual nanocrystal and their assembly. Deemed insulating due to long chains of carbons, oleic acid is typically treated with short ligands such as hydrazines to decrease the inter-nanocrystal distances and improve electronic coupling among the neighboring nanocrystals.

Despite its apparent insulating behavior, oleic acid was shown to exhibit surface plasmon coupling under certain circumstances. The geometric arrangement of the ligands was first investigated by HAADF-STEM imaging. Under air exposure, PbSe nanocyrstals easily oxidize to form oxide shells that are responsible for p-type doping by introducing surface acceptor states. At early

oxidation stage (partial oxidation), prior to the formation of uniform oxide shells, the nanocrystals appear to form links between neighbors. Localized EELS analysis shows that these links are made of carbon based materials, most likely modified form of oleic acid ligands consisting of conjugated double bonds. Such modification occurred through oxidative dehydrogenation of the oleic acid ligands that is facilitated by the growing oxide shells on the surface of nanocrystals.

CONTENTS

LIST OF TABLES

LIST OF FIGURES

1

Introduction

1.1 Transmission Electron Microscopy (TEM) as Atomic Scale Analytical Tools

Numerous research fields have benefited from the invention of TEM. The capability of TEM to look at nanometer and atomic length scale has advanced physical sciences such as the understanding of thin film interfaces in electronics,[1-6] mechanical[7-11] and electrical failure analysis,[12-16] as well as magnetic domains.[17-21] The field of spintronics will also be significantly affected by the latest ability to control the electron spin polarization in TEM.[22] TEM has also helped the life science community particularly through 3-D reconstruction of objects (such as virus) using tomography,[23-27] forensic analysis,[28-31] and medical purposes.[32-35] Geology and metallurgy are other areas aided by TEM.[36-42]

In its simplest application, TEM is used to take images of the samples much like having an X-ray medical check-up. A lot could be obtained from those images such as the determinations of sizes, shapes, and defects. However, two advancements transform TEM to become more powerful. The first is the integration of electron energy loss spectroscopy (EELS) and energy dispersive X-ray (EDX) to perform simultaneous imaging and spectroscopy analysis and secondly the invention of aberration-corrected microscopy to push the resolution down to sub-Å. The current state-of-the-art TEM allows one to perform analytical investigations down to a single atom. It is still unknown as to what limit analytical TEM can achieve. Ongoing research on imaging bonding orbitals[43-45] and *in-situ* TEM[46-51] will surely test the limit.

1.2 Importance of Inelastic Scatterings in TEM

When electron beam passes through materials, a number of phenomena can occur. They can be classified as elastic and inelastic scattering. Elastic scattering, originating from coulomb interactions, is most useful for image formation. Inelastic scattering, on the other hand, is useful for various different purposes other than imaging although at times could be problematic. Phonon inelastic scattering is known to produce Kikuchi lines useful for understanding crystal orientation.[52, 53] Core-loss excitation in EELS and EDX, which are localized to within the atoms,[54] are advantageous for determining the elemental distributions in the samples. Plasmon inelastic scattering can be used to determine the thickness of the samples[55-57] and, as I will show in this dissertation, plasmon scattering can be useful for probing interaction or coupling in the samples as the signals are delocalized. The only downside of inelastic scattering is sample damage by radiolysis and knock-on scattering,[58-62] which can limit the duration of analysis by electron beams at specific locations.

1.3 Chalcogenide-Based Semiconductor Nanocrystals

As important as the TEM to microscopists, it is equally critical to have the right materials to study. In order to understand the many usage of inelastic scattering in TEM, I chose to analyze chalcogenide-based semiconductor nanocrystals. More specifically, Mn doped ZnSe nanocrystals were used to study the core-loss imaging of 'invisible' dopant atoms. ZnSe nanocrystals have found applications in dilute magnetic semiconductors,[63-67] whereby the number and locations of dopant atoms are critical components of the electronic properties of the nanocrystals.[68-73] The properties of the Mn doped ZnSe nanocrystals have also been rigorously studied using different synthesis and experimental techniques.[74-78] Another type of chalcogenide-based semiconductors that I used is PbSe nanocrystals, which are used for infrared emitters[79-81] and solar cells applications.[82-85] One of the main properties of PbSe nanocrystals that are

exploited in this dissertation is their tendency to form electronic coupling under close separation distances.[86, 87] This manifests in the understanding of a new plasmonic interaction in the ensembles of these nanocrystals.

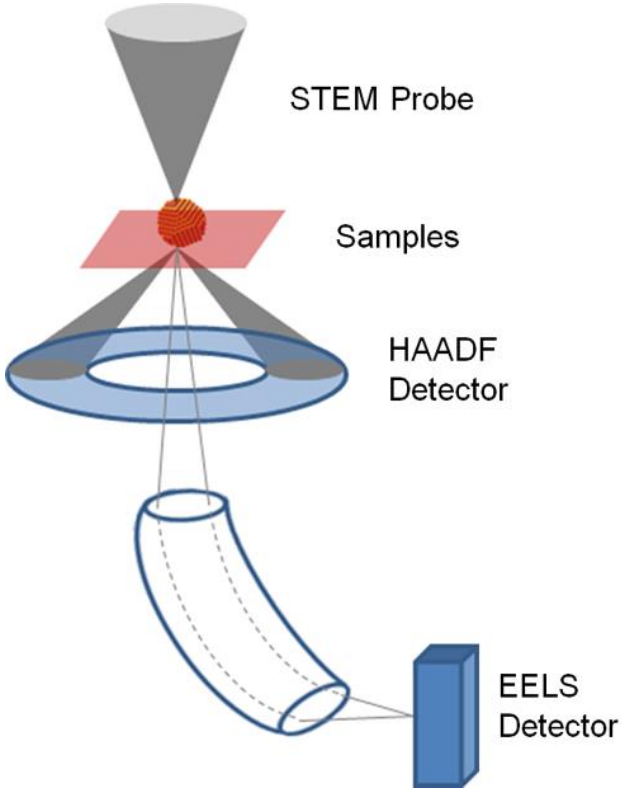

Figure 1.1. Schematic illustration of TEM operated in scanning mode (STEM) for analyzing nanocrystals. The high-angle scattered electrons exiting the samples are used to form high-angle annular dark-field STEM (HAADF-STEM) images. The electron scattered at low angles can be used to form bright-filed TEM images but in here are shown to form EELS spectra after passing through magnetic prism to differentiate based on the amount of energy lost.

1.4 Thesis Overview

The central topic of my dissertation is the use of inelastic scattering to understand various aspects of chalcogenide-based nanocrystals. Core-loss and plasmon scattering are used to characterize the dopant atoms in ZnSe and plasmonic interactions in PbSe nanocrystals. Deeper understanding of the

contribution of plasmon scattering to TEM imaging is also made via modifications of the *Multislice* simulation method.

Chapter 2 gives the background on the TEM instruments used throughout the dissertations. First, the fundamental concept of conventional TEM (CTEM) imaging is discussed. Subsequently, an alternative to the CTEM mode called scanning transmission electron microscopy (STEM) is discussed. STEM technique is actually critical in performing simultaneous imaging and spectroscopic analysis as it allows the collection of image signal using annular detector and spectroscopic signals through the central detector. The concept of EELS is described particularly on how the instrumentation is integrated and signals detectable under typical collection experiments. The chapter is closed with the discussion on aberration corrected TEM. The main modification of aberration corrected TEM is the incorporation of correctors consisting of multipole lenses to cancel out the spherical aberration introduced by the objective lenses. The improved resolution of the TEM can be used to resolve spatial resolution down to 0.6 Å.

Chapter 3 describes the types of inelastic scattering particularly useful for the dissertation. It starts with the discussions of bulk or volume plasmon, which is the most probable type of inelastic scattering in EELS. The theory of bulk plasmon based on free electron gas approximation is derived. The characteristic cross section and plasmon dispersions are also discussed before the concept of bulk plasmon in semiconductors (not completely free electrons) is described. Surface plasmon, another type of electron oscillations, is the subject of the subsequent discussion specifically on the surface plasmon modes on nanoparticles. The origin of surface plasmon and the conditions of exciting the resonant oscillations are defined. The sources of dephasing or decay for plasmon are important as they have implications on the width of the plasmon spectra as observed in EELS. Plasmon dephasing concept is also used to understand plasmonic and electronic interactions in PbSe nanocrystals (Chapter 6). Types of

plasmonic interactions involve dipolar, tunneling, and charge transfer coupling. Each is discussed based on the implications on the spectra. The chapter is closed with the discussions on core-loss excitations using EELS, which is the key to the topic of imaging invisible dopant atoms in Chapter 5.

Chapter 4 describes the incorporation of plasmon inelastic scattering into the *Multislice* image simulation algorithm. I decided to put this chapter preceding the other chapters on my research results as it allows me to describe the STEM image formation in a great mathematical details pertaining to the algorithm. The existing algorithm is then discussed, which is based solely on elastic scattering. The modified algorithm incorporating plasmon scattering is outlined and comparisons with experimental data are made particularly based on the simulated EELS spectra, convergent beam diffraction patterns (CBED), and STEM images. The effects on the contrast of simulated images of various materials are investigated. The relation with Stobbs factor, which is responsible for explaining the contrast difference in simulated and experimental TEM images is also made. The content of this chapter has also been prepared for publications titled "Incorporating Plasmon Inelastic Scattering in *Multislice* Image Simulation".

Chapter 5 discusses the technique of using core-loss signal for imaging 'invisible' dopant atoms. Dopant atom imaging using HAADF-STEM typically relies on the large difference between the atomic number of the dopant atoms and the host, such as Sb in Si and Y in Al_2O_3. For dopant atoms with similar or lower atomic numbers than the hosts, performing HAADF-STEM imaging alone is insufficient to detect the impurities. Simultaneous HAADF-STEM imaging and core-loss correlation can circumvent such problems as shown for Mn (Z = 25) doped ZnSe (Z_{ave} = 32) nanocrystals. Three different types of samples were analyzed: undoped, singly doped, and heavily doped ZnSe:Mn nanocrystals. Statistical limits of the experiments were calculated and the results were explained in terms of the simulated profiles of STEM beam propagation in the

nanocrystals. Conditions that enhance the probability of dopant detections are also discussed. This includes the choice of the EELS core-loss edge, size or thickness of materials, accelerating voltage, beam scanning dwell time, pixel sizes, and locations of dopant atoms.

Chapter 6 is devoted to the discussions of plasmonic interaction through the changes in the chemical bonds of oleic acid ligands on PbSe nanocrystals. It begins with the understanding of geometric arrangements of ligands on the surface of lead chalcogenide nanocrystals using HAADF-STEM imaging. This is the first such report on the effort to image the geometric conformation of ligands experimentally. Low-loss and core-loss EELS analysis on the surface ligands further elucidate plasmonic interactions supported by the modified ligand chemical bonds. The plasmonic interaction is tightly related to the electronic coupling exhibited by the high dielectric materials such as PbSe. The plasmonic interaction through modified chemical bonds is explained in terms of oxidative dehydrogenation mechanism, which is partly understood based on the study of ligand orientation.

2

The TEM Instruments

This chapter gives an overview of the concepts and instruments that have helped me complete my dissertations. We start with the discussions on conventional transmission electron microscopy before describing the difference from scanning transmission electron microscopy. A section about electron energy loss spectroscopy is to follow before closing the chapter with the descriptions of aberration-corrected transmission electron microscopy as the current state-of-the-art microscopy for sub-Å resolution.

2.1. Conventional Transmission Electron Microscopy (CTEM)

The birth of TEM occurred at the beginning of 20th century around the same time when the wave characteristics of electrons were under heavy investigations. It was suggested that the resolution limit of light microscopes could be improved by the use of the smaller electron wavelengths. Scientists, however, were unsure how to focus the electrons hence the idea of electron microscope was yet to be realized. In 1932, Knoll and Ruska made a breakthrough by developing the first electron lenses.[88] A few years later, the first TEM was developed in UK that paved the way for the successive improvements of TEM machines until the present time. [89]

The imaging modes of TEM employ coherent electron beams that interact with the samples to form images. It is often referred as conventional TEM (CTEM) to distinguish from another mode of imaging called scanning transmission electron microscopy (STEM), which is discussed in Section 2.2.

2.1.1 Illumination System

The typical ray diagram of the TEM illumination system before passing through the samples is shown in Figure 2.1a. The electron beam emanating from the sources, or the gun systems, is brought into crossover at the back focal plane of the condenser 1 (C1) lens to produce a demagnified image of the source. C2 lens brings the electron into another crossover for further demagnification. The C2 diaphragm or aperture is used to control the convergence angle (α) of the incident beam on the specimen and a critical component in determining the image resolution of CTEM operation. Note that the beam is relatively parallel as the value of α is in the order of 0.1 mrad or 0.006°.

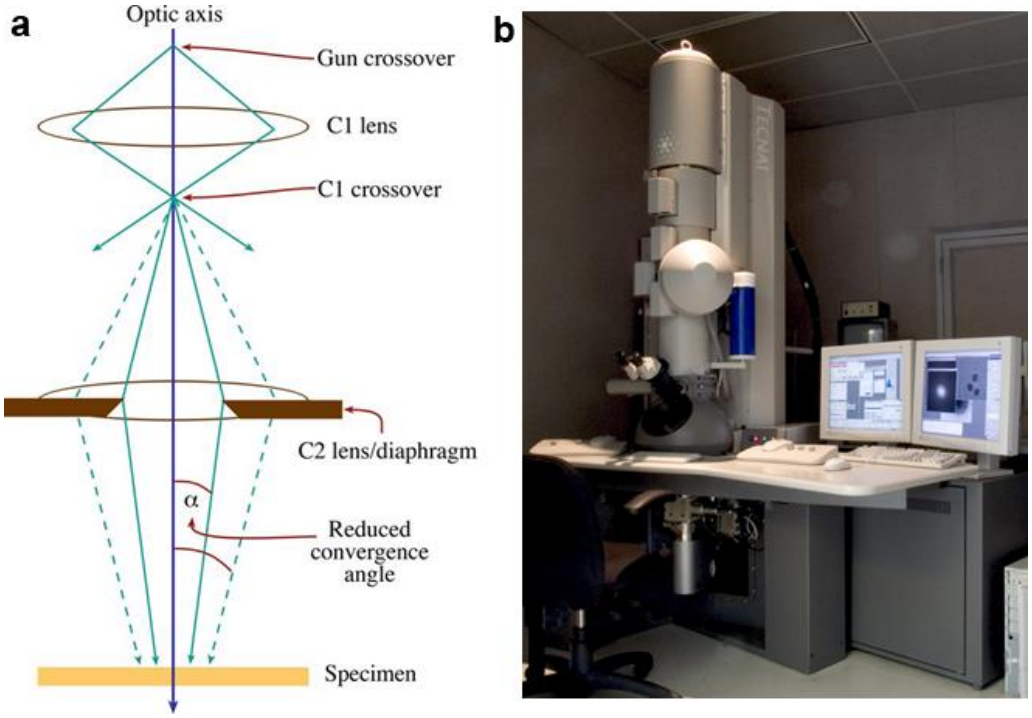

Figure 2.1. (a) Schematic ray diagrams for CTEM illumination system incident on the specimen. C1 is utilized to produce the demagnified image of the source and the effect different C2 size on the convergence angle $\boldsymbol{\alpha}$ is shown (dotted lines).[89] (b) FEI Tecnai T-12 instrument located at the University of Minnesota Characterization Facility capable of CTEM imaging up to 120 kV accelerating voltage.[90]

The TEM at University of Minnesota used mainly for CTEM operation is shown in Figure 2.1b. It is an FEI Tecnai T-12 model equipped with LaB_6 thermionic emission gun source. The resolution limit of the instrument is about 3.4 Å making it unsuitable for very high resolution TEM work. It, however, serves well for initial training purposes and quick TEM experiment such as size verifications and elemental determination as it is also equipped with Energy Dispersive X-rays (EDX).

2.1.2 Imaging System

The imaging system refers to the paths of electron beams after passing through the specimens. In principle, there can only be two types of electron beam propagation in CTEM: forming diffraction patterns or images. The diffraction patterns, or more commonly known as selected area diffraction (SAD), are formed by spreading the beam illumination to a wide area on the samples as shown in the left-panel of Figure 2.2. The back focal plane of the objective lens is used as the object for the intermediate lens so that the focused electrons are imaged on the screen forming the dot-like feature of SAD patterns such as shown in Figure 2.3b.

The process of image formation in CTEM is shown in the right panel of Figure 2.2. The beam propagation for CTEM imaging mimics that of the SAD up to the intermediate lens. However, as opposed to SAD mode, the strength of the intermediate lens is adjusted such that the image plane of the objective lens is used as the object planes to form final images on the viewing screen. Figure 2.3a shows typical high resolution CTEM images.

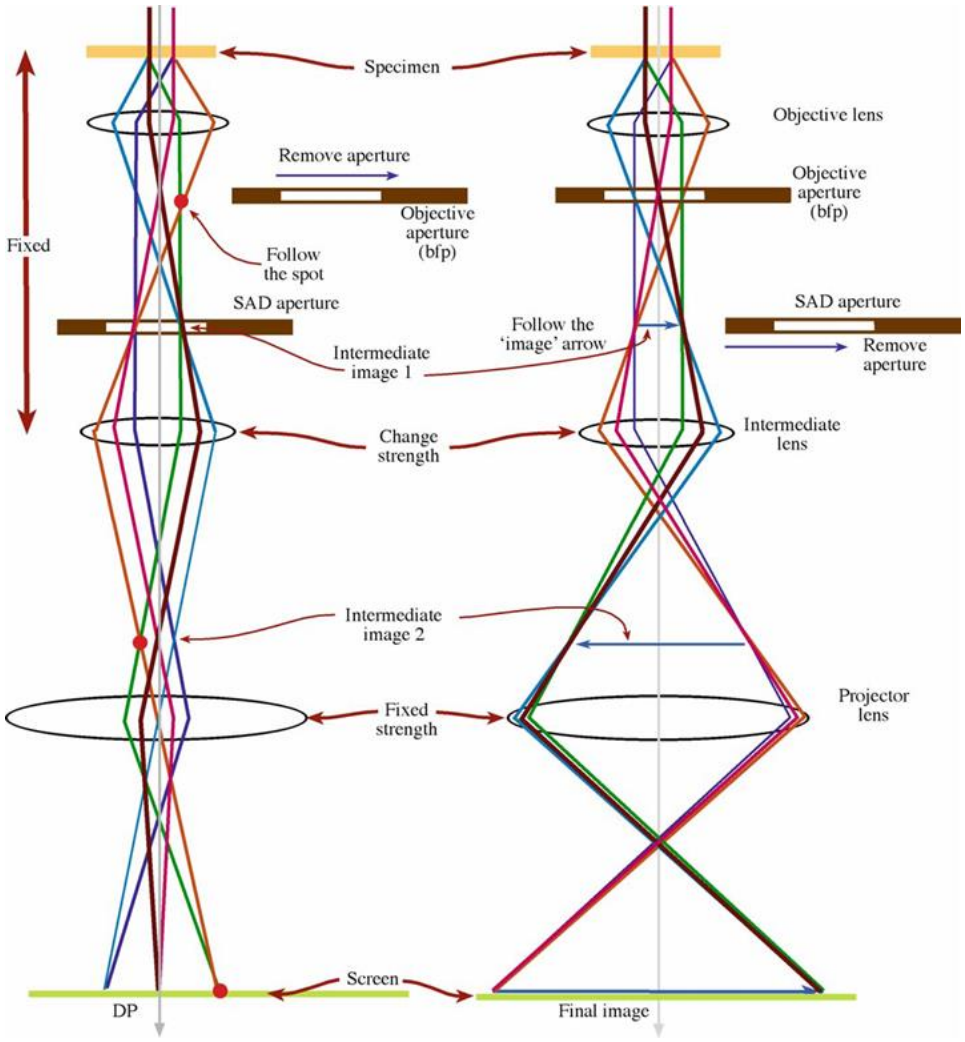

Figure 2.2. Ray diagrams after passing through specimen for CTEM operation in diffraction (left-panel) and bright-field (right-panel) imaging modes. In both cases, the paths of electron beams are identical until encountering the intermediate lens. In diffraction mode, the intermediate lens uses the back focal plane of the objective lens as the object while imaging mode uses the image plane of the objective lens.[89]

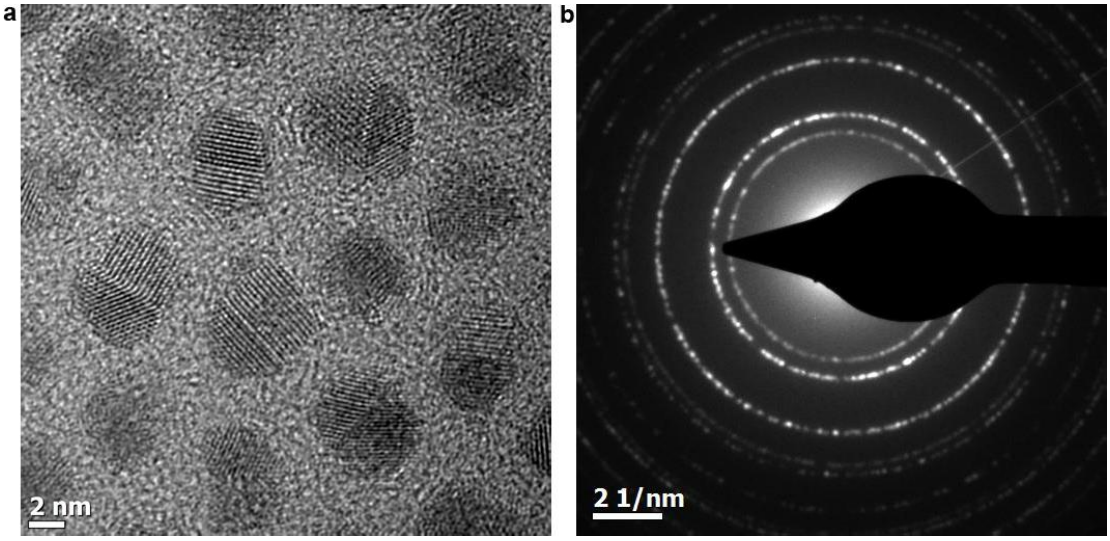

Figure 2.3. (a) High resolution CTEM image of PbSe nanocrystals and (b) the corresponding SAD patterns.

2.1.3 Aberration

We have thus far neglected the discussion about lens aberration, which is a lingering problem in electron microscopy that prevents a sub-Å resolution ideally achievable with the typical electron wavelength of fast electrons in the order of 0.01 Å. Figure 2.4a shows the effect of spherical aberration introduced by the (electromagnetic) lens on the propagating electron waves. The electrons passing through the edge of the lens are more strongly focused than the ones passing closer to the center, which produces a spreading of the focused points and hence lowering the resolution. The aberration induces an error on the propagating wavefronts in the value of δ resulting in the phase deviation of $\chi = (2\pi/\lambda)\delta$.

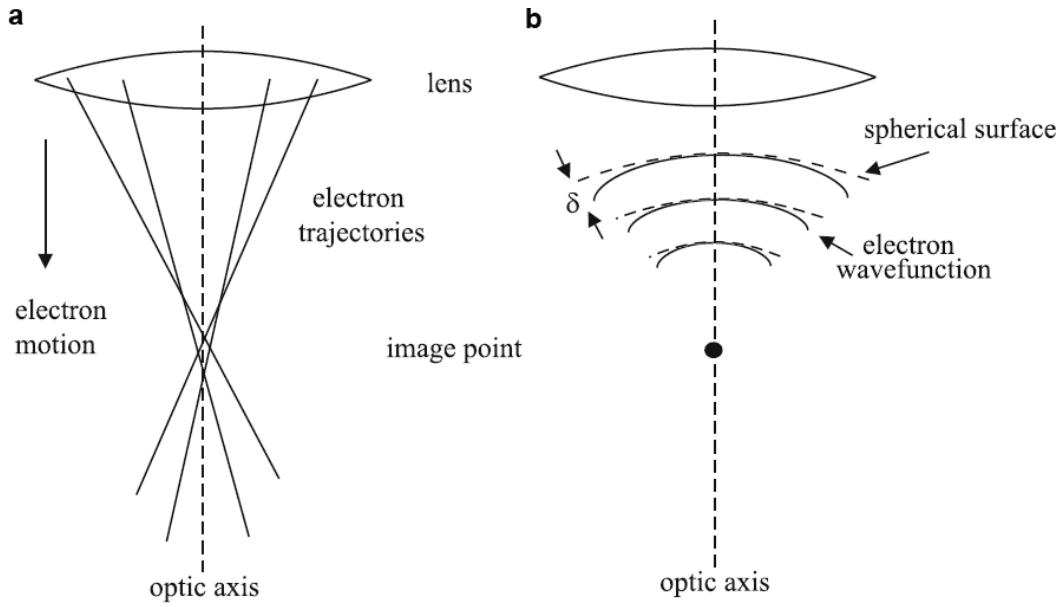

Figure 2.4. The effects of lens spherical aberration on the focusing of electron beams. In (a) real space, the spherical aberration alters the trajectories by focusing electrons traveling close to the edges of the lens more strongly than those passing near the center of the lens. (b) In the reciprocal space, the electron wavefunction can be thought as having different phases radially due to the different focusing strength of the lens. The phase error is referred to as $\boldsymbol{\chi}$.[91]

The phase error χ, better known as the aberration function, can be expanded in terms of the angular deviations from the optic axis (α_x, α_y) as[91]

$$\chi = \frac{2\pi}{\lambda}\delta = \frac{2\pi}{\lambda}\left(\frac{1}{2}C_1\alpha^2 + \frac{1}{4}C_3\alpha^4 + \frac{1}{6}C_5\alpha^6 + \cdots\right), \tag{2.1}$$

where $\alpha = \sqrt{\alpha_x^2 + \alpha_y^2}$ is the convergence angle in Figure 2.1a, $C_1$is the defocus of the lens characterizing the strength of the current running through lens, C_3 is the third-order spherical aberration coefficient better known as C_S, and C_5 is the fifth-order spherical aberration coefficient. While operating TEM, a user needs to minimize the aberration function (2.1) by selecting the appropriate defocus value C_1 at a given aperture size. The use of C2 can be thought of limiting the amount of overfocused electrons that contribute to the spreading of the focused points.

2.1.4 Contrast Transfer Functions

The effect of aberration function is to introduce modulation in the spatial frequency of the wavefunction through the phase shift relation[91]

$$H_O(K) = \exp[-\mathrm{i}\chi(K)] = \cos[-\chi(K)] - \mathrm{i}\sin[-\chi(K)], \qquad (2.2)$$

where we have used $\alpha = \lambda k$ and $K = k(C_S\lambda^3)^{1/4}$ is the normalized or dimensionless number for the angles to express (2.2). $H_O(K)$ is also known as modulation transfer function or contrast transfer functions (CTF) as it tells how the objective lens transfers the information regarding spatial frequency of the wavefunction after it passes through the samples and before the final image is collected. Figure 2.5 shows typical CTF for 200 kV accelerating voltage and 1 mm spherical aberration for two different defocus values. There are significant oscillations about the zero level particularly for higher spatial frequencies, which means that some parts of the wavefunctions carrying the crystal spacing information in the sample are transferred as black if $H_O(K) < 0$ and white if $H_O(K) > 0$. Consequently, the lattice fringes of the high resolution TEM images in Figure 2.3b do not necessarily tell where the exact atomic locations are. This is a disadvantage of CTEM operation that sometimes limits the capabilities to detailed atomic analysis such as detecting dopant atoms.

2.2 Scanning Transmission Electron Microscopy (STEM)

The first effort to build STEM was done by Manfred von Ardenne in 1937-1938, not long after the invention of TEM in 1934.[92] While TEM was built to improve the spatial resolution of light microscopes, STEM was initially developed to make scanning electron microscopes (SEM). For that reason, STEM

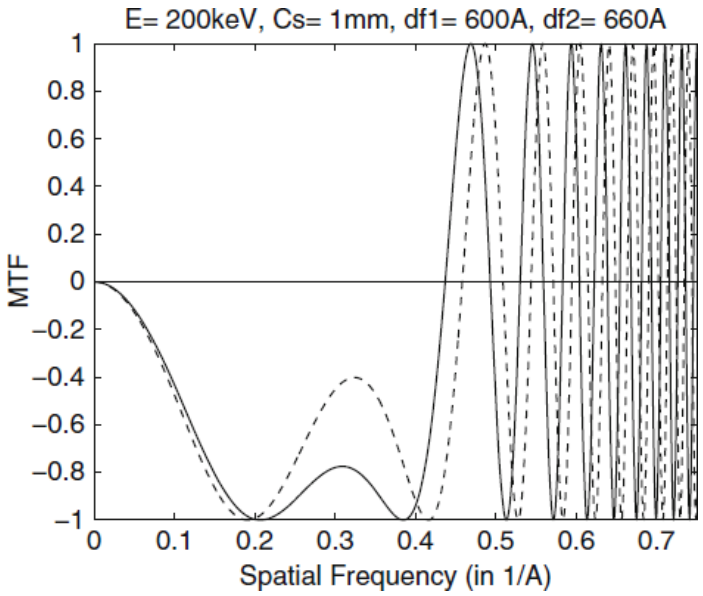

Figure 2.5. The modulation transfer function for 200 keV accelerating voltage and 1 mm spherical aberration coefficient. The effects of different defocus values are shown. Note that perfect coherence is assumed in calculating these transfer functions. Actual transfer functions have incoherence (the beam is never fully coherent) which affects the amplitude and phase of the CTF as shown in Figure 2.10.[91]

had a considerably lower spatial resolution of 40 nm in its early development than TEM. The use of thermionic sources STEM contributed to such poor resolution although it does not prevent TEM from achieving high spatial resolution. It was not until decades later than using field-emission gun as the source could improve the spatial resolution of STEM along with the improved understanding of the STEM detectors and lens.

2.2.1 Probe in STEM

If TEM utilizes wide area coherent illumination of electron beam on the sample as shown in Figure 2.1a, STEM imaging principle necessitates the formation incoherent focused electrons called the probe. The strength of C2 lens is adjusted so that the electrons form an image of the C1 crossover on the sample such as shown in Figure 2.6a.[89] This also can be thought as the image of the

source size that has been demagnified twice. Hence, the choice of the gun type is even more critical in STEM since it defines the probe size on the specimen. A detailed mathematical treatment of probe formation in STEM is given in Chapter 4.

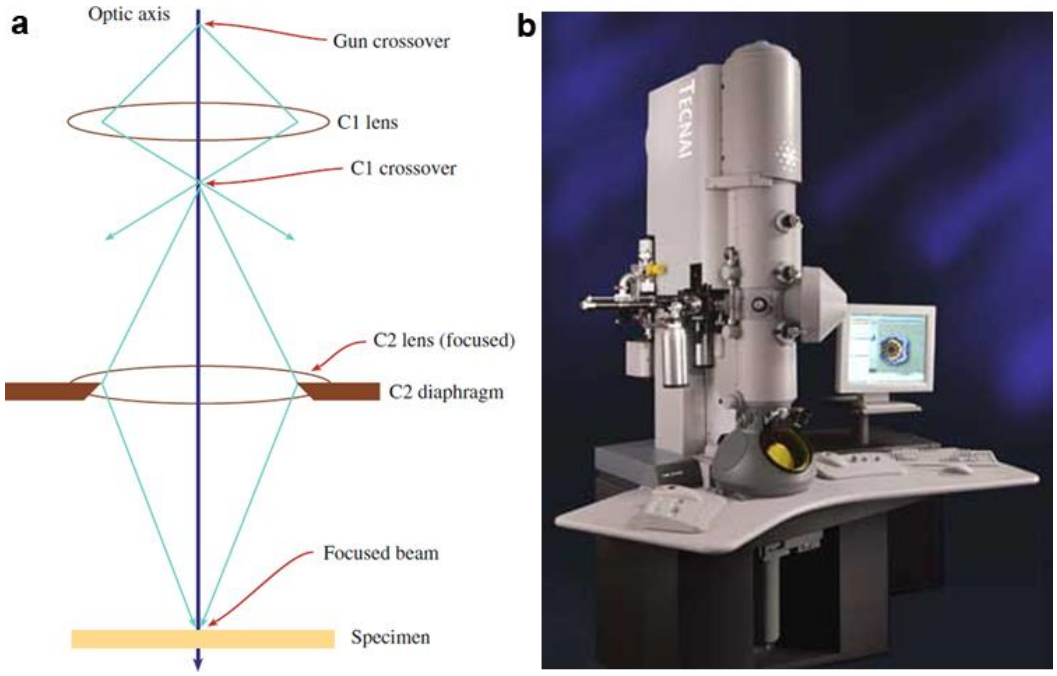

Figure 2.6. (a) Schematic illustration of the formation of focused probe for STEM imaging purposes. The strength of C2 lens is adjusted to form converged beam on the specimen the C2 aperture is used to control the convergence angle of the electron beams.[89] (b) The FEI Tecnai G2 F30 instrument at the University of Minnesota Characterization Facility capable of performing TEM operation both in CTEM and STEM mode.

The STEM at the University of Minnesota is FEI Tecnai G2 F30 (Figure 2.6b). It has capabilities of performing both CTEM and STEM imaging mode by adjusting the focusing strengths of the appropriate lenses. One of the main differences from the CTEM-only FEI Tecnai T12 (Figure 2.1b) is the use of Schottky-field-emission gun (FEG) instead of the thermionic as its sources. The first gun crossover before passing through C1 can reach down to 3 nm in the case of FEG sources, which is better than 10 μm crossover size typically

achievable using thermionic sources. Figure 2.7 shows the images of LaB6 and tungsten filament used for thermionic and Schottky-FEG sources respectively. It is clear that the tungsten needle forms a fine electron sources necessary for high-resolution STEM imaging.

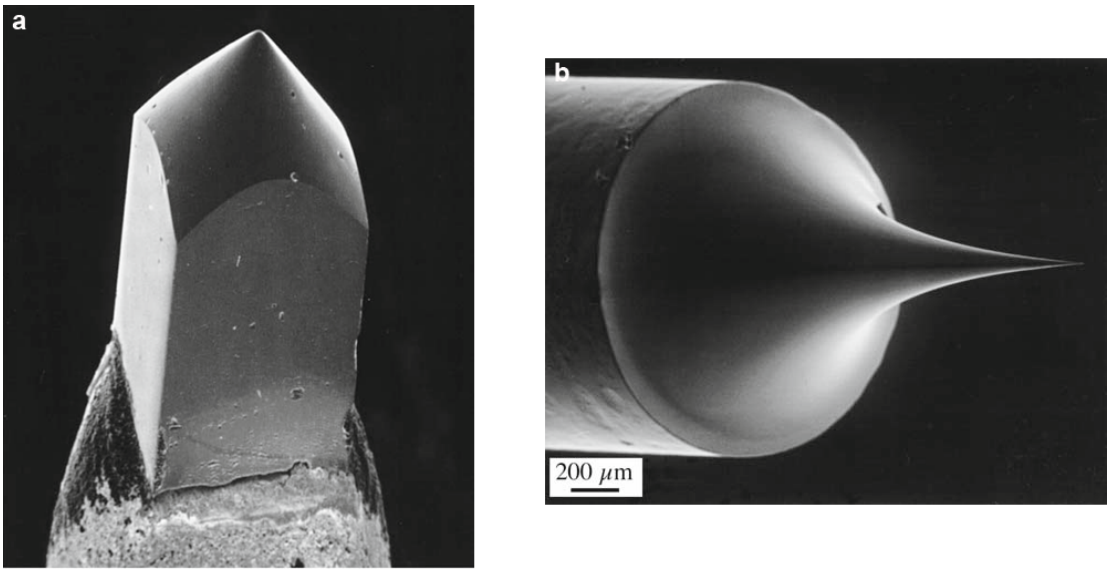

Figure 2.7. Images of electron source from (a) LaB6 and (b) tungsten needle. LaB6 filament is usually for thermionic emission and the fine tungsten needle is for Schottky-FEG.[89]

2.2.2 STEM Imaging

The principle of STEM imaging involves the scanning of the probe over the desired areas on the samples. The transmitted electron intensity is recorded as a function of scanning position on the detector, which is then used to create the STEM images. STEM imaging is a serial process making it fundamentally different from the parallel acquisition in the CTEM counterpart. Figure 2.8 illustrates the scanning process of the STEM probe incident on two different points on the specimens. Unlike in SEM where the pivot point is on or near the sample surface, the scan coils – lens systems in STEM are assembled to have the pivot point after the objective lens. Such conditions enable the probe to be

focused at the same angle with respect to the optic axis for different locations. A tilted probe found in STEM can result in unintended intensity variation recorded in the detector arising not from the specimens. This may not be an issue in SEM whereby the artifacts induced by tilted scanning beam are negligible compared to the signal variations obtained from the sample surfaces.

The STEM imaging modes can be classifieds into bright-field (BF) and annular dark-field (ADF) imaging. In the case of BF-STEM, we mainly use the direct unscattered beams much like in the case of CTEM (Figure 2.9a) by inserting circular electron detectors centered on the optic axis. The image contrast thus mimics that of CTEM images, whereby the specimens (Au islands) look darker than the vacuum (top right in Figure 2.9b). In the first few decades of its invention, STEM imaging adopted the BF mode and the resolution was not necessarily better than CTEM. It was not until 1970's that ADF-STEM imaging was realized and heavily researched.[93, 94] By using the elastically scattered electrons exiting at high angles, images are acquired by incoherently integrating the intensity of electrons incident at particular angles (typically 54-300 mrad). Figure 2.9c shows the image of the same Au islands collected using ADF-STEM. Detailed mathematical treatments of ADF-STEM imaging are given in Chapter 4. The ADF-STEM images are often referred as *Z*-contrast images since the elastic scattering intensity depends on powers of the atomic number such as found in Rutherford scattering $I \sim Z^2$.

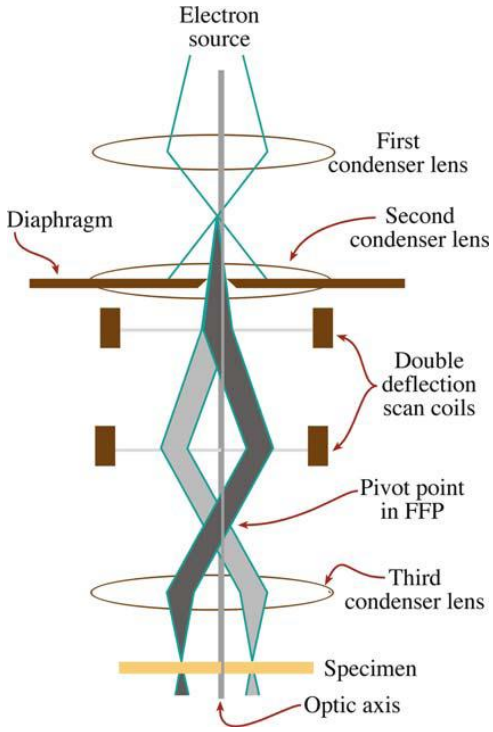

Figure 2.8. Schematic illustration of probe scanning mechanism in STEM mode. The scan coils are responsible for the deflections of the probe to avoid the tilting of the focused beam on the specimen.[89]

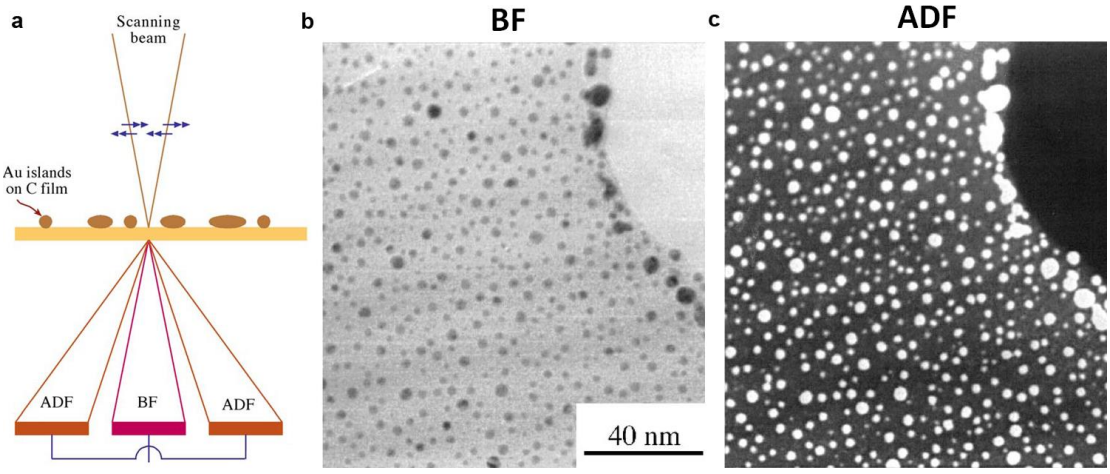

Figure 2.9. (a) Schematic illustration of STEM image formation. The probe is scanned over the specimen and the transmitted electrons are collected by the central detector to form (b) BF image. Electrons scattered at higher angles are used to form (c) ADF image. The signal of BF is complementary of the ADF signals. [89]

2.2.3 STEM Contrast Transfer Functions

The contrast transfer functions of ADF-STEM can be calculated similar to (2.2) and the plot is compared with CTEM transfer function in Figure 2.10.[91] One distinct behavior is that the transfer functions of ADF-STEM are positive for wider frequencies. This is due to the fact that any coherence in the incident electron is disrupted due to the formation of focused probes. As a result, the intensity of ADF-STEM signals should better convey information regarding atomic positions of the specimens since the transmitted electrons are incoherent. However, obtaining high-resolution ADF-STEM images is relatively more difficult since the probe size has to be smaller than typical atomic separation (1-3 Å).

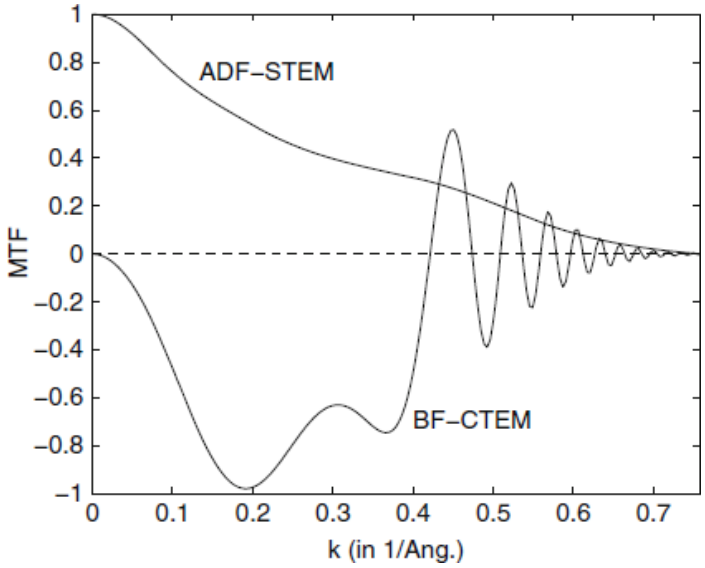

Figure 2.10. A comparison of modulation transfer functions for CTEM and ADF-STEM where partial incoherence is incorporated. It is obvious that ADF-STEM transfers information less ambiguously since the signal intensity is not highly modulated around 0 compared to CTEM transfer function in the calculated range.[91]

2.3. Electron Energy Loss Spectroscopy (EELS)

The development of EELS started in the late 1920's when Rudberg performed measurement of the kinetic energy of electrons reflected from the surface of metals.[95] While the resolution is relatively low in the order of 1 eV, the work started a new field of glancing-angle reflected EELS (REELS). The energy resolution was subsequently improved to reach the meV range, which was possible since surface technique typically requires low energy voltage beam (< 20 keV), and hence lower chromatic aberration or energy spread. REELS system is commonly attached to SEM or molecular beam epitaxy (MBE) chambers as means to perform elemental analysis. This dissertation, however, does not focus on the surface mode of EELS but rather the transmitted EELS mode attached to TEM.[95]

The first work of operating EELS in transmission mode was done in 1941 by Rutherman on thin film Al.[96] He observed a series of peaks having multiplicity of 16 eV, which was later determined to be the bulk plasmon signals of Al. Elemental analysis obtained from inner-shell excitations were later realized on nitrocellulose samples. However, since transmission EELS requires higher incident energy in the order of tens and hundreds of keV, the energy resolution is limited to about 0.7 eV much worse than typical optical experiments and REELS. The use of monochromator has circumvented this problem bringing the energy resolution down to tens of meV.

2.3.1 Magnetic Prisms

The imaging mechanisms of CTEM and STEM discussed in Sections 2.1 and 2.2 utilize electrons that are elastically scattered through Coulomb interactions with atomic nuclei, and hence maintain the same energy before passing through the specimens. EELS signals, on the other hand, are comprised of scattered electrons that have lost some energies through inelastic interactions with specimens such as plasmons and inner-shell excitations. As a consequence,

the critical part of EELS instrumentations is magnetic prism that separates electrons with different energies.

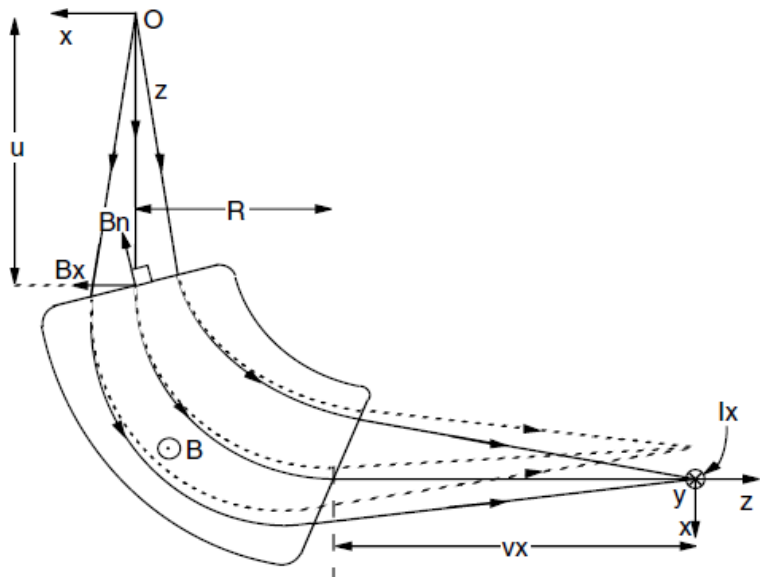

Figure 2.11. The trajectories of electrons passing though the magnetic prism. The electrons that have lost more energy or slower are bent more inward or have smaller curvatures. The prism is also equipped with a focusing capability to generate the EELS spectra on the CCD detector.[95]

The concept of magnetic prisms is illustrated in Figure 2.11. The transmitted electrons propagate along the z-axis with speed v and the magnetic field is in the y-direction. The electrons experience Lorentz force within this magnetic field and travel in a circular motion within the prism. The radius of curvature (R) of the bending electrons is

$$R = \left(\frac{\gamma m_o}{eB}\right) v \qquad (2.3)$$

where γ is the relativistic factor, m_o is the rest mass of electrons, e is the electronic charge, and B is the magnitude of the magnetic field. The electrons that have not lost energies, whether unscattered or elastically scattered, travel

the fastest and hence have the largest radius of curvature. Those that have lost larger energies travel slower and are focused on different spots on the detector.

2.3.2 The Spectrum

Typical EELS spectrum is shown in Figure 2.12 for a high temperature superconductor $YBa_2Cu_3O_7$ in logarithmic scale.[95] The largest signal and zero energy loss is the unscattered and elastically scattered electrons. The energy resolution is obtained from the FWHM of this peak. The broad peaks commonly observed in the range of 6-30 eV energy loss can be attributed to plasmon excitations. This arises due to the collective oscillations of the electrons in the valence bands of the specimens. Chapter 3 is dedicated to the discussions about plasmon since it is central to my dissertation.

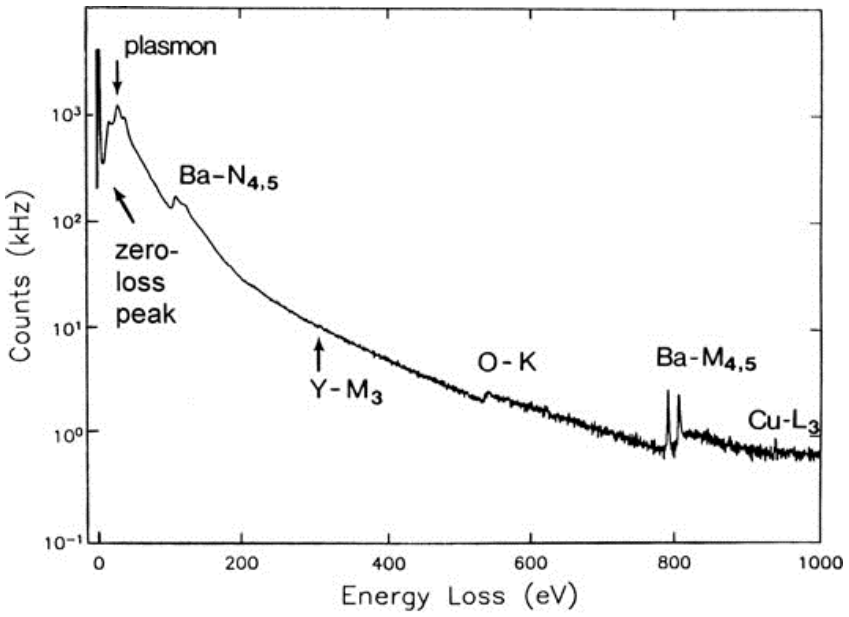

Figure 2.12. An EELS spectrum of a high temperature superconductor $YBa_2Cu_3O_7$ showing three main regions: (i) zero-loss that contains unscattered and elastically scattered electrons, (ii) plasmon loss, and(iii) core-loss excitations labeled with the nomenclature explained in the text. It is put in logarithmic scale to emphasize the relative intensity from each type of excitations.[95]

At higher energy loss, one usually observes inner-shell or core-loss excitations that come from the energy lost due to exciting electrons from inner-shell orbitals to empty states above the Fermi level. The nomenclature of core-loss follows X_i, where X is the principal quantum number the shell is located (K for n=1, L for n=2, …) and i is the associated with the spin-orbit quantum number j. Hence, O-K signal in Figure 2.12 arises from electron excitation in shell n=1, l=0, and j=1/2, while Ba-$M_{4,5}$ originates from excitations in shell n=3, l=2, j=3/2 and 5/2. Generally, the deeper the shells the higher the energy loss and the lower the excitation probability is. Note that the intensity of core-loss is lower than the plasmon loss.

2.3.3. Energy Filtered TEM (EFTEM)

The development of magnetic prisms for EELS experiments reached a new direction in 1960's with the invention of energy selecting prism to allow imaging using certain range of energy losses.[95] The first type of energy filter prism uses the combination of mirror and filter to induce the dispersive and focusing capability of the system to form images (Figure 2.13a). Another type of energy filter is the omega-filter as shown in Figure 2.13b, which is more commonly employed in the present. It consists only of magnetic prisms without mirrors and each prism introduces dispersion on the electron trajectory based on the velocity or the amount of energy loss. The electron path follows an omega trajectory, hence the name, to preserve the alignment of the electron beam passing through the optic axis. An energy slit is inserted on plane D2 (see Figure 2.13b) to select the desired energy loss range used to form images.

There is a plethora of applications of EFTEM imaging in the physical and biological sciences. This technique can see the distributions of elemental maps by collecting the images from each core-shell energy loss associated with each element (see Figure 2.12). One of the applications is to observe the elemental distributions in transistor stacks as shown in Figure 2.14.[97] The locations of Si

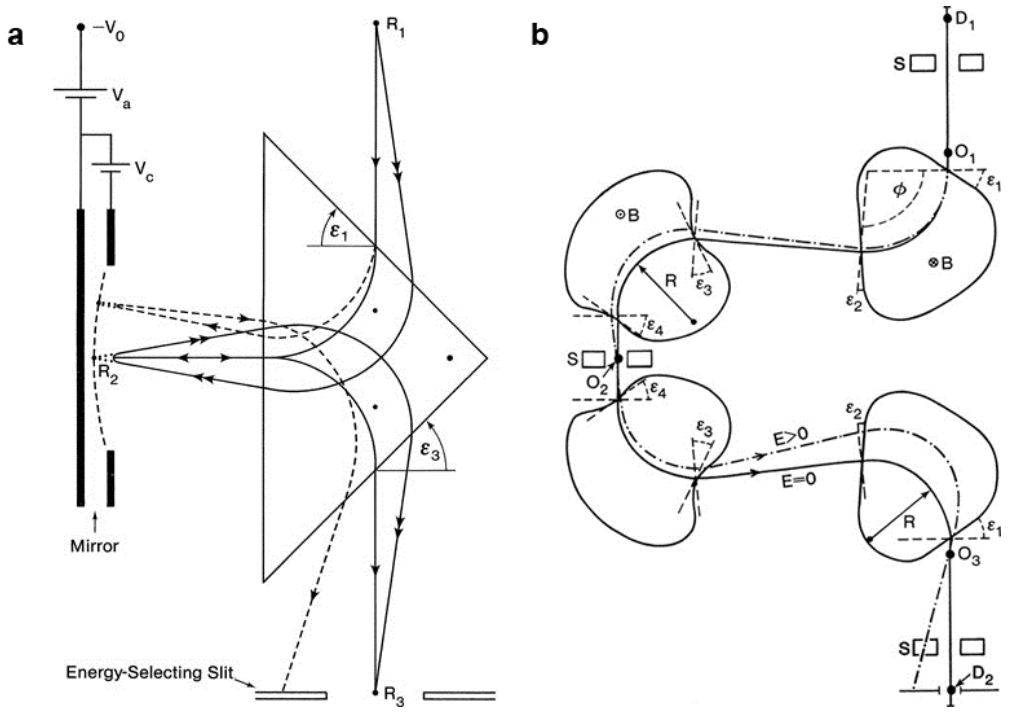

Figure 2.13. (a) Magnetic prism used in combination with mirror to act as energy filter. (b) Omega filter commonly used as energy filter.[95]

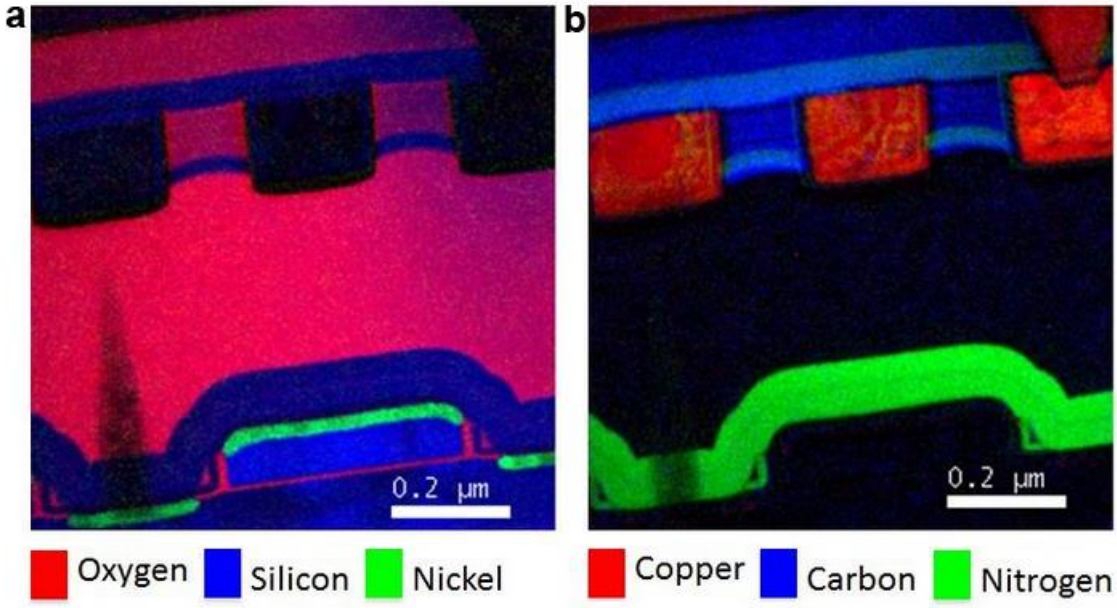

Figure 2.14. Elemental maps obtained from energy-filtered TEM images for device stacks.[97]

(poly-Si and bulk Si<100>), SiO_2 gate oxide, Si_3N_4, Cu contacts, and the formations of silicide (SiNi) can be determined. This can help locate possible failures, contaminations, and intermixing between layers. However, in my dissertation, EFTEM is used for understanding the diffraction from plasmon loss region (see Chapter 4) and not for imaging purposes.

2.4. Aberration Corrected TEM

The challenge to generate spherical aberration free TEM dates back to 1947 when Otto Scherzer first postulated possible schemes to circumvent the aberrations.[98] One of the proposed solutions was to use multipole correctors to produce a negative spherical aberration before the beam passes through objective lens with positive spherical aberration, and hence canceling the aberration. However, the multipole corrector systems are likely to consist of a series of lenses and hence manual alignment procedure might not be feasible. It was not until 1990's that aberration corrector was successfully integrated and commercialized.[99] The reasons for the half of century lagging time are the invention and improvement of fast computing algorithms (and computers) used to correct the lenses and birth of CCD cameras.

There are two types of aberration correcting systems that have been developed almost simultaneously since 1947: quadrupole-octuple (QO) and hexapole correctors, which differ in principles. The QO system is more complicated in nature as it requires more lenses but can correct both spherical and chromatic aberration. On the other hand, the hexapole correctors are much simpler in the ray diagrams with fewer lenses but can only correct the spherical aberration. We will pay attention only for STEM corrector system. The background on CTEM corrector systems can be found on the suitable literature.[99]

The QO corrector systems are integrated in Nion-aberration correction STEM, which was used to perform experiments on detecting dopant atoms in Chapter 5. The ray diagrams on such correctors are shown in Figure 2.15a.[100] The corrector is placed after the condenser lens and before the scan coils consisting of six identical sets of quadrupole-octupole lenses. By appropriately exciting the correct lenses, the corrector produces negative spherical aberration wavefront to compensate for the positive spherical aberration in the objective lens. Hence, the residual aberrations are higher than third order and act as the limiting resolutions.

The hexapole corrector system consists only of two hexapole lenses and two sets of transfer round-lenses as shown in Figure 2.15b.[101] The first hexapole is located at the front focal plane of the first round lens and the other is at the back focal plane of the second round lens. The sets of round lenses and the locations of the hexapoles result in the imaging of the first hexapole with -1 magnification on the second one. Consequently, second-order aberrations are eliminated leaving only third order spherical-like aberration with opposite sign to that of the round objective lens, which cancels the spherical aberration once the probe is incident on the samples.

The new FEI Titan at the University of Minnesota is shown in Figure 2.16a. It is equipped with the hexapole probe corrector systems and hence only corrects the spherical aberrations. For most purposes, this is already sufficient. It is also capable of acquiring EELS spectra with high energy resolution in the order of than 0.1 eV because of the presence of monochromator. HAADF-STEM images obtained from this system at 300 kV for Si <110> is shown in Figure 2.16b. A spatial resolution of about 0.65 Å is readily achievable as evidenced by the ability to resolve the dumbbell spacings of Si <110>.

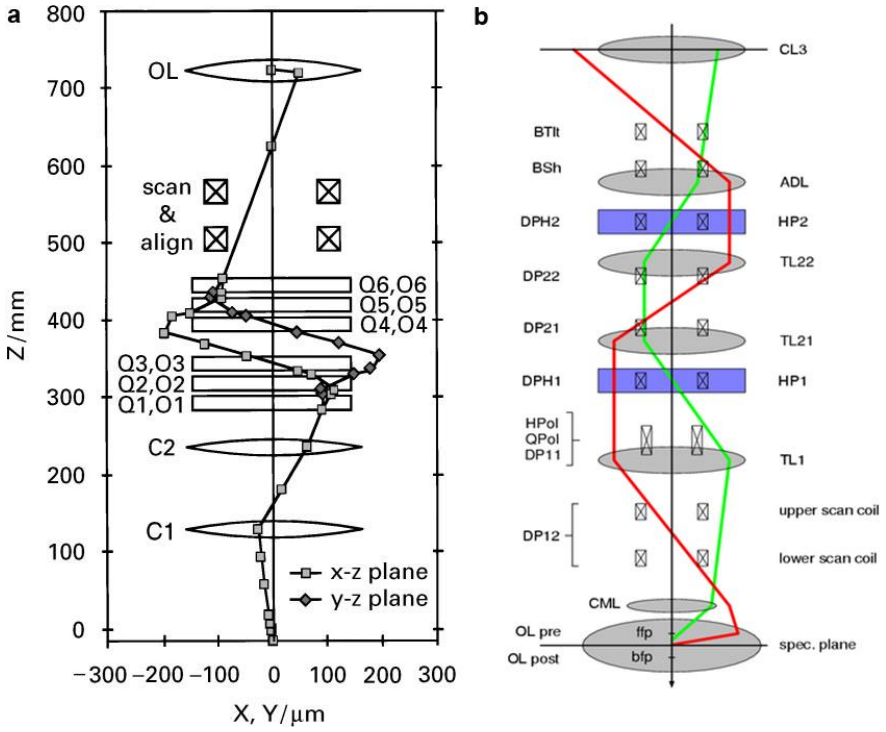

Figure 2.15. Ray trajectories of aberration corrected TEM in (a) quadrupole-octupole[100] and (b) hexapole system.[101]

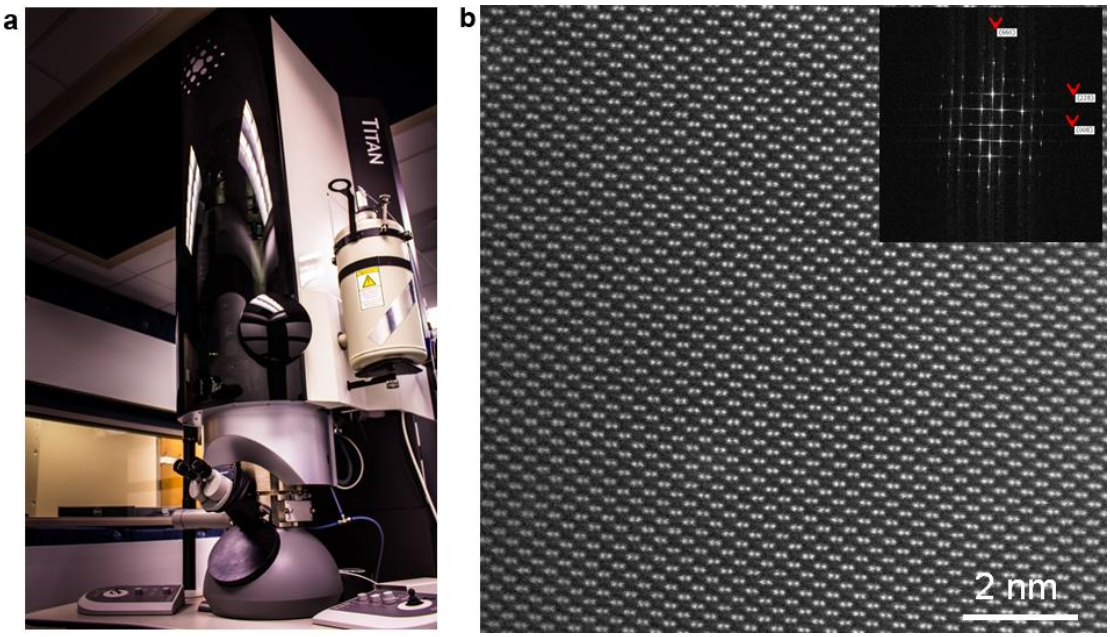

Figure 2.16. (a) The aberration corrector equipped FEI Titan at the University of Minnesota.[102] (b) HAADF-STEM of Si<110> acquired using Titan showing point resolution of about 0.6 Å.[103]

3

Inelastic Scatterings in Nanoscale Semiconductors

This chapter is intended to review and present some results on inelastic scattering events that occur when electron beams pass through materials. It is an important chapter as inelastic scattering is the central theme of my discussions in Chapter 4-6. Materials typically undergo various inelastic scatterings under electron beams such as X-ray emissions, Auger and secondary electron excitations, plasmons, phonons, cathodoluminescene, beam damage, and sputterings. However, we will focus on three types of inelastic scatterings namely bulk plasmons, surface plasmons, and inner-shell (core-loss) excitations.

3.1 Bulk Plasmons

3.1.1 Drude Formulation

Bulk plasmons, or sometimes referred as volume plasmons, are collective oscillations of electrons around the atomic nuclei under excitation of electromagnetic fields (electron beams). In metals, conduction electrons are mostly responsible for such plasmon excitations. In the case of semiconductors or insulators, the oscillations arise predominantly from the valence band electrons. Under the assumptions that the electron oscillation with density n is a minor perturbation, the oscillating electrons with frequency ω can be thought to have a "quasi-mass" m, which is different from the rest mass m_o, and undergo time-dependent displacements $\mathbf{x}$ under the influence of external field $\mathbf{E} = \mathbf{E}\exp(-i\omega t)$ related through[95]

$$m\ddot{\mathbf{x}} + m\Gamma\dot{\mathbf{x}} = -e\mathbf{E}, \tag{3.1}$$

where e is the magnitude of electronic charge and Γ is the damping constant of the plasmon oscillations that will be discussed in Section 3.3. Relation (3.1) is sometimes referred as the Drude formulation. Solving (3.1) for the displacement **x** and calculating the susceptibility $\chi = -enx/(\varepsilon_o m)$, where $\varepsilon_o$is the vacuum permittivity, the complex dielectric function ε(ω) can be expressed as[95]

$$\varepsilon(\omega) = 1 + \chi = 1 - \frac{\omega_p^2}{\omega^2 + \Gamma^2} + \frac{\mathrm{i}\Gamma\omega_p^2}{\omega(\omega^2 + \Gamma^2)}\,, \tag{3.2}$$

where $\omega_p = [ne^2/(\varepsilon_o m)]^{1/2}$ is the plasmon resonant frequency.

3.1.2 Plasmon Cross Section

We have thus far looked at the bulk plasmon response of the electrons that are part of the materials under electron beam excitation. In order to complete the understanding of the plasmonic interaction, it is customary to also examine how the propagating electrons are scattered and modified. Treating the collective valence electron as dielectric medium, the transmitted electrons at position **r** and velocity **v** in the z-direction (column axis) generate a spatially dependent and time-dependent electrostatic potential $\phi(\mathbf{r}, t)$ described by Poisson's equation[95]

$$\varepsilon_0 \varepsilon(\mathbf{q}, \omega)\nabla^2\phi(\mathbf{r}, t) = e\delta(\mathbf{r}, t), \tag{3.3}$$

where the right hand side of (3.3) arises from assuming the propagating electrons can be represented as a point charge $-e\delta(\mathbf{r}\text{-}\mathbf{v}t)$.

During their motions, the electrons can be thought as experiencing stopping powers or losing energies by exciting bulk plasmons (amongst various inelastic events). The stopping power (dE/dz) can be described as

$$\frac{dE}{dz} = \iint n_a E \frac{d^2\sigma}{d\Omega dE} d\Omega dE, \tag{3.4}$$

where E is the energy of the propagating electron and $d^2\sigma/d\Omega dE$ is the double-differential cross section per atom for inelastic scattering. Solving (3.3) for dE/dz is non-trivial but using Fourier transforms, Ritchie has shown that[104]

$$\frac{dE}{dz} = \frac{2\hbar^2}{\pi a_o m_o v^2} \iint \frac{q_y \omega \mathrm{Im}[-1/\varepsilon(q,\omega)]}{q_y^2 + (\omega/v)^2} dq_y d\omega, \tag{3.5}$$

Where a_o is the Bohr radius, m_o is the electron rest-mass, ω is the angular frequency $(E/\hbar)$, q_y is the y-component of the scattering vector perpendicular to **v**. $\mathrm{Im}[-1/\varepsilon(q,\omega)]$ is the term containing the response of the materials responsible for "stopping" the propagating electrons also known as the *energy loss function*. By equating (3.4) and (3.5), an expression for the double-differential cross section can be calculated as[95]

$$\frac{d^2\sigma}{d\Omega dE} \approx \frac{\mathrm{Im}\left[-\frac{1}{\varepsilon(q,\omega)}\right]}{\pi^2 a_o m_o v^2 n_a} \left(\frac{1}{\theta^2 + \theta_E^2}\right),$$

where $\theta_E = E/(\gamma m_o v^2)$ is the characteristic angle of the inelastic scattering where most of the scattered electrons are contained.

The energy loss function $\mathrm{Im}\left[-\frac{1}{\varepsilon(q,\omega)}\right]$ in the numerator can be found from (3.2) to be

$$\mathrm{Im}\left[-\frac{1}{\varepsilon(q,\omega)}\right] = \frac{\varepsilon_2}{\varepsilon_1^2 + \varepsilon_2^2} = \frac{\omega\Gamma\omega_p^2}{\left(\omega^2 - \omega_p^2\right)^2 + (\omega\Gamma)^2}$$

$$= \frac{E\left(\Delta E_p\right)E_p^2}{\left(E^2 - E_p^2\right)^2 + \left(E\Delta E_p\right)^2}, \tag{3.6}$$

where we have used $E = \hbar\omega$ and $\Delta E_p = \hbar\Gamma = \hbar/\tau$ to obtain (3.6). Substituting the energy loss function from (3.6), the double differential cross section for bulk plasmon scattering can be written as[95]

$$\frac{d^2\sigma}{d\Omega dE} \approx \frac{1}{\pi^2 a_o m_o v^2 n_a} \frac{E(\Delta E_p)E_p^2}{\left(E^2 - E_p^2\right)^2 + \left(E\Delta E_p\right)^2}\left(\frac{1}{\theta^2 + \theta_E^2}\right). \qquad (3.7)$$

This cross section expression is a complete description of how the interactions between propagating electron and the valence bands electrons through excitation of bulk plasmon results in the reduction of energy and re-orientation of the propagation vector of the transmitted electrons.

3.1.3 Plasmon Dispersion

The cross section (3.7) has not told the whole stories yet as it only applies to small momentum transfer although it is valid for all energy range. Various efforts have been done to obtain plasmon dispersion relation. One simplest method is the Lindhard model, which uses the Drude formulation in Section 3.1 to calculate E_P for higher q. The model uses random phase approximations[105] and neglects any spin interactions and Coulomb correlation and hence is most accurate for metals. The relation is given by

$$E_P(q) = E_P + \gamma(\hbar^2/m_0)q^2,$$

where E_P is the plasmon energy at $q = 0$ discussed in previous sections, and γ is the dispersion coefficient equal to $\frac{3}{5}\frac{E_F}{E_P}$.

Incorporating $E_P(q)$ modifies the cross section expression (3.7) to become[95]

$$\frac{d^2\sigma}{d\theta dE} = \frac{\sin\theta}{\pi n_a a_0}\frac{1}{E_0}\left(\frac{1}{\theta^2 + \theta_E^2}\right)\left[\frac{E(\Delta E_P)E_P^2}{\left(E^2 - E_P^2 - \gamma 4E_P E_0(\theta^2 + \theta_E^2)\right)^2 + (E\Delta E_P)^2}\right].$$

It is an important relation as it will be used a central theme for examining the role of plasmon scattering in HAADF-STEM imaging discussed in Chapter 6.

Figure 3.1 shows the plot of $\frac{d^2\sigma}{d\theta dE}$. The cross section falls off considerably after about 8 mrad but the gist of the signal is contained within less than 0.1 mrad scattering angle. This indicates that the plasmon scattering is largely forward direction. It peaks at 16.6 eV in the energy scale, which corresponds to the value of the plasmon energy in the limit of low scattering angle E_P.

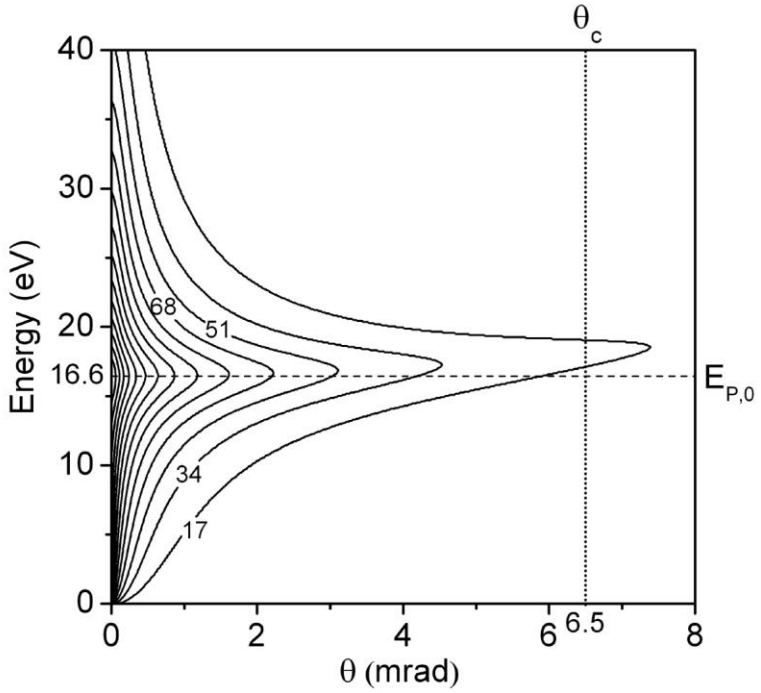

Figure 3.1. Differential cross section of bulk plasmon for Si under 100 keV accelerating voltage electron beam. The cross section has a maximum at $\boldsymbol{E_P}$ = 16.6 eV at the limit of low scattering angle. The critical angle signifies the angle at which the intensity of the cross section has dipped significantly.[106]

3.1.4 Bulk Plasmons in Semiconductors

The dielectric response models in (3.1) and (3.2) are derived for free electrons; a valid assumption for metals but not necessarily true for semiconductors. The motions of valence band electrons in semiconductors are constrained by the lattice and hence not completely free. It is assumed that these electrons bound to the lattice have their own oscillation frequency ω_b. In order

to take this into consideration additional term containing the oscillations of the bound electrons is added to (3.1)

$$m\ddot{\mathbf{x}} + m\Gamma\dot{\mathbf{x}} + m\omega_b^2\mathbf{x} = -e\mathbf{E}, \tag{3.8}$$

modifying the complex dielectric function in (3.2) to become

$$\varepsilon(\omega) = 1 + \chi_b = 1 + \frac{\omega_p^2}{\omega_b^2 - \omega^2 - \mathrm{i}\omega\Gamma}, \tag{3.9}$$

where ω_p is the plasmon frequency if the electrons are free. This modification can be interpreted as shifting the plasmon resonant frequency to $\left(\omega_p^2 + \omega_b^2\right)^{1/2}$ in the case of semiconductors. The magnitude of the electron binding energy $E_b = \hbar\omega_b$ is similar to the energy gap E_g. For most semiconductors $E_p^2 \gg E_g^2$ and hence $E_p^2 \approx E_{p,free}^2$ (e.g. for Si $E_p^2 = 275\ eV^2 \gg\ E_g^2 = 1.2\ eV^2$). Consequently, the Drude formulation derived in Section 3.1.1 is considered valid, at least for semiconductors studied in my thesis.

3.1.5 Plural Scattering

The probability of bulk plasmon scattering is dependent on the thickness of the samples. A parameter called plasmon mean free path λ ($\lambda_{Si,plasmon}$ = 121 nm) describes the average distance traveled by electron beams before undergoing a single bulk plasmon scattering event. But single, double, and multiple scatterings occur at finite probability at typical thickness ranges used in TEM (20-50 nm). The distribution of single and multiple plasmon scatterings after passing through samples obeys Poisson's statistics if the plasmon scatterings are assumed to be independent events:[95]

$$P_n = \frac{I_n}{I_t} = \left(\frac{1}{n!}\right)\left(\frac{t}{\lambda}\right)^n \exp\left(-\frac{t}{\lambda}\right), \tag{3.10}$$

where P_n is the intensity ratio of the n-th scattering to the total intensity and t is the sample thickness. From (3.10), one can see that the ratio for the single scattering is

$$P_1 = \frac{I_1}{I_t} = \frac{t}{\lambda}\exp\left(-\frac{t}{\lambda}\right). \tag{3.11}$$

Figure 3.2 shows experimental bulk plasmon from Si(100) with six varying thicknesses of 32, 42, 73.5, 82.5, 127, and 135 nm under excitation of 100 kV electron probe, 1.3 mm C_s, and 21.5 mrad EELS collection angles.[106] The spectra are all normalized with respect to the intensity of the zero-loss peaks. The evolution of the 1st plasmon peak at about 17 eV energy loss can clearly be observed as the thickness increases. The 2nd plasmon peak starts to become significant once the thickness reaches half of the plasmon mean free path (120 nm) and can be seen clearly starting with the 73.5 nm thick sample. The 3rd plasmon peak starts to appear when the thickness is in the vicinity of the mean free path for the 127 nm sample.

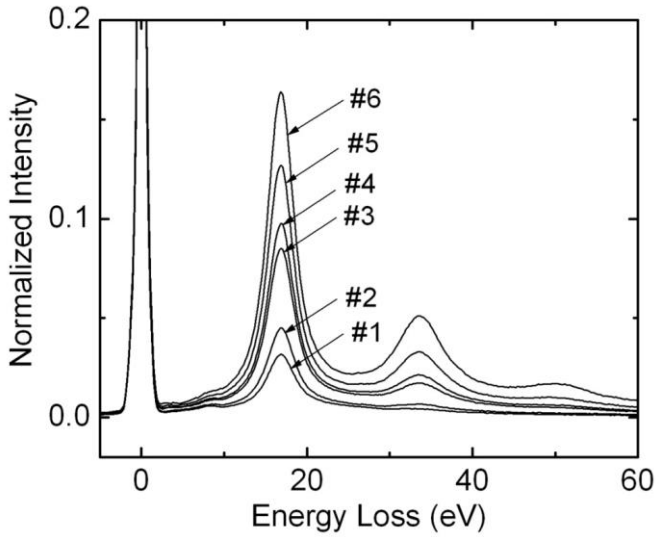

Figure 3.2. EELS spectra from Si<100> having thicknesses of 32, 42, 73.5, 82.5, 127, and 135 nm. The accelerating voltage was 100 keV and the collection angle was 21.5 mrad. The 2nd plasmon peaks start to appear when the sample thicknesses are at least half of the plasmon mean free path of 120 nm. The 3rd plasmon peaks arise when the thicknesses are roughly equal to the mean free path.[106]

3.2. Surface Plasmons

The term surface plasmon is more loosely defined than the bulk plasmon counterpart. There are two main types of surface plasmon excitations; the first one is *propagating* electromagnetic fields confined on metal/dielectric interfaces more appropriately referred as surface plasmon polaritons (SPP) and the other one is *standing waves* arising from oscillations of conduction band electrons on the surface of nanostructured materials such as nanocrystals and nanoprisms known as localized surface plasmon resonance (LSPR). Sometimes both are (correctly) referred as surface plasmons. In SPP, the excitation fields (electron beam) are the "plasmon" while the electrons from materials act as the main "plasmon" in for LSPR. In my research, we will focus on LSPR excitation in semiconductor nanocrystals.

Origin of LSPR

The scattering and absorption of electromagnetic field by small particles were actually known as early as in 1908 when Mie developed a theory to understand the colors of colloidal gold particles in solution, which vary depending on the size and the choice of solution.[107] However, the term LSPR was not coined until 1950's after the discovery bulk plasmon using electron energy loss experiments.[108] The complete understanding of how excitation field is absorbed and scattered as well as the response of the electrons in the materials in the form of LSPR has led to the numerous technological applications. Enhanced solar cells efficiency,[109, 110] biosensors,[111, 112] and stained glass windows on medieval churches are among the ubiquitous utilizations of LSPR in nanostructured materials.

A sphere with radius a at the origin is exposed to a uniform and static electric field $\mathbf{E} = E_0\hat{\mathbf{z}}$ such as shown in Figure 3.3. The complex dielectric function of the sphere is $\varepsilon(\omega)$ and the surrounding medium is assumed to have a

dielectric constant ε_m. In the electrostatic limit, we can consider the situation in Figure 3.3 as solving the Laplace equation[113]

$$\nabla^2\Phi = 0, \tag{3.12}$$

where Φ is the potential of the sphere and the electric field $\mathbf{E} = -\nabla\Phi$. The solutions in spherical geomtery to (3.12) after applying the appropriate boundary conditions are[113]

$$\Phi_{in} = -\frac{3\varepsilon_m}{\varepsilon(\omega) + 2\varepsilon_m} E_0 r\cos\theta \tag{3.13}$$

$$\Phi_{out} = -E_0 r\cos\theta + \frac{\varepsilon(\omega) - \varepsilon_m}{\varepsilon(\omega) + 2\varepsilon_m} E_0 a^3 \frac{\cos\theta}{r^2}, \tag{3.14}$$

where the subscripts on the left-hand-side denote whether the potentials are inside or outside the sphere. Physically, (3.14) means that the potential outside the sphere is the superposition of the applied electric field and a dipole at the center of the sphere.

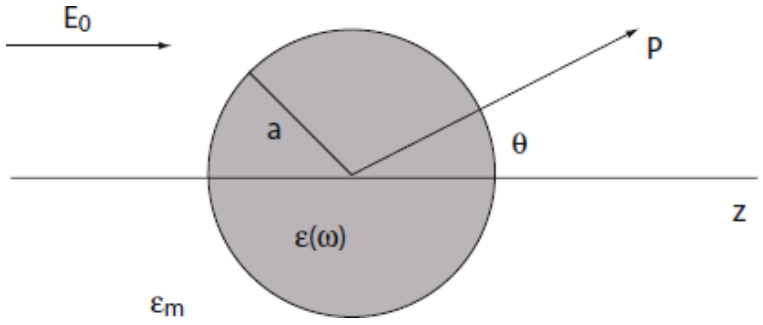

Figure 3.3. Schematic illustration of a plasmonic sphere with dielectric function $\boldsymbol{\varepsilon(\omega)}$ under the excitation of eternal field $\boldsymbol{E_0}$ under medium with dielectric constant $\boldsymbol{\varepsilon_m}$.[113]

Introducing dipole moment **p** into (3.14)

$$\Phi_{out} = -E_0 r\cos\theta + \frac{\mathbf{p}\cdot\mathbf{r}}{4\pi\varepsilon_0\varepsilon_m r^3} \tag{3.15}$$

$$\mathbf{p} = 4\pi\varepsilon_0\varepsilon_m a^3 \frac{\varepsilon(\omega)-\varepsilon_m}{\varepsilon(\omega)+2\varepsilon_m}\mathbf{E_0}. \tag{3.16}$$

The polarizability α can be found using the relation $\mathbf{p} = \varepsilon_0\varepsilon_m\alpha\mathbf{E_0}$ giving

$$\alpha = 4\pi a^3 \frac{\varepsilon(\omega)-\varepsilon_m}{\varepsilon(\omega)+2\varepsilon_m}. \tag{3.17}$$

The polarizability (3.17) reaches the resonant maximum when the term in the denominator is a minimum, which is satisfied when

$$Re[\varepsilon(\omega)] = -2\varepsilon_m. \tag{3.18}$$

This condition is sometimes called the Fröhlich criterion characterizing the resonant oscillation of the conduction band electrons under applied oscillating field.[113] It is important to note that the derivation (3.12)-(3.18) is done under quasi-static approximation, which means that the phase of the oscillating applied electromagnetic field is constant over the sphere size; in other words the particle diameter d is much smaller than the wavelength of the applied field λ. This assumption is valid for typical optical experiments where the wavelength is in the order of hundreds of nanometers and the particle size is tens of nanometer or smaller. Condition (3.18) can then be thought of *dipole* generation inside the sphere by the slight displacements (oscillations) or the electrons in the conduction band. However, this condition might not be valid for excitation using fast electron in which the wavelength is sub-nm. Garcia de Abajo has shown that in the case of excitation using relativistic electron beam the resonant oscillations of the electrons are not limited to the generation of dipole LSPR, but also quadrupole, hexapole and other multipole LSPR.[114] The main contribution to the observed intensity is still from the dipole LSPR particularly for nanometer size particles and hence we only pay attention to the dipole modes in (3.18).

3.3. Damping of Plasmons

Bulk and surface plasmons typically have small finite lifetime in the order of tens of femtoseconds. Although they arise from different mechanisms, the sources of damping are similar for both bulk and surface plasmons. Hence, the discussions of the origins of the plasmon damping are intended for both bulk and surface plasmons unless otherwise noted. There are various ways that plasmon can decay such as through the creations of electron-hole pairs, surface scattering, and interface decay channels. The shapes, sizes, types of chemicals attached on the surfaces, and grain sizes are among the critical factors determining which mechanisms are most prevalent in governing the decay processes.

3.3.1 Creations of Electron-Hole Pairs

One of the main damping sources of plasmon excitation is the creation of electron-hole pairs. The first condition to allow such creations is that the bulk plasmon energy E_P is larger than the energy gap E_G, which is readily satisfied for most semiconductor materials. The second condition is for the process to have a favorable momentum transfer. From energy and momentum conservation of the plasmon scattering processes one can write[95]

$$E = \frac{\hbar^2}{2m_0}(\mathbf{q} + \mathbf{q_i})^2 - \frac{\hbar^2}{2m_0}\mathbf{q_i}^2 = \frac{\hbar^2}{2m_0}(q^2 + \mathbf{2q} \cdot \mathbf{q_i}) \tag{3.19}$$

where the lattice electron initially has a momentum $\hbar\mathbf{q_i}$and acquire $\hbar\mathbf{q}$ after the plasmon scattering processes. The highest energy transfer occurs when $\mathbf{q_i}$ is parallel to $\mathbf{q}$ and the largest, which is equal to q_F giving

$$E_{max} = \hbar^2/2m_0\,(q^2 + \mathbf{2}qq_F), \tag{3.20a}$$

while the smallest energy transfer is satisfied when $\mathbf{q_i}$ is antiparallel to $\mathbf{q}$ and equal to q_F

$$E_{min} = \hbar^2/2m_0\,(q^2 - \mathbf{2}qq_F). \qquad (3.20b)$$

Within this range $E_{min} < E < E_{max}$, the plasmon oscillations can decay into single electron excitation (electron-hole pair). Figure 3.4 shows the range of possible single electron excitations (hatched area). If the plasmon energy falls inside this single electron regime, it will have a smaller lifetime than if it is located outside the hatched area. However, even if the plasmon energy is outside the single electron regime, it can still decay into single electron excitation by the help of lattice momentum (shown as a straight arrow in Figure 3.4).[95]

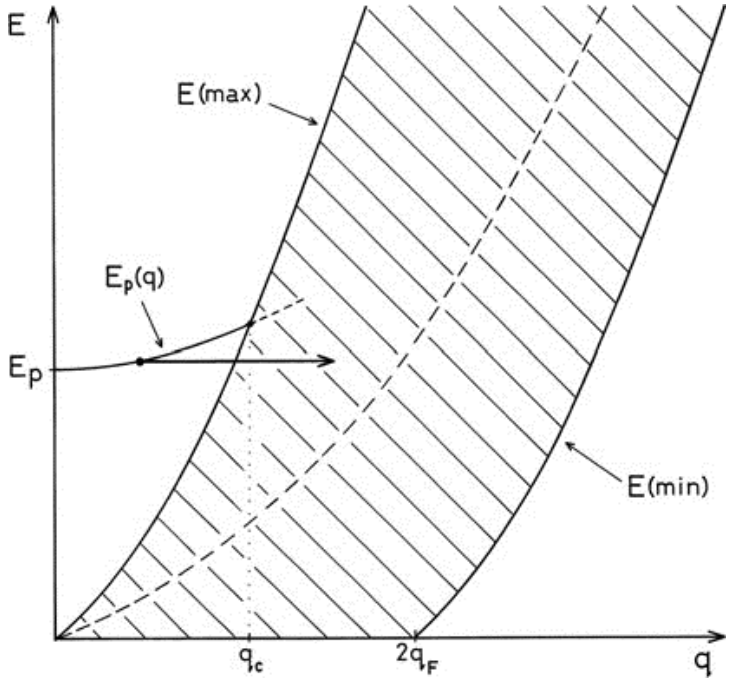

Figure 3.4. The q-dependent energy loss showing the region for which single electron excitations are possible (hatched area). When the plasmon scattering falls in this region, as depicted by the plasmon dispersion (dashed line), the plasmon experiences additional decay mechanism through single electron excitations.[95]

3.3.2 Defects

Various types of defects such as steps and grain boundaries can act as sources of decay. In grained gold nanoarrays, the surface plasmon lifetime increases as the grain sizes increase by annealing.[115] Figures 3.5a and b show the AFM images of the gold array before and after annealing. The grain sizes can be seen to increase in Figure 3.5b. The measured FWHM of transmittance spectra as a function of grain size is shown in Figure 3.5c. The smaller FWHM as higher annealing temperatures were reached indicate longer plasmon lifetimes.

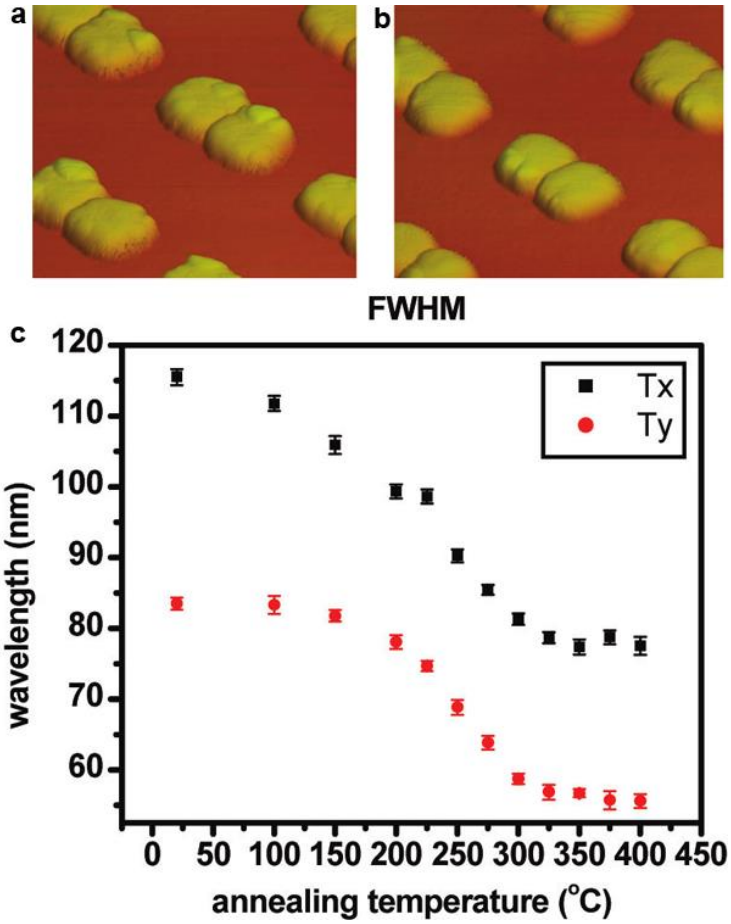

Figure 3.5 Atomic force microscopy (AFM) images of grained Au crystals (a) before and (b) after annealing. The disappearance of the grain boundaries is observed after annealing. The larger grains exhibit higher lifetime or smaller FWHM as shown in (c) for the FWHM of transmittance spectra as a function of annealing time.[115]

A similar phenomenon to the effects of grain sizes is the size of nanocrystals. Although surface is not necessarily a defect, the dangling bonds present could become the source of plasmon decay. Figure 3.6 shows the EELS signals from differing sizes of Si nanocrystals.[116] As the size increases, the FWHM of bulk plasmon signals at 16-17 eV energy loss decreases approaching the FWHM of the Si thin film. The observed energy shift is due to quantum effects of the Si nanocrystals.

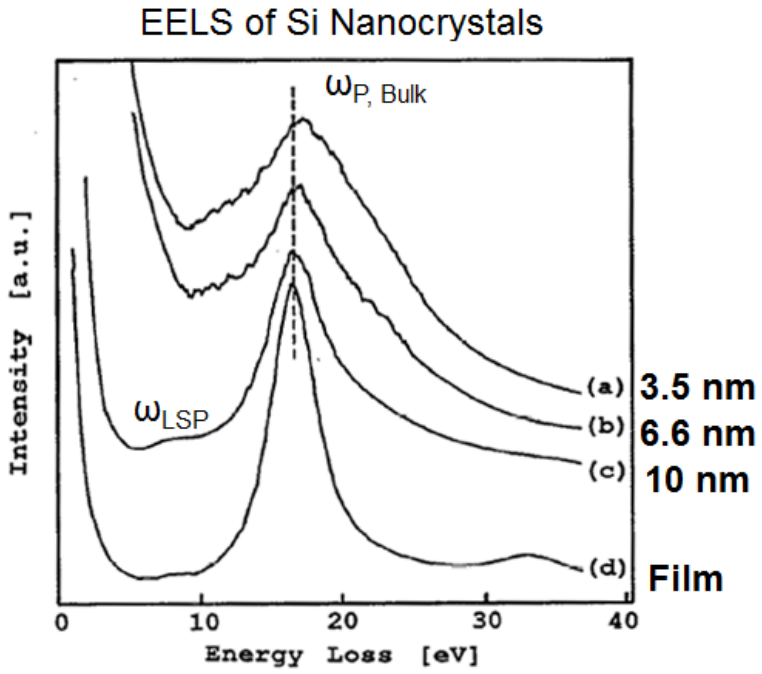

Figure 3.6. Low-loss EELS spectra of Si nanocrystals as a function of sizes. The bulk plasmon signal exhibits a shrinking FWHM as the size increases indicative of a higher plasmon lifetime.[116]

3.3.3 Chemical Interface Damping

This type of plasmon decay is prevalent in colloidally synthesized nanocrystals whereby organic molecules (or adsorbates) are attached on the surface of the nanocrystals as size stabilizers. Post-synthesis molecular attachment on the surfaces of nanocrystals could also induce this type of decay.

The main sources of plasmon damping are the unoccupied density of states in the adsorbates. More clearly, Figure 3.7 depicts the energy band alignment of adsorbates on the surface of metal nanoparticles.[117] When the adsorbates are still free molecules, they act largely as atoms and absent of any bands (right hand side of Figure 3.7). Once attached, the collection of adsorbates has finite bandwidth near the metal interfaces. The empty density of states in the adsorbed molecules attracts the oscillating electrons from the metals and induces plasmon dephasing before returning back to the metals.[117]

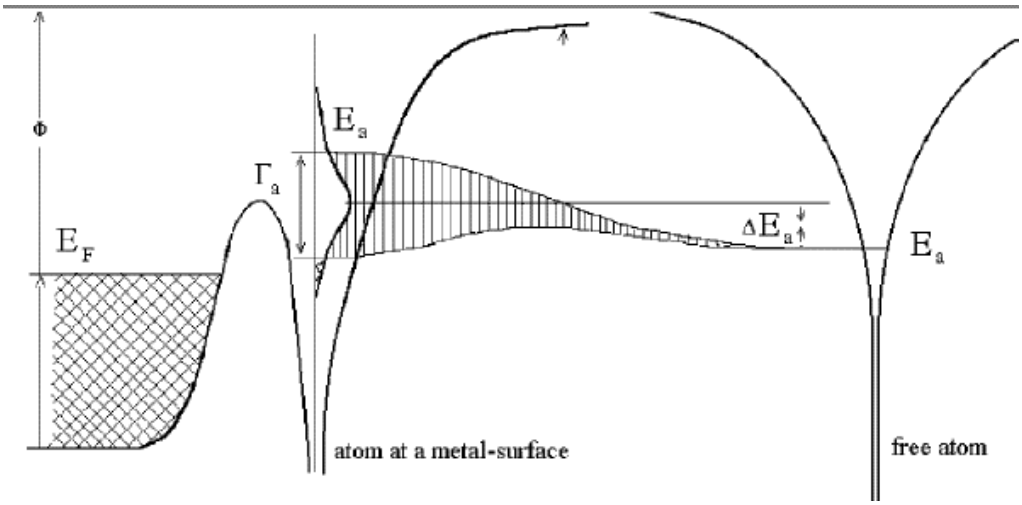

Figure 3.7. Energy band diagram at the nanocrystal surface before and after the attachment of chemical adsorbates. Before attachment, the adsorbates do not exhibit bands as they act as free molecules. After attachment, bands exist in the adsorbed molecules.[117]

The strength of the chemical interface damping depends on various factors such as the chain length of the adsorbates, the energy alignment between the metal and the adosrbates, and the bandwidth of the adsorbed molecules. In the extreme case where the affinity energy of the adsorbed molecules is far from the Fermi level of the metals, plasmon damping occurs to a lesser extent. Capped Au nanocrystals are among the most studied metals particularly for LSPR

purposes. Figure 3.8 shows measured absorbance spectra of Au nanoparticles capped with different adsorbates showing varying FWHM.[118]

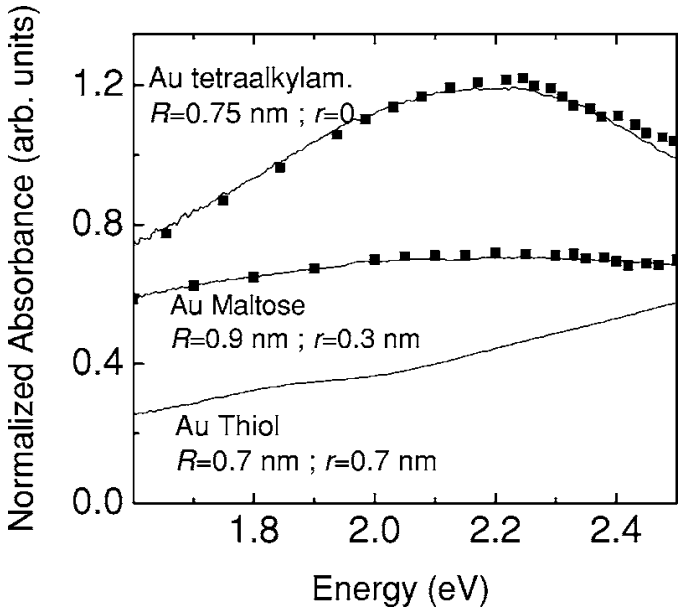

Figure 3.8. Absorbance spectra for Au nanoparticles coated with different adsorbates.[118]

3.3.4 Quantification of Dephasing Time Using STEM-EELS

The determination of plasmon damping time is usually done using optical experiments. Nanoparticles are illuminated with narrow band lasers and the dephasing time is calculated from the FWHM of the corresponding optical spectra. Since ensembles of nanoparticles are needed to obtain good signal to noise ratio, optical experiments typically lack the knowledge of the exact nanocrystal size and shapes under consideration.

The invention of aberration corrected TEM equipped with monochromated EELS system has recently enabled the measurement of plasmon dephasing time from isolated nanoparticles.[119] The main reason holding STEM-EELS as a tool to quantify plasmon dephasing is the energy resolution, which is generally worse than optical experiments. Without monochromator, the EELS

energy resolution is about 0.5 eV at best much larger than typical plasmon lifetime in the fs or meV range. Monochromated EELS can easily achieve such energy resolution while maintaining the high spatial sub-Å spatial resolution.

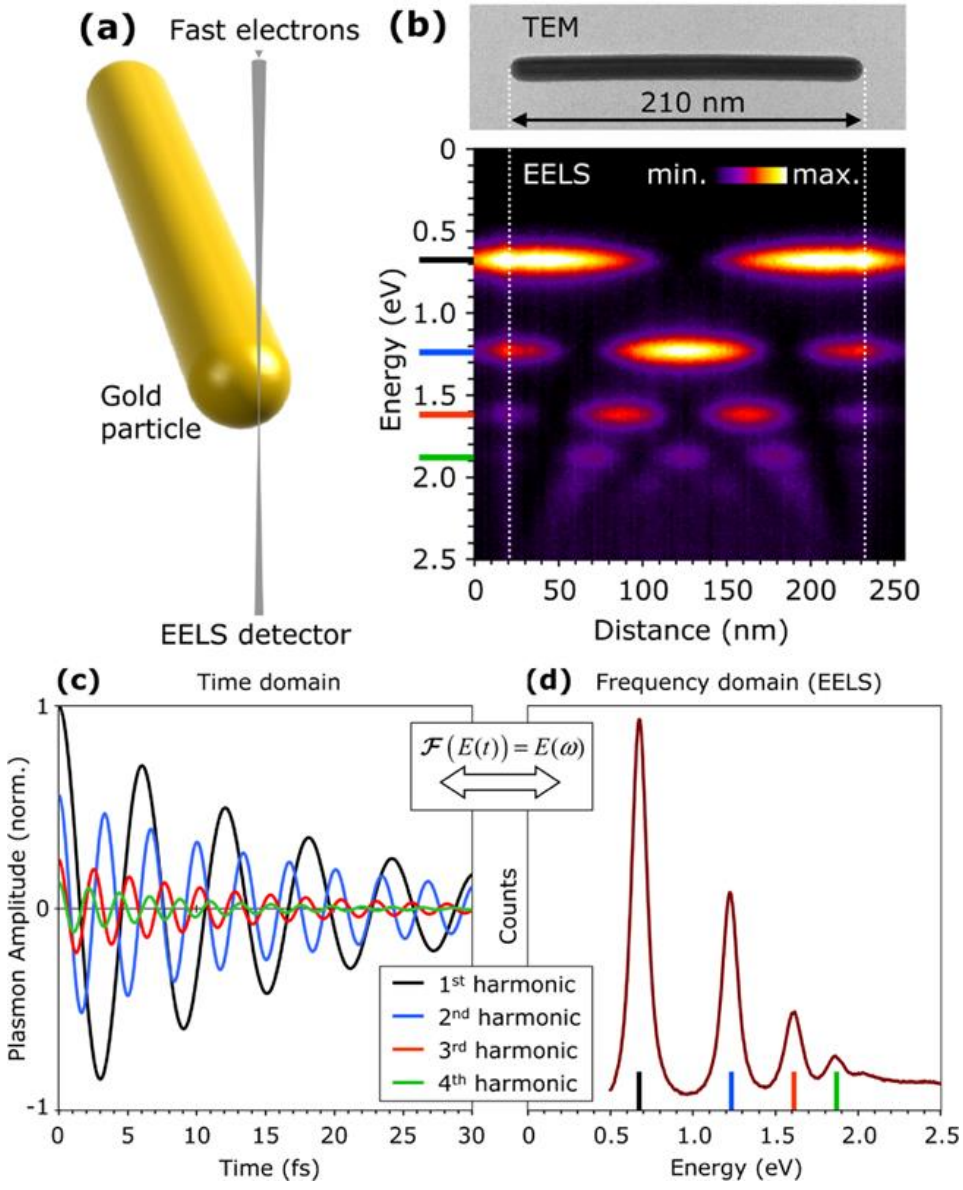

Figure 3.9. (a) Schematic illustrations of aloof excitations of surface plasmon on gold nanoparticle using electron beams. (b) Spatial distributions of various plasmon modes along the nanoparticle. The four major modes are indicated by colors on the energy scale. The EELS spectra in (c) time and (d) frequency domain for the four main modes. The damping is characterized by the decreasing amplitude in time domain and the FWHM in frequency domain.[119]

The key setup in STEM-EELS dephasing time experiment is aloof excitation, in which focused electron probe is passed 1 – 2 nm near the area of interest. In the case of gold nanorods shown in Figure 3.9a, the electron probe is placed near the one of the tips. EELS signals in the time domain obtained from such measurement is shown in Figure 3.9c consisting of multiple damped harmonics of the plasmon resonance. In frequency space, which is a more common representation of EELS spectra, the four main harmonics give rise to the lowest four energy loss peaks each with the corresponding FWHM. The dephasing time (T) of each plasmon modes can be calculated from the FWHM (γ) according to $T = 2\hbar/\gamma$.[119] Figure 3.10 summarizes the dephasing time for various plasmon modes obtained from different morphologies and sizes.

3.4 Interactions of LSPR

The LSPR discussed in Section 3.2 arises from isolated nanocrystals or ensembles of nanocrystals in the absence of interactions amongst them. This section is dedicated to explore possible types of LSPR interactions in collections of nanocrystals and how such interactions affect the observed LSPR signals. There are three main types of plasmonic interactions that exist in the literature: i) dipolar coupling, ii) tunneling regime coupling, and iii) charge transfer plasmon. Although plasmon modes exist in multiple modes, we will mainly consider the dipolar modes, which is a good assumption for small (< 10 nm) nanoparticles.

The most common interaction is dipolar coupling, which is a long-range force and arises due to the dipole approximation of the surface plasmon. There are no specific distances at which the dipolar interactions start to appear, as they are sample and size dependent. However, a general rule of thumb is that such interactions can be observed when the distance between particles is less than one and a half of the radii of the particles for spherical sizes.[120] The effect of dipolar interactions is described in Figure 3.11 by assuming the surface plasmon

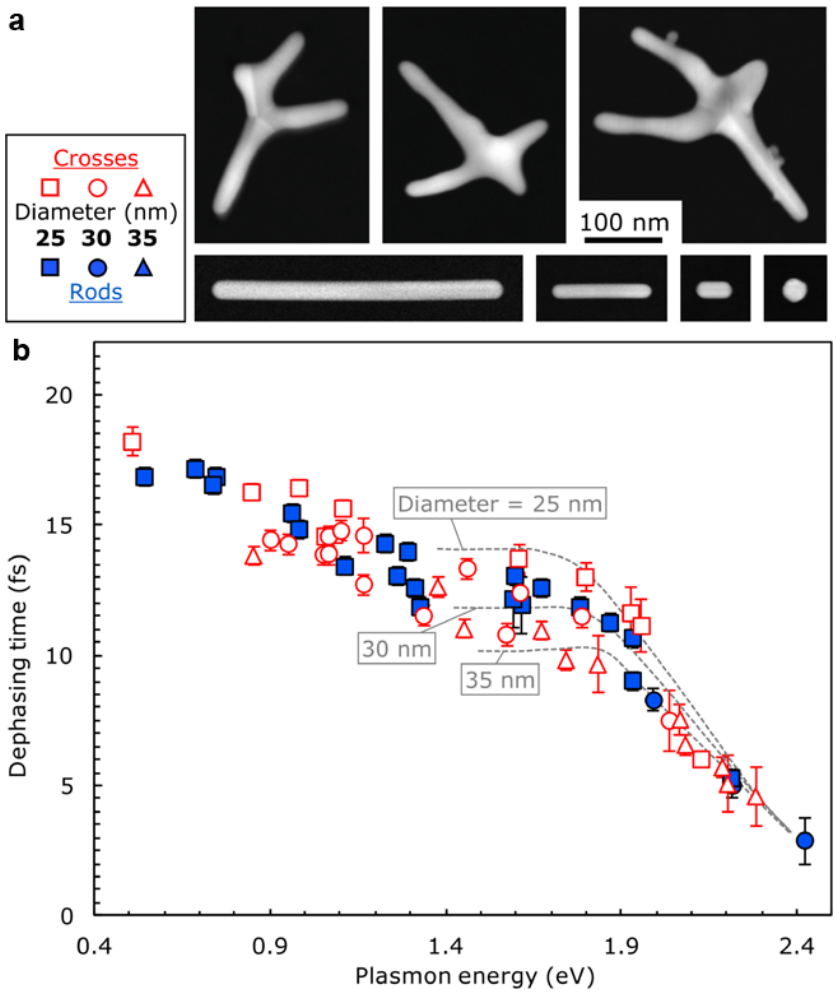

Figure 3.10. (a) HAADF_STEM images of varying sizes of gold nanorods used to measure plasmon dephasing time. (b) Measured plasmon dephasing time as a function of plasmon energy. [119]

acts as a dipole. In the first case (Figure 3.11a), the dipoles are aligned transversely causing repulsion from the equal charges on each side. This results in the blue-shifts of the surface plasmon signal. When aligned longitudinally (Figure 3.11b), the attracting dipoles require less excitation energy to oscillate at the plasmon frequency and hence red-shifts are typically observed.[113] Figures 3.11c and d show the experimental evidence for the transverse and longitudinal interactions of gold particles arrays.

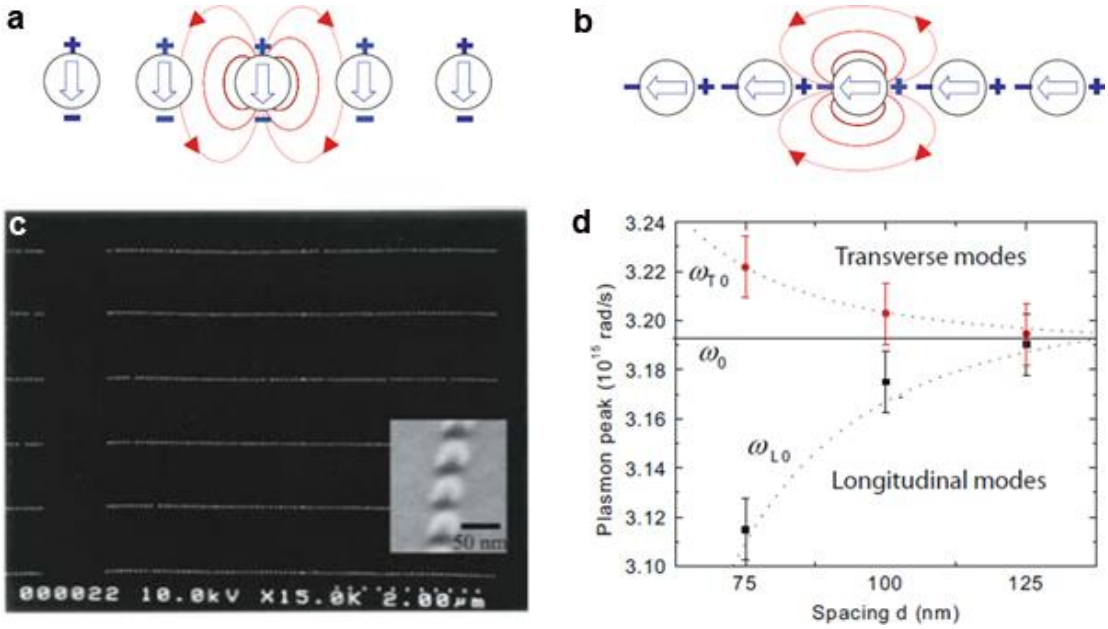

Figure 3.11. (a) Schematic illustration of dipolar coupling in (a) transverse and (b) longitudinal mode. (c) SEM micrographs of gold arrays and the measured plasmon resonance as a function of spacings compared with theoretical prediction.[113]

The red-shifts of longitudinal plasmon interaction increase as the separation distance between particles decreases as shown in the calculated optical absorption spectra in Figure 3.12b.[120] At a particular distance less than half of the particle radius, the tunneling LSPR interaction regime becomes the dominating effect. In this condition, the electrons can tunnel to the neighboring particles causing the surface plasmon to be out of phase when penetrating the insulating barrier. Hence, the spectra become broadened due to lower plasmon lifetime as shown in the red curves in Figure 3.12b.

When conducting channels form once the nanoparticles are in contact, or other means of charge conductions besides tunneling such as inserting molecules capable of conducting charges, the plasmon lifetime is recovered and the spectra exhibit blue-shifts back to the initially non-dipole interaction condition.[120] The calculated optical absorption method excludes the presence of

adsorbates on the surface of the nanoparticles and hence predicts that the plasmon lifetime is smaller (broader peaks) compared to the dipole interaction regime.

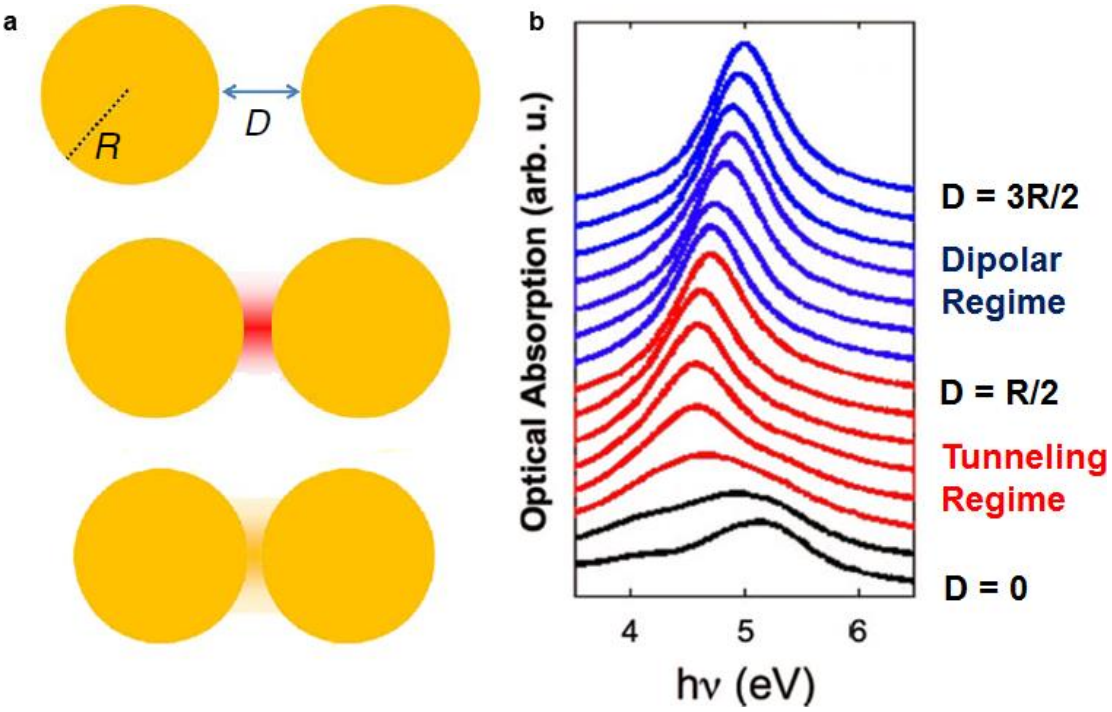

Figure 3.12. (a) Schematic illustration of three different coupling regimes: dipolar, tunneling, and charge transfer plasmon. (b) Calculated optical absorption spectra under decreasing interparticle spacings.[120]

When the nanocrystals are in the touching regime, another interaction called electronic coupling can arise.[121] This coupling is different from the charge transfer plasmon coupling and originates from the interaction between neighboring wavefunctions of conduction and valence bands. The effects on the band structures of the nanocrystals ensembles mimic the atom to solid band formation as shown in Figure 3.13a. The strength of the coupling increases as the dielectric constant (through the size of exciton Bohr radius) of the materials

increases. Hence, PbSe nanocrystals, with a static dielectric constant of 23, can exhibit strong electronic coupling. The coupling effects are induced by exchanging long surface ligands with shorter ones such as hydrazine.[122] The FTIR absorbance spectra as a function of hydrazine reaction time for PbSe nanocrystals are shown on Figure 3.13b. The 1st exciton transition energy exhibits a red-shift as more hydrazine is reacted signifying the lowering of the band gap as shown in Figure 3.13a.

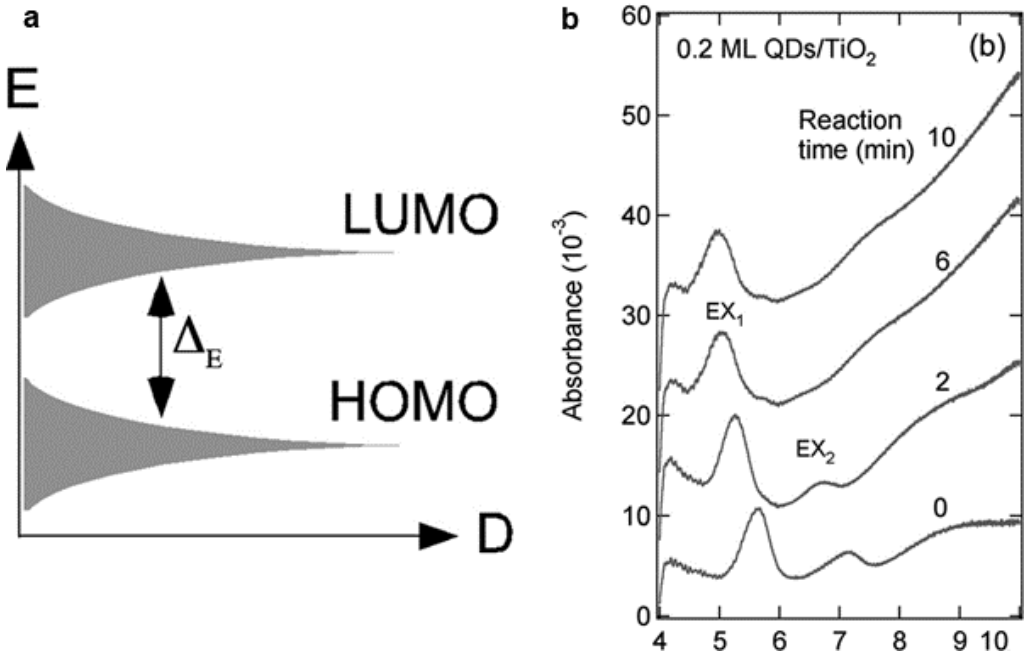

Figure 3.13. (a) Band formation in arrays of nanoparticles under decreasing interparticle spacings. (b) Evolution of the first exciton energy transitions as the interparticle spacing decreases by longer hydrazine reaction time.[122]

3.5.Core-Loss Excitation

We have thus far discussed the plasmon scattering phenomena, which are collective excitations of the electrons in materials and hence can be approximated as delocalized scattering (not confined to an atom). The core-loss or inner-shell excitations, however, are localized to each atom and arise from

electronic transitions from inner-shell orbitals to available states above the Fermi level. The notations and brief explanations for different orbital transitions can be found in Section 2.3.2. In this section, the cross section for core-loss EELS excitations is discussed and compared with experimental spectra.

Inner-shell excitations can be described with time-dependent perturbation theory for transition rate between initial and final states assuming that the excited electrons are interacting. This is sometimes referred as the Fermi's Golden rule. The differential cross sections derived based on this approximation is[123]

$$\frac{d\sigma_{if}}{d\Omega} = \left(\frac{m}{2\pi\hbar^2}\right)^2 \frac{k_f}{k_i} \left| \iint \phi_f^*(r') \exp(\mathrm{i}(\mathbf{k_i} - \mathbf{k_f}) \cdot \mathbf{r}) V_{\mathrm{Coul}}(\mathbf{r}, \mathbf{r}') \phi_i(r') d^3r d^3r' \right|^2 \quad (3.21)$$

where $\mathbf{r}$ is the vector coordinate of the incident electrons having initial plane wave state of $\exp(\mathrm{i}\mathbf{k_i} \cdot \mathbf{r})$ and final state $\exp(\mathrm{i}\mathbf{k_f} \cdot \mathbf{r})$. These traveling electrons interact with the electrons in the atomic orbitals through the repulsive Coulomb potential $V_{\mathrm{Coul}} = e^2/(4\pi\varepsilon_0|\mathbf{r} - \mathbf{r_o}|)$, which causes electronic transition from the initial state ϕ_i to the final state ϕ_f. By introducing the scattering vector $\mathbf{q} = \mathbf{k_i} - \mathbf{k_f}$, (3.21) can be written as

$$\frac{d\sigma_{if}}{dEd\Omega} = 4\left(\frac{e^2 m}{4\pi\varepsilon_0\hbar^2}\right)^2 \frac{k_f}{k_i}\left(\frac{1}{q^4}\right) \left| \int \phi_f^*(r') \exp(\mathrm{i}\mathbf{q} \cdot \mathbf{r}') \phi_i(r') d^3r' \right|^2, \quad (3.22)$$

where the finals states, unlike the discrete initial states corresponding to inner-shell orbitals, are treated as continuum. Note that (3.22) is sometimes represented as Dirac bra-ket notations.

The calculated cross section for EELS Fe $L_{2,3}$, which is transition from $2p_{1/2}$ and $2p_{3/2}$ inner orbitals, is shown in Figure 3.14 as dashed lines. The cross section derived in (3.22) does not take into account for the band structures in

the final continuum states and hence it does not completely predict the experimental Fe $L_{2,3}$ (solid line). The two sharp peaks near the EELS edge onset are termed white lines and originate from the transitions to the narrow empty *d*-bands in Fe. The first and the second peaks are L_3 ($2p_{3/2}$) and L2 ($2p_{1/2}$) transitions split due to spin-orbit coupling. The calculated cross section estimates the overall intensity profile quite well but excludes the contribution from the available density of states in the final states.

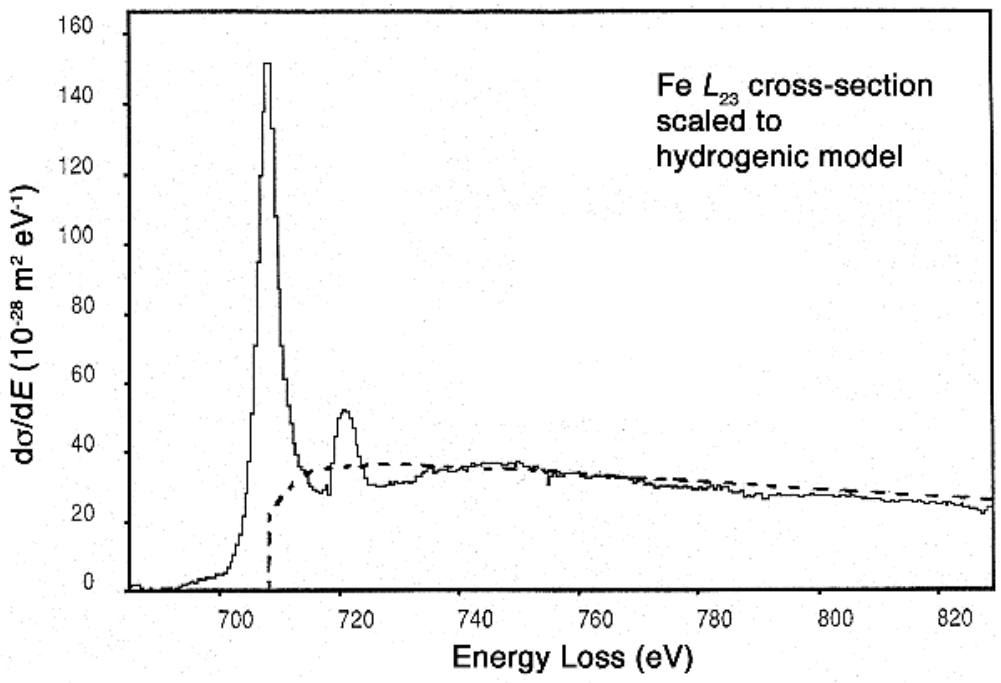

Figure 3.14. Comparison of calculated Fe $L_{2,3}$ cross section without taking into account the band structures and experimental spectra.[123]

4

Plasmon Inelastic Scattering in Annular Dark-Field Scanning Transmission Electron Microscopy

This chapter is the first chapter discussing my research results. It focuses on the modification of existing image simulation method called *Multislice* to incorporate the effects of inelastic scattering. Although it was chronologically my last project, I decided to put the chapter preceding the other earlier work since it seems appropriate to discuss about STEM image formation here. Hence, the chapter starts by the treatment of annular dark-field STEM image formations before describing the existing *Multislice* algorithm in details. It is followed by the modification of the algorithm to incorporate the plasmon scattering and the subsequent results.

4.1 Annular Dark-Field Scanning Transmission Electron Microscopy (ADF-STEM) Image Formation

The principle of ADF-STEM image formation is depicted in Figure 4.1a. An incident electron approximated as a plane wave, having a wavefunction $\psi_{inc}(\mathbf{x})$, is transformed into a focused probe $\psi_p(\mathbf{x})$ by a combination of objective aperture and lens. The probe wavefunction is obtained by integrating the aberration function $\chi(k)$ over all angles up to the maximum imposed by the objective aperture (k_{max}). The aberration function itself arises from the interplay of various microscope and lens parameters such as electron wavelength (λ), defocus (Δf), spherical aberration coefficient (C_s), coma, and astigmatisms, which is expressed as[91]

$$\chi(k) = \frac{2\pi}{\lambda}\left(\frac{1}{4}C_s\lambda^4k^4 - \frac{1}{2}\Delta f\lambda^2k^2\right), \tag{4.1}$$

ignoring the contributions from coma and astigmatism. The probe wavefunction is then described as

$$\psi_p\left(\mathbf{x}\right) = A_p \int_0^{k_{max}} \exp[-\mathrm{i}\chi(\mathbf{k})\Big] \mathrm{d}^2\mathbf{k} \tag{4.2}$$

When focused at point x_p on the specimen, the probe wavefunction is modified to

$$\psi_p(\mathbf{x}, \mathbf{x}_\mathrm{p}) = A_p \int_0^{k_{max}} \exp[-\ \mathrm{i}\chi(\mathbf{k}) - 2\pi\mathrm{i}\mathbf{k}(\mathbf{x} - \mathbf{x}_\mathrm{p})]\ \mathrm{d}^2\mathbf{k}\,, \tag{4.3}$$

where the normalization factor $A_p$is chosen so that the total integrated intensity of the probe is unity,

$$\int \left|\ \psi_p(\mathbf{x}, \mathbf{x}_\mathrm{p})\right|^2 \mathrm{d}^2\mathbf{x} = 1. \tag{4.4}$$

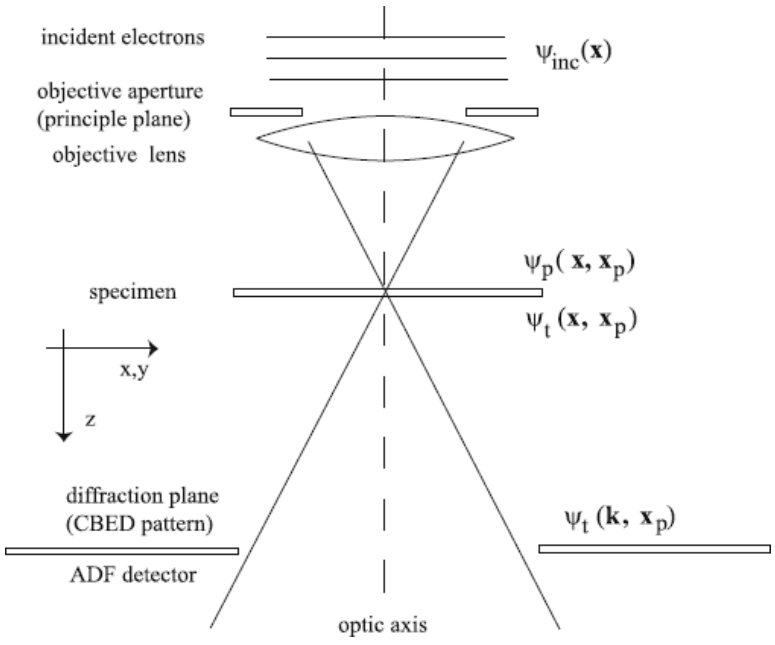

Figure 4.1. Schematic illustration of the STEM probe and electron propagation.[91]

It is more meaningful to look at the spatial distribution of the probe intensity $\left|\psi_p(\mathbf{x})\right|^2$ (instead of the wavefunction), which is better known as the point spread function (psf). Figure 4.2a shows the 2-D spatial distribution of the psf under 200 kV accelerating voltage, 1.3 mm spherical aberration coefficient, 571 Å defocus, and 9.4 mrad semi-convergence angle ($\alpha_{max} = \lambda k_{max}$). An easier representation of the 2-D psf is by performing a 1-D linescan of it as shown in Figure 4.2b. The full width at half maximum (FWHM) of the psf is referred to as the probe size. The re-appearance of intensity at the probe tails usually contributes to the smearing of the images as the probe picks up signals from locations at which it is not focused on and hence worsens the image resolution. The invention of aberration corrected STEM results in the psf profile that has lower FWHM with negligible tails to dramatically improve the image resolution.

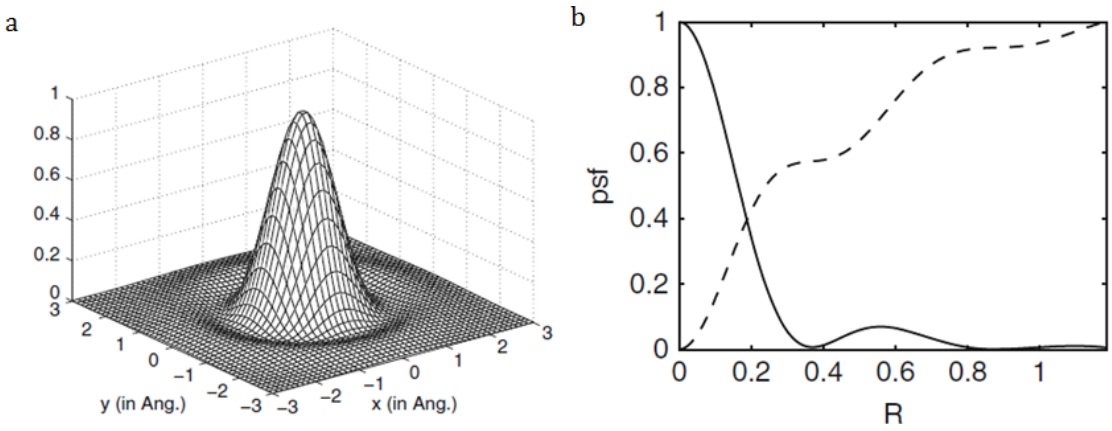

Figure 4.2. (a) The calculated 2-D STEM probe intensity using 200 keV, C_s = 1.3 mm, Δf = 571A°, and α = 9.4 mrad. (b) Point spread function (solid line) and integrated current (dashed line).[91]

When propagating through the specimen, the probe interacts with the atomic nuclei through Coulomb potential. The transmitted wavefunction $\psi_t(\mathbf{x})$ exiting the specimen can be approximated assuming the samples act as phase objects as[91]

$$\psi_t(\mathbf{x}, \mathbf{x}_\mathrm{p}) = \psi_p(\mathbf{x}, \mathbf{x}_\mathrm{p}) \exp[\mathrm{i}\sigma v_z(\mathbf{x})], \tag{4.5}$$

where $v_z(\mathbf{x})$ is the projected specimen potential acting as the phase shift argument and σ is the a parameter dictating how much the beam interacts with the specimen. One can think σ as the "cross-section" of this elastic scattering process, which is smaller for higher accelerating voltage and vice versa. A clearer mathematical description is derived in section 4.2 in (4.11). One can also think this specimen interaction as diffraction of the electron waves from the crystals. Two main types of diffraction can occur: i) coherent (Bragg scattering) and ii) incoherent diffraction. The incoherently scattered waves exit the samples at larger angles and are used to form the high-angle annular dark-field (HAADF) STEM images. More precisely, the HAADF detector integrates the intensity of the transmitted wave at diffraction planes at a given probe position x_p according to[91]

$$g(\mathbf{x}_\mathrm{p}) = \left| \psi_i(\mathbf{x}_\mathrm{p}) \right|^2 = \int D(\mathbf{k}) \left| \psi_t(\mathbf{k}, \mathbf{x}_\mathrm{p}) \right|^2 \mathrm{d}^2\mathbf{k}\,, \tag{4.6}$$

where $D(\mathbf{k})$ is the detector function, which is equal to 1 at the detector (typically 50-300 mrad for HAADF-STEM imaging) and 0 otherwise. This process of integrating the intensity is repeated as the probe moves to a different point on the sample and the recorded intensity is used to generate HAADF-STEM images. Figure 4.3 shows HAADF-STEM images of PbS nanocrystals acquired using FEI Tecnai F-30 at the University of Minnesota.

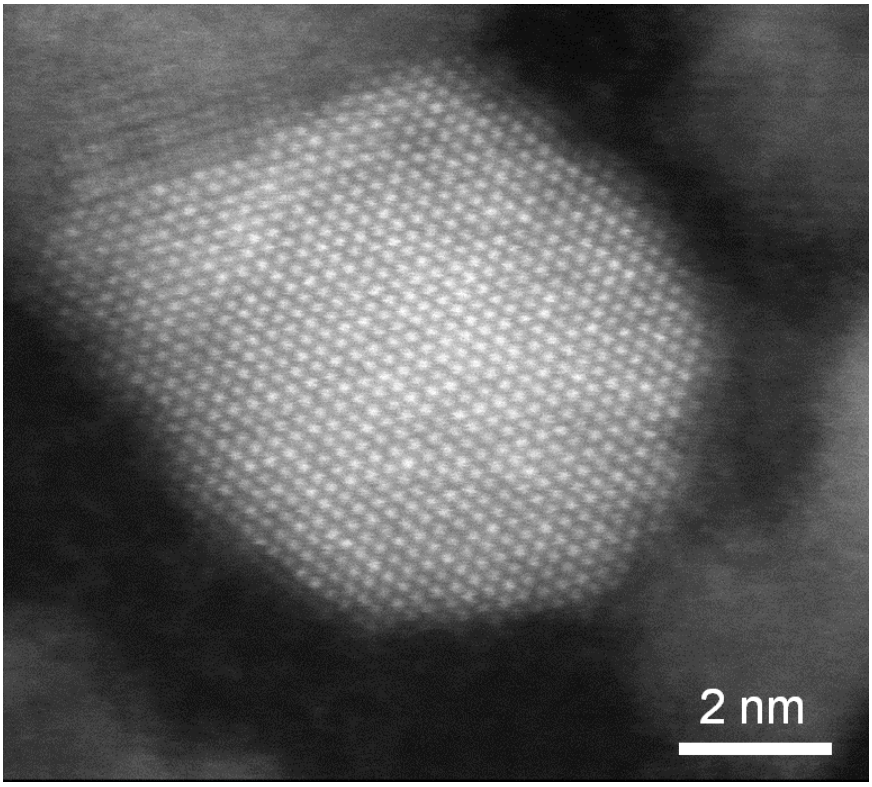

Figure 4.3. HAADF-STEM image of PbS nanocrystals acquired using FEI Tecnai F-30 at the University of Minnesota. Samples were obtained from Maksym Kovalenko at ETH-Zürich.

4.2 *Multislice* Image Simulation

Simulation of STEM images has now become a common tool to help analyze experimental images and understand various concepts in STEM image formation such as electron beam channeling[124] as well as capabilities of STEM to obtain analytical information from materials such as differentiating nanotubes[125] and tilts on single layer material.[126] There are two main methods typically used to simulate STEM, and particularly HAADF-STEM images: Bloch wave and *Multislice* methods.[91] The Bloch wave method calculates the expansion of Fourier components of the electron wavefunction and crystal potentials that match the lattice periodicity. It first started in 1928 when Bethe derived such expansion (not for electron microscope) and was later improved and modified for simulating STEM images by various groups.[127] While it can produce accurate results for small number of

beams on perfectly crystalline samples, the Bloch wave method is very inefficient for calculations involving a large number of beams (> 10) on non-periodic specimens such as defects and interfaces.[91]

The *Multislice* method offers a more efficient approach. Instead of computing expansions in reciprocal space, the *Multislice* method starts with slicing the specimens into thin parts (usually one atomic layer thick) and introduces quantum mechanical electron wave packets that transmit (by specimen potential) and propagate (to the next slice) as the electron beam passes through the samples. The method was pioneered by Cowley and Moodie[128] in 1957 and later developed extensively in the 1970's and 1980's to calculate electron diffraction and ADF-STEM images.[129] Subsequently, the expression for transmission and propagation operation will be derived starting from the time independent Schrödinger equation. The choice of using time independent (instead of time dependent) stems from the need to be more efficient without losing much accuracy. This choice is also validated by the fact that the simulated images are stationary (time-averaged).

The non-relativistic 3-D Schrödinger equation for electron wavefunction $\psi(x, y, z)$ under the influence of specimen potential $V(x, y, z)$ is[91]

$$\left[-\frac{\hbar^2}{2m}\nabla^2 - eV(x, y, z)\right]\psi(x, y, z) = E\psi(x, y, z), \tag{4.7}$$

where $\hbar = h/2\pi$ (Planck's constant divided by 2π), m is the relativistic mass of the electron, and e is the magnitude of electronic charge. This equation is considerably accurate for accelerating voltage less than 1,000 keV, which is typical for STEM experiments (60-300 keV). If the accelerating voltage is larger than 1,000 keV, relativistic Schrödinger equation might be necessary to avoid large discrepancies. Since the effect of specimen potential is to introduce a minor

perturbation on the electron trajectory that is mainly in the z-direction (along optic axis), the wavefunction $\psi(x,y,z)$ can be represented as[91]

$$\psi(x,y,z) = \psi_s(x,y,z)\exp\left(\frac{2\pi \mathrm{i} z}{\lambda}\right), \tag{4.8}$$

where $\psi_s(x,y,z)$ is the part of the wavefunction that varies slowly along z-direction. The Laplacian of the wavefunction in (4.8) is

$$\nabla^2\psi_s(x,y,z) = \exp\left(\frac{2\pi \mathrm{i} z}{\lambda}\right)\nabla_{xy}^2\psi_s(x,y,z) + \frac{\partial^2}{\partial z^2}\left[\psi_s(x,y,z)\exp\left(\frac{2\pi \mathrm{i} z}{\lambda}\right)\right], \tag{4.9}$$

where ∇_{xy}^2 is the sum of the second derivative with respect to x and y.

After calculating the second term on the right hand side of (4.9), the Schrödinger equation in (4.7) can now be rewritten as

$$-\frac{\hbar^2}{2m}\left[\nabla_{xy}^2 + \frac{\partial^2}{\partial z^2} + \frac{4\pi \mathrm{i}}{\lambda}\frac{\partial}{\partial z} + \frac{2meV(x,y,z)}{\hbar^2}\right]\psi_s(x,y,z) = 0. \tag{4.10}$$

Further simplifications can be made by considering that the electron motion is predominantly in the forward direction and λ is very small, resulting in

$$-\frac{\hbar^2}{2m}\left[\nabla_{xy}^2 + \frac{4\pi \mathrm{i}}{\lambda}\frac{\partial}{\partial z} + \frac{2meV(x,y,z)}{\hbar^2}\right]\psi_s(x,y,z) = 0. \tag{4.11}$$

The omission of $\partial^2/\partial z^2$ term can sometimes be considered as neglecting the backscattered electrons; a good assumption for HAADF-STEM imaging at high accelerating voltages. It is more meaningful to write (4.11) as a first order differential equation (for the purpose of *Multislice* algorithm)[91]

$$\frac{\partial \psi_s(x,y,z)}{\partial z} = \left[\frac{\mathrm{i}\lambda}{4\pi}\nabla_{xy}^2 + \mathrm{i}\sigma V(x,y,z)\right]\psi_s(x,y,z), \tag{4.12}$$

where $\sigma = 2\pi me\lambda/h^2$ is the parameter appearing in (4.5) that describes how much the beam interacts with the sample at a given accelerating voltage (or a given wavelength). Equation (4.12) is central to the formulation of multislicle algorithm and the rest of this chapter.

4.3 The Existing Algorithm

The solution to (4.11) takes the form of[91]

$$\psi_s(x,y,z) = \exp\left[\int_0^z \left(\frac{\mathrm{i}\lambda}{4\pi}\nabla_{xy}^2 + \mathrm{i}\sigma V(x,y,z')\right)\mathrm{d}z'\right]\psi_s(x,y,0). \tag{4.13}$$

Rewriting (4.13) from z to $z + \Delta z$ and performing the integration gives

$$\psi_s(x,y,z+\Delta z) = \exp\left[\frac{\mathrm{i}\lambda}{4\pi}\Delta z\nabla_{xy}^2 + \mathrm{i}\sigma v_{\Delta z}(x,y,z)\right]\psi_s(x,y,z), \tag{4.14}$$

where $v_{\Delta z}(x,y,z') = \int_z^{z+\Delta z} V(x,y,z')\mathrm{d}z'$is the projected atomic potential previously appearing in (4.5) as the argument in the phase shift factor when the electron beam encounters the specimen.

After appropriate expansions of the exponential term and some manipulations, (4.14) can be expressed as

$$\psi_s(x,y,z+\Delta z) = \exp\left(\frac{\mathrm{i}\lambda}{4\pi}\Delta z\nabla_{xy}^2\right)t(x,y,z)\psi_s(x,y,z), \tag{4.15}$$

where the transmission function $t(x,y,z)$ is defined as $\exp\left[\mathrm{i}\sigma\int_{z}^{z+\Delta z}V(x,y,z')\mathrm{d}z'\right]$. In order to gain insight into the other exponential factor, it is useful to take a (non-trivial) Fourier transform of (4.15)

$$\mathrm{FT}[\psi_s(x,y,z+\Delta z)]=\mathrm{FT}\left[\exp\left(\frac{\mathrm{i}\lambda}{4\pi}\Delta z\nabla_{xy}^2\right)(t\psi_s)\right]=\exp\left[-\mathrm{i}\pi\lambda\Delta z\left(k_x^2+k_y^2\right)\right]\mathrm{FT}[t\psi_s]$$
$$=P(k,\Delta z)\ \mathrm{FT}[t\psi_s], \qquad (4.16)$$

where $P(k,\Delta z)$ is the propagator function in reciprocal space. Rewriting (4.16) back into real space gives

$$\psi_s(x,y,z+\Delta z)=p(x,y,\Delta z)\otimes[t(x,y,z)\psi_s(x,y,z)], \qquad (4.17)$$

where $p(x,y,\Delta z)$ is the propagator function in real space and represented as

$$p(x,y,\Delta z)\otimes\ =\ \frac{1}{i\lambda\Delta z}\exp\left[\frac{\mathrm{i}\pi}{\lambda\Delta z}(x^2+y^2)\right]\otimes=\exp\left(\frac{\mathrm{i}\lambda}{4\pi}\Delta z\nabla_{xy}^2\right). \qquad (4.18)$$

For a better *Multislice* interpretation, (4.17) can be written in a layer-by-layer and more compact form as[91]

$$\psi_{n+1}(x,y)=p_n(x,y,\Delta z_n)\otimes[t_n(x,y)\psi_n(x,y)], \qquad (4.19)$$

where n = 0, 1, 2,... is the slice number in the specimen each having slice thickness of Δz_n (usually each slice has the same thickness). *Multislice* equation (4.19) is the most important equation as it depicts how the wavefunction is mathematically formulated when it passes through the specimen. This is also the equation that will be modified by incorporating inelastic scattering as will be apparent in Section 4.5.

4.4 Influence of Plasmon Inelastic Scattering to HAADF-STEM Imaging

Thus far, the existing *Multislice* method in (4.19) only considers for elastic scattering as the main electron beam-sample interaction with the exception of the inclusion of thermal diffuse scattering (due to lattice vibrations or phonons) at non-zero temperature in *Multislice* method developed by Kirkland.[130] The phonon scattering is not incorporated explicitly in (4.19) but rather implicitly though frozen phonon method. Phonon scattering plays a pivotal role in the generation of Kikuchi bands and thermal diffuse scattering in the output of *Multislice* simulation. However, even after incorporating phonon scattering, some discrepancies still exist in the contrast of *Multislice* simulated HAADF-STEM images.[131] One possible explanation is that mutislice method still neglects plasmon scattering, which is another type of inelastic scattering as discussed in Chapter 3. We will only consider bulk plasmon scattering in this chapter neglecting the contribution from surface plasmon.

The contribution of plasmon scattering to HAADF-STEM images was first measured in 1991 by Xu *et al.* using energy filtered convergent beam electron diffraction (CBED) on Si(100) samples.[132] CBED itself is an electron diffraction pattern formed using focused probe commonly used in STEM imaging. The parallel beam counterpart is often referred as selected-area diffraction (SAD) and more familiar for non-microscopists to analyze the crystallinity of the samples and sample orientation. CBED patterns, though less familiar, are actually more powerful since crystal symmetry, bonding, and composition could be determined from them.[89] In mathematical terms, CBED pattern is represented by $\left|\psi_t(\mathbf{k}, \mathbf{x}_\mathrm{p})\right|^2$, which is used to obtain the intensity of HAADF-STEM images at particular probe position x_p. Figure 4.4a shows the schematic formation of CBED patterns from a focused probe for a relatively small probe convergence angle α. At medium α the CBED patterns start to overlap with nearest neighbors (Figure 4.4b). In the limit of large α, next nearest neighbors then start to overlap (Figure

4.4c). For high resolution HAADF-STEM, it is necessary to have overlapping disks such as shown in Figure 4.4b.

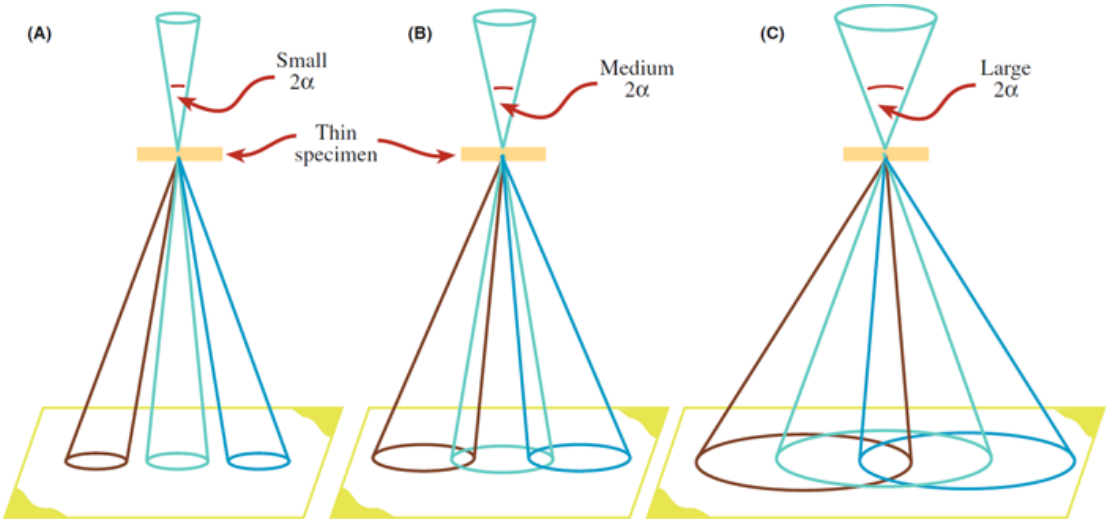

Figure 4.4. Schematic illustrations of CBED pattern formations under differing illumination angles.[89]

Figure 4.5a and b show simulated CBED patterns from Si without and with thermal vibrations respectively. In the absence of phonon at hypothetically 0 K, the CBED patterns consist of only the disks and rings associated with Laue zones (Figure 4.5a). When phonons are incorporated there are additional lines referred as Kikuchi bands, which arise from electrons that have been scattered by phonons (inelastic) and subsequently undergo elastic Bragg scattering (Figure 4.5b), Figure 4.5c shows experimental CBED patterns from 30 nm thick Si(100) samples.[132] The disc at the center is the direct beam or central diffraction disc containing non-Bragg diffracted beams while the rest of the disks have been Bragg-diffracted. The Kikuchi bands can be clearly observed since the experiment was done at room temperature. While CBED patterns in Figure 4.5c were obtained from elastically scattered electrons (zero loss signals in EELS – as explained in Chapter 4), Figure 4.5d were acquired from inelastically scattered electrons in the region of 12-20 eV energy loss, which mostly contain 1st plasmon scattering ($E_{p,c\text{-}Si}$ = 16.6 eV). Overall patterns are preserved in the case

of 1st plasmon scattered CBED with the exception of more blurry patterns particularly visible near the central diffraction disc. This should be of no surprise since 1st plasmon CBED patterns consist of electrons having undergone inelastic plasmon and elastic Bragg scattering (in no particular order). Consequently, there are more diffuse scattering introduce by the plasmon interaction when compared to the "zero loss plasmon" in Figure 4.5c whereby the electrons have only undergone Bragg scattering.

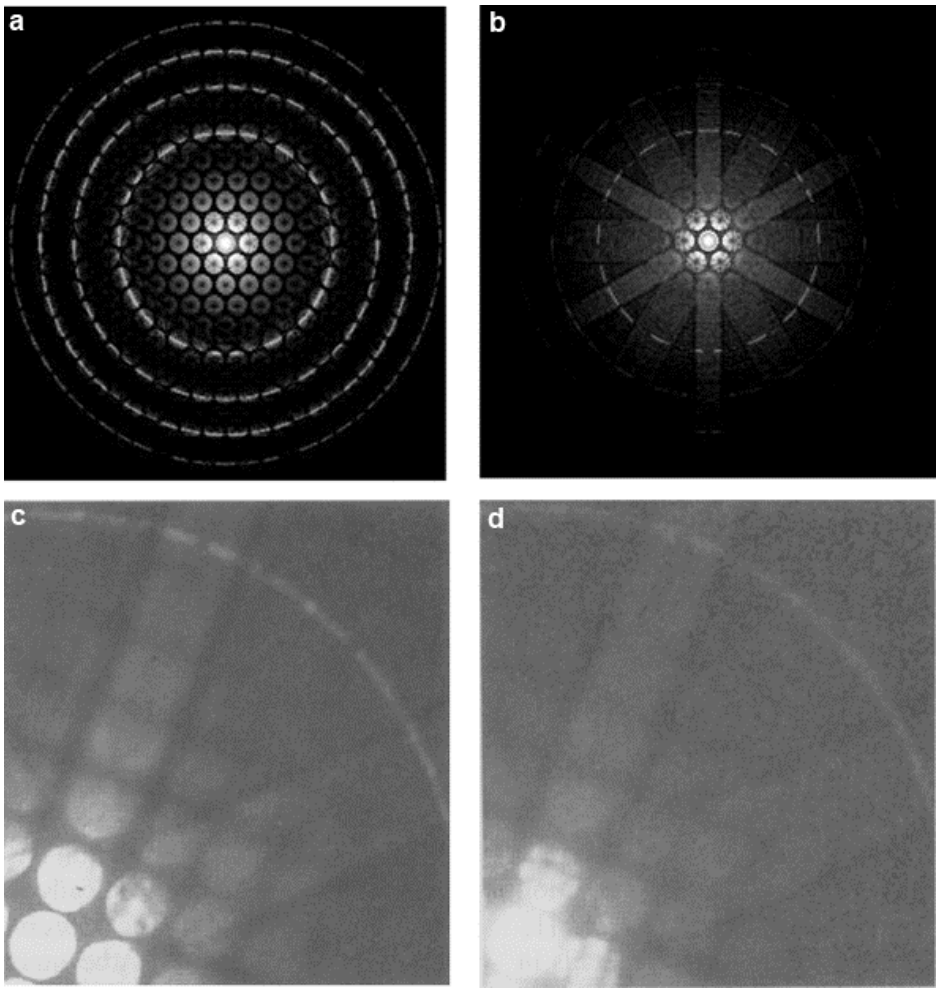

Figure 4.5. Simulated CBED patterns (a) without and (b) with phonon showing the appearance of Kikuchi bands from Si <111> using 100 kV, 3.3 mm C_S, and 8 mrad probe convergence angle. Experimental energy-filtered CBED patterns for Si<100> from (c) zero-loss and (d) 1st plasmon obtained using 100 kV, 3.3 mm C_S, and 7 mrad convergence angle.[91, 132]

The CBED patterns in Figure 4.5 are sometimes presented in 1-D format in Figure 4.6 after azimuthal integration for a more compact presentation. The zero-loss and 1st plasmon curves were obtained from the CBED patterns in Figure 4.5c and d. The intensity minimum after the first peak in the 1st plasmon curve is only one order of magnitude lower than the maximum. In the case of the zero loss curve, the intensity minimum after the first peak is about two orders of magnitude lower indicating that zero loss CBED patterns are sharper than the 1st plasmon patterns. The magnitude of the first plasmon signals is about 22 % of the zero loss signals throughout all the scattering angles. Using Poisson statistics, the calculated ratio of 1st plasmon with respect to the zero loss intensity for 30 nm Si was found to be 24 % (see Section 3.1), in close agreement with the experimental value of 20 % from Xu *et al.*[132]

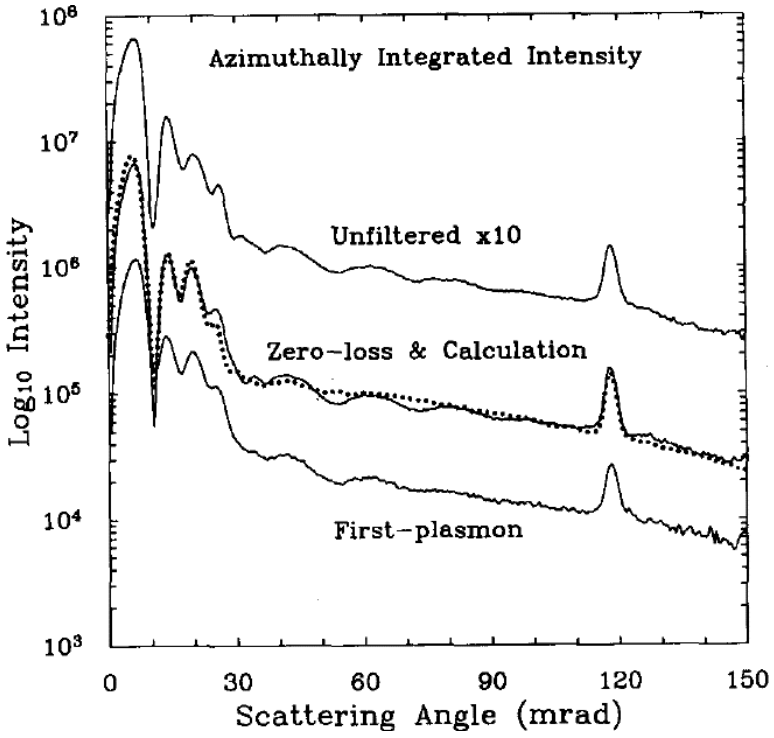

Figure 4.6. Azimuthally integrated CBED intensity from patterns in Figure 4.5c and d.[132]

4.5 The Algortihm for Modified Elastic-Inelastic *Multislice* Method

The bulk plasmon scattering cross section generated by fast electrons can be expressed as[106]

$$B(E,\mathbf{k}) = \frac{d^2\sigma}{d\theta dE} =$$

$$\frac{\sin\theta}{E_0\pi n_a a_0}\left(\frac{1}{\theta^2+\theta_E^2}\right)\left[\frac{E(\Delta E_{\mathrm{P}})E_{\mathrm{P},0}^2}{\left(E^2-E_{\mathrm{P},0}^2-\gamma 4E_{\mathrm{P},0}E_0(\theta^2+\theta_E^2)\right)^2+(E\Delta E_{\mathrm{P}})^2}\right] \quad (4.20)$$

where $n_a$is the atomic density of the specimens, a_0 is the Bohr radius, E_0 is the incident electron energy, $E_{\mathrm{P},0}$is the plasmon energy at $q=0$, ΔE_{P} is the plasmon damping coefficient, $\theta=\lambda k$ is the scattering angle, γ is a density-dependent constant equal to $3E_F/5\,E_{\mathrm{P},0}$, and $\theta_E=(E/E_0)[(E_0+m_oc^2)/(E_0+2m_oc^2)]$ is the plasmon characteristic angle. This expression is previously discussed in Section 3.1.3. The effect of plasmon scattering is to induce energy loss and redistribute the angles on the *intensity* of the incoming electron through the relation[133]

$$I_{in,n+1}(E,\mathbf{k}) = I_{el,n}(\mathbf{k})\otimes B(E,\mathbf{k})\beta_1(\Delta z) \quad (4.21a)$$

$$I_{in,n+1}(E,\mathbf{x}) = \mathrm{FT}^{-1}\{I_{in,n+1}(E,\mathbf{k})\} = I_{el,n}(\mathbf{x})B(E,\mathbf{x})\beta_1(\Delta z) \quad (4.21b)$$

where $I_{in,n+1}$ is the intensity of the plasmon inelastically scattered electrons at slice $n+1$, $I_{el,n}(\mathbf{k})$ is the intensity of elastically scattered electrons at slice n, and $\beta_1(\Delta z)$ is the probability of a single plasmon scattering within slice thickness Δz. The value of $\beta_1(\Delta z)$ can be approximated by the Possion's statistics of plasmon plural scattering (see Section 3.1.5) in the limit of small Δz in which only a single scattering occurs

$$\frac{I_1}{I_{total}} = \beta_1(\Delta z) = \frac{\Delta z}{\lambda_{pl}}e^{-\Delta z/\lambda_{pl}} \quad (4.22a)$$

$$\frac{I_0}{I_{total}} = \beta_0(\Delta z) = e^{-\Delta z/\lambda_{pl}}, \tag{4.22b}$$

where λ_{pl} is the plasmon inelastic mean free path. The factor β_1 can also be thought as an absorption factor to account for the plasmon scattering.

In order to account for plasmon scattering, the wavefunction in (4.19) has to be modified by inserting an additional dimension to include the energy loss terms. Using the relation $|\psi(\mathbf{x})|^2 = I(\mathbf{x})$, the "inelastic-elastic" *Multislice* algorithm can be written as

$$\psi_{n+1}(E = 0, \mathbf{x}) = p_n(\mathbf{x}, \Delta z_n) \otimes \left[t_n(\mathbf{x}) \left[\psi_n(E = 0, \mathbf{x}) \sqrt{\beta_0} \right] \right], \tag{4.23a}$$

$$\psi_{n+1,single}(E_i > 0, \mathbf{x}) =$$

$$p_n(\boldsymbol{x}, \Delta z_n) \otimes \left[t_n(\mathbf{x}) \left[\psi_n(E = 0, \mathbf{x}) \sqrt{B(E_i, \mathbf{x}) \beta_1} \right] \right], \tag{4.23b}$$

where (4.23a) is the usual elastic-only method with additional intensity reduction factor of $\sqrt{\beta_0}$ to account for the inelastic scattering. The algorithm (4.23b) only describes the single plasmon scattering. In order to include the effects of multiple scattering, additional plural inelastic terms must be computed

$$\psi_{n+1,plural}(E_i > 0, \mathbf{x}) =$$

$$\sum_{E_i > E_k} p_n(\mathbf{x}, \Delta z_n) \otimes \left[t_n(\mathbf{x}) \left[\psi_{n,single}(E_k, \mathbf{x}) \sqrt{B(E_i - E_k, \mathbf{x}) \beta_1} \right] \right]. \tag{4.24}$$

Algorithm (4.24) can be interpreted as the plural inelastic scattering for a given energy loss E_i at slice $n + 1$ can be calculated from the sum of all single scattered electrons having energy $E_k < E_i$ from previous slice n which undergo another scattering.

The main modifications of inelastic-elastic *Multislice* are the computations of bulk plasmon cross section (4.20) and its incorporation to the *Multislice* algorithms (4.23) and (4.24). The probe in this simulation was formed using 100 kV accelerating voltage, 1.3 mm C_s, 850 Å defocus and 11.4 mrad convergence angle. The effects of chromatic aberration and finite source size are excluded. The bulk plasmon cross section (4.20) of Si(100) under these conditions is shown in Figure 3.1.

The steps involved in the modified inelastic-elastic methods updating the elastic-only method are (see also Figure 4.7)

1. Calculate the bulk plasmon cross section in reciprocal space $B(E,\mathbf{k})$ according to (4.20) and apply inverse Fourier transform to obtain the real space expression $B(E,\mathbf{x})$. Take the square root of the real space cross section $\sqrt{B(E,\mathbf{x})}$.
2. Calculate the transmission function $t(\mathbf{x},z)$ within each slice according to (4.15).
3. Compute the probe wavefunction entering the first slice $\psi_0(E=0,\mathbf{x})$ with only the elastic part having nonzero elements for position x_p on the specimen.
4. Perform one inelastic-elastic mutlisce algorithm by calculating the elastic-only part according to (4.23a)

   $$\psi_{n+1}(E=0,\mathbf{x}) = \mathrm{FT}^{-1}\{P_n(\vec{k},\Delta z_n)\mathrm{FT}[t_n(\mathbf{x})\psi_n(E=0,\mathbf{x})\sqrt{\beta_0}]\}, \qquad (4.25a)$$

   and the single scattering plasmon according to (4.23b)

   $$\psi_{n+1,single}(E_i>0,\mathbf{x}) =$$

   $$\mathrm{FT}^{-1}\left\{P_n(\mathbf{k},\Delta z_n)\mathrm{FT}\left[t_n(\mathbf{x})\psi_n(E=0,\mathbf{x})\sqrt{B(E_i,\mathbf{x})\beta_1}\right]\right\} \qquad (4.25b)$$

5. Calculate the contribution from plural scattering according to (4.24)

$$\psi_{n+1,plural}(E_i > 0, \mathbf{x}) =$$

$$\sum_{E_i > E_k} \mathrm{FT}^{-1}\left\{P_n(\mathbf{k}, \Delta z_n) FT\left[t_n(\mathbf{x})\psi_{n,single}(E_k, \mathbf{x})\sqrt{B(E_i - E_k, \mathbf{x})\beta_1}\right]\right\} \quad (4.26)$$

where this quantity is zero for the first slice.

6. *Independently* transmit and propagate (4.25) and (4.26) to the next slice and then repeat steps 4 and 5 until the end of the specimen is reached.
7. Fourier transform the wavefunctions in (4.25) and (4.26) exiting the specimen to obtain the far-field wavefunction at the diffraction planes.
8. Calculate the intensity (square modulus) of the total wavefunctions (elastic and inelastic) at the diffraction planes to obtain the signal for one pixel corresponding to point x_p on the specimen/image. "Energy-filtered" STEM images can also be computed by selecting the energy loss range intended to construct the images.
9. Repeat steps 3-8 for each position on the specimens.
10. CBED patterns and EELS signals averaged over the entire scanned image are also calculated.

The modified inelastic-elastic algorithm is qualitatively illustrated in Figure 4.8. The treatment of the elastic ($E = 0$) wavefunctions mimics the existing *Multislice* method as shown in Figure 4.8 for part of the incident probe wavefunction normal to the surface of the first slice of the specimen. After interacting with the specimen potentials (transmission), the wavefunction is scattered (shown as three different exit paths of the wavefunctions) and undergoes phase shifts (effects not shown). These scattered wavefunctions are then propagated onto the next slices. For the inelastic portions, slight broadening of the wavefunction induced by the plasmon scattering is present (shaded cones). The size of the broadening depends on how much energy loss incurred with maximum broadening occurs near the plasmon energy.

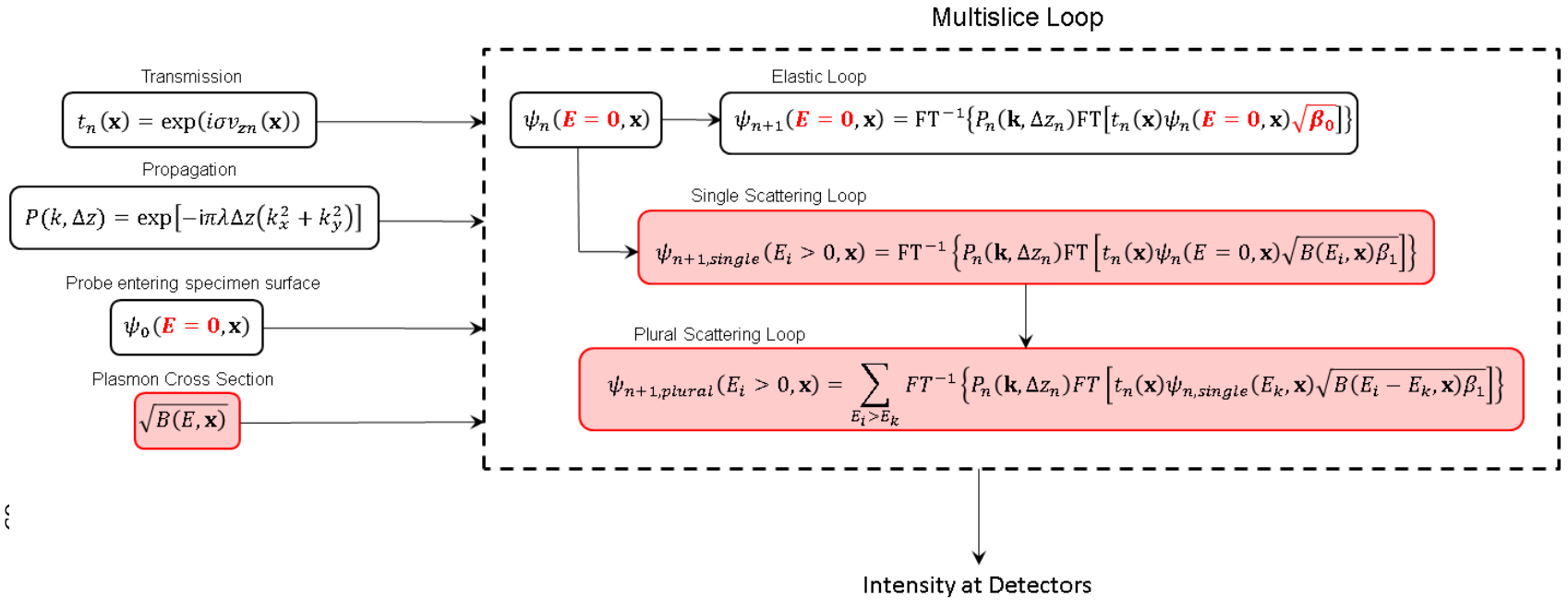

Figure 4.7. Algorithm sequences for modified inelastic-elastic *Multislice* method. The main multislice loop is shown for a particular probe position x_p on the specimen.

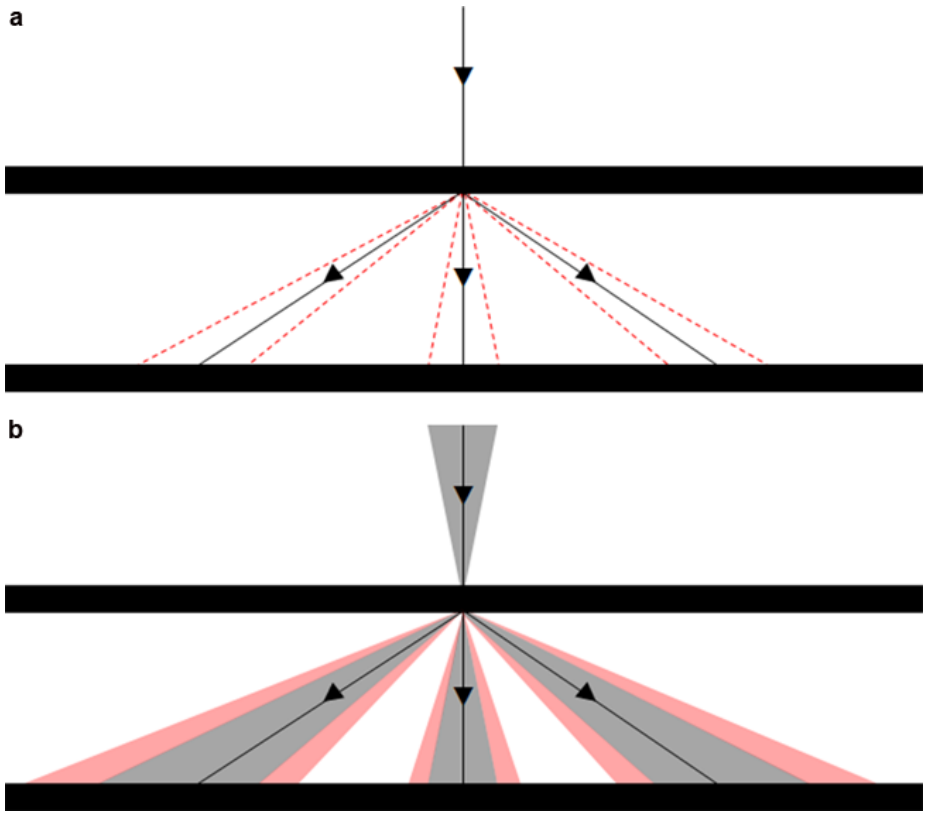

Figure 4.8. Schematic illustration of the effects of plasmon scattering on the broadening of beams for (a) one specific wavevector and (b) conical wavevector representing STEM probe. The red-dotted lines and shaded areas represent the effects of inelastic scattering.

Si(100) with thicknesses of 20, 30, 40, and 50 nm were examined using the modified inelastic-elastic *Multislice* algorithm. While thicker specimens will have more significant contributions from the plasmon scattering, we limit our attention to typical thicknesses used in TEM experiments. The supercell size is 65.16×65.16 Å^2 with 1024×1024 grid size and 1.3575 Å slice thickness. For HAADF-STEM imaging, the STEM probe is scanned at 8 pixel/Å across the specimen Collected electrons scattered between 54 and 150 mrad are used to form HAADF-STEM images.

For the computation of inelastic scattering, the plasmon is allowed to scatter from 0 to 40 eV energy loss with 1 eV dispersion. This range includes up to the double scattering signals, which is a good approximation for the range of thicknesses under consideration. It may be necessary to include the triple scattering signals once the thickness reaches half of λ_{pl}, or about 60 – 70 nm in crystalline Si. EELS signals are computed from electrons scattered in the 0 – 20 mrad range. "Energy-filtered" CBED and STEM images are simulated using 10 eV energy slit centered on the 1st (16 eV energy loss) and 2nd (32 eV energy loss).

4.6 Simulated Electron Energy Loss Spectroscopy

EELS spectra for three different thicknesses of 32, 42, and 73.5 nm were simulated according to the modified elastic-inelastic *Multislice* method for 100 kV accelerating voltage as shown in Figure 4.9 (red lines). This was done by calculating the intensity of the wavefunction after passing through the samples for each energy loss in the range of 0 – 21.5 mrad, which is the EELS collection angles. The first plasmon peaks increase as a function of the thickness and agree with experimental data (blue lines) obtained under similar conditions.[106] The modified algorithm also calculates the plasmon plural scattering until *n*th scattering. However, since the 3rd plasmon peak is not significant unless the thickness is roughly equal to the plasmon mean free path (120 nm) and to be computationally efficient, only double scattering is considered. The intensity ratio of the 2nd plasmon to the 1st plasmon for simulated and experimental EELS are in agreement specifically for the thickness range considered.

The modified inelastic-elastic algorithm, however, excludes the contributions from surface loss. This is apparent in the underestimation of the signals in the range of 3-10 eV energy loss when compared to the experimental data. Efforts to include surface loss are under consideration to complete the plasmon loss modifications to *Multislice* method. Additionally, the modified algorithm does not take into account the chromatic aberration and hence the

finite width of the zero-loss peaks. This results in the smaller FWHM of the simulated 1st plasmon peaks in comparison to the experimental data. The slight discrepancy in the energy loss position of the second plasmon peak, as deduced from the 73.5 nm spectrum, arises from the finite sampling (1 eV dispersion) of the modified algorithm.

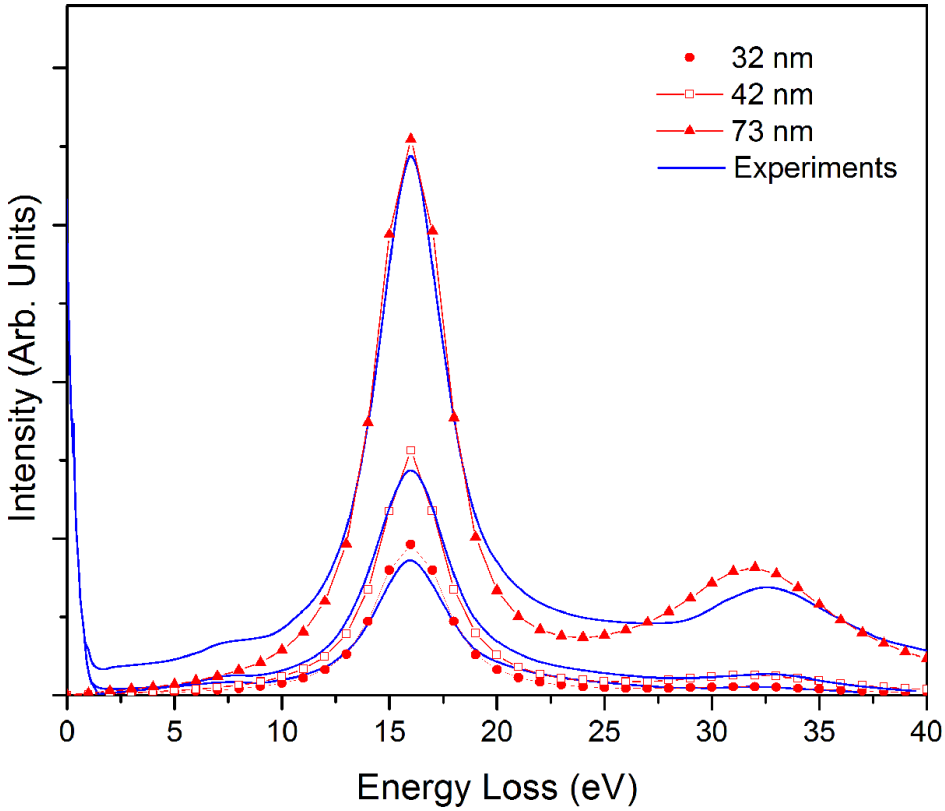

Figure 4.9. Simulated EELS spectra of 32, 42, and 73.5 nm Si (red data points) and the comparison with the experimental spectra (blue lines). [106]

4.7. Effects of Plasmon Scattering on CBED Patterns

The central step in the modified inelastic-elastic *Multislice* method is that the elastically scattered beams are allowed to undergo plasmon within a slice. This interplay between elastic and plasmon scattering manifests in the broadening of the CBED discs. Figures 4.10a-c show energy-filtered CBED

patterns from 50 nm crystalline Si along <100>, which were calculated for zero-loss, 1st plasmon, and 2nd plasmon energy loss. A focused beam with 7.5 mrad convergence angle and 3.3 mm C_S were used to compute the non-overlapping CBED patterns. The edges of the CBED discs from the zero-loss patterns look sharp since the diffuse scattering induced by the plasmon is absent (Figure 4.10a). In the 1st plasmon pattern, however, the edges become slightly blurred with significant intensity emerging in between the Bragg discs (Figure 4.10b). The 2nd plasmon CBED patterns display more significant intensity and edge blurring as shown in Figure 4.10c. This broadening can also be observed

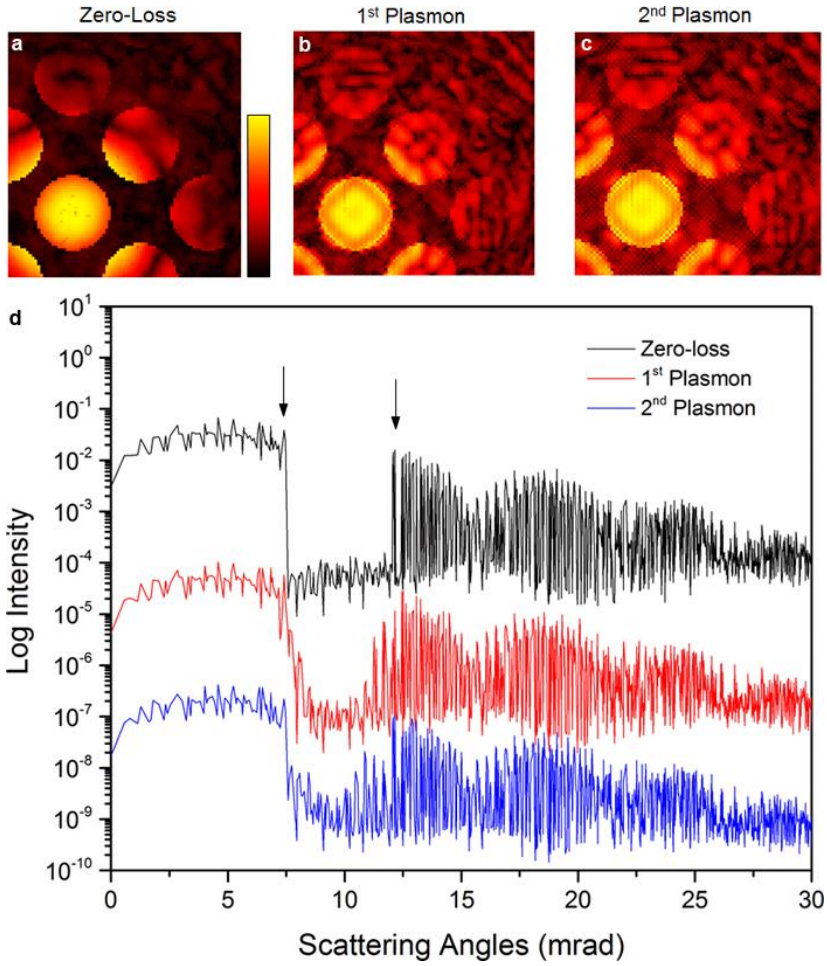

Figure 4.10. Simulated CBED patterns for (a) zero-loss, (b) 1st plasmon, and (c) 2nd plasmon showing the diffuse scattering. (d) Azimuthally integrated patterns from a-c.

more clearly in the azimuthally integrated CBED patterns in Figure 4.10d. The edge profiles of the central discs broaden as a function of the number of plasmon scattering. The difference between the intensity minimum at 12 mrad and the first peak at 4 mrad is about three orders of magnitude, which is bigger than that of the 2nd plasmon CBED patterns. A smaller difference is observed for the zero-loss and 1st plasmon patterns.

4.8. HAADF-STEM Imaging

Plasmon loss is a relatively forward scattering process as seen in Figure 3.1 with a critical angle of about 6 mrad for Si under 100 kV electron beam. As a result, formations of HAADF-STEM images that utilize high scattering angles above 50 mrad *are thought* to have insignificant contributions from plasmon scattering. Most efforts to include plasmon contributions in *Multislice* simulations focused on bright-field imaging whereby the low scattering angles (< 20 mrad) have considerable contributions from the forward-scattered plasmon loss.[95] However, the results from the modified inelastic-elastic *Multislice* method show that plasmon loss contributes significantly to the high-angle signals.

Figure 4.11 shows the azimuthally integrated energy-filtered CBED patterns (zero-loss and 1st plasmon) from 30 and 50 nm Si<100> obtained using 11.4 mrad convergent angle and 1.3 mm C_S. The CBED patterns from 1st plasmon exhibit similar profiles to the zero-loss patterns regardless of the thickness. At 30 nm, the total ratio of 1st plasmon to zero loss intensity, $(I_1/I_0)_{total}$, is 20 % while the high angle intensity ratio $(I_1/I_0)_{54-150}$ is about 16 %. Experimental energy-filtered CBED patterns on 30 nm thick Si collected under similar conditions show comparable ratio for $(I_1/I_0)_{total}$ at 22 % (see Figure 4.6).[132] However, unlike the simulated CBED, the value of experimental $(I_1/I_0)_{54-150}$ is the same as $(I_1/I_0)_{total}$ at 20 %. Increasing the thickness to 50 nm results in higher simulated $(I_1/I_0)_{total}$ of 50 % and $(I_1/I_0)_{54-150}$ of 37 %.

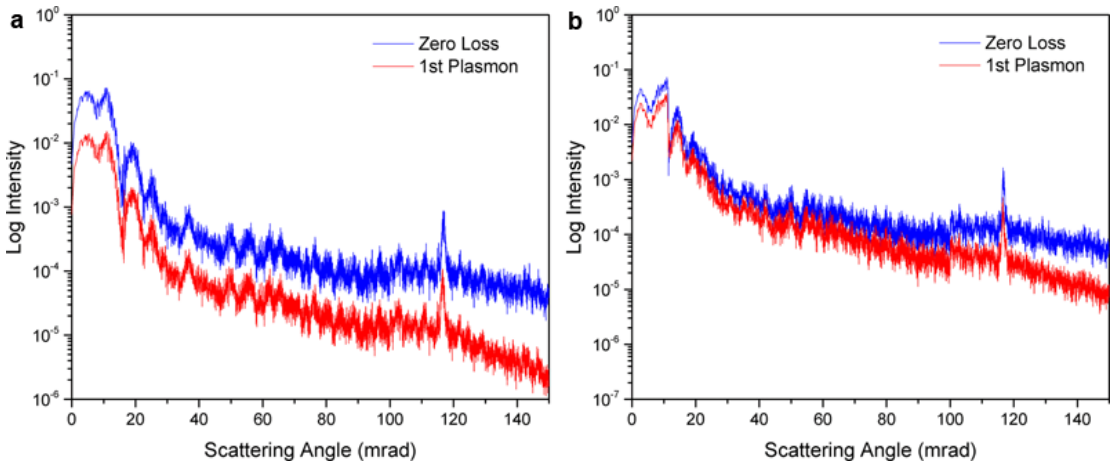

Figure 4.11. Azimuthally integrated energy-filtered CBED patterns for (a) 30 and (b) 50 nm thick Si specimens.

Figure 4.12 summarizes the simulated intensity ratio for four different thicknesses, which are compared with experiments (only 30 nm data are available) and theoretical ratio based on Poisson distribution. The difference between $(I_1/I_0)_{total}$ and $(I_1/I_0)_{54-150}$ increases as the thickness increases and the simulated $(I_1/I_0)_{total}$becomes larger than $(I_1/I_0)_{Poisson}$at thickness greater than 40 nm. This discrepancy could be attributed to several factors. The simulation only used 1 phonon configuration to save some computational time and hence, with the inclusions of more phonon configurations, the discrepancy can be minimized. With more phonon configurations, the images have more realistic representation of the atomic vibrations. Additionally, the use of larger grid sizes to 2048 x 2048 was calculated to reduce the discrepancy but the computational time increases by a factor of four (data not shown).

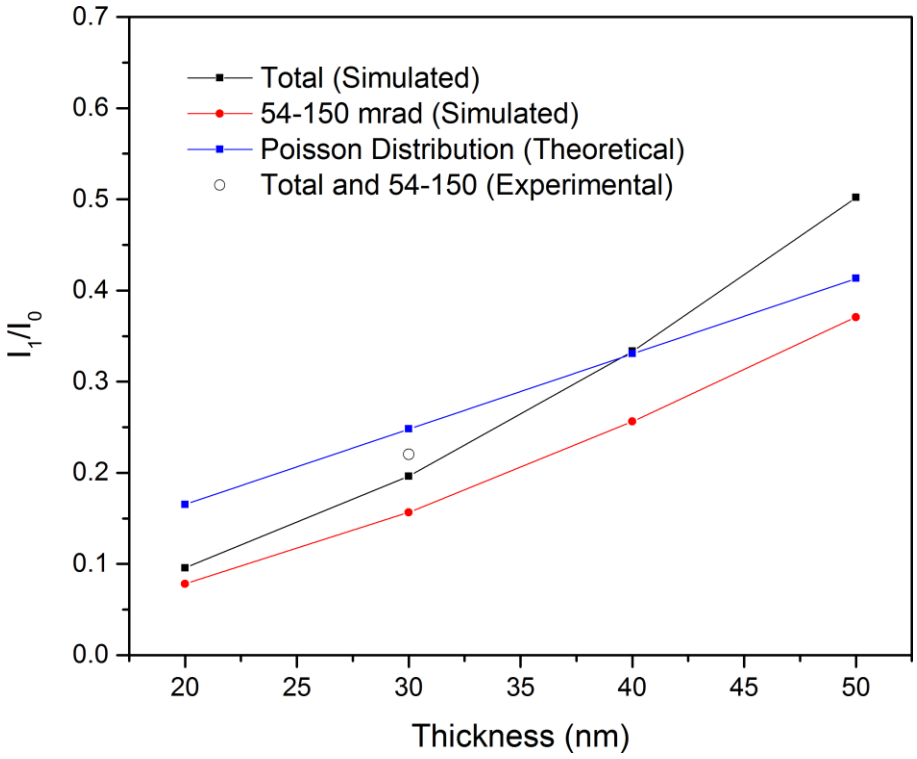

Figure 4.12. Summary of intensity ratio of 1st plasmon to zero-loss for total (whole angles), high-angle region (54-150 mrad), and the comparison with theoretical Poisson distribution and experimental data (only for 30 nm). [132]

HAADF-STEM images for 50 nm Si<100> simulated using the modified inelastic-elastic *Multislice* method are shown in Figure 4.13a obtained using 11.4 mrad convergence angle and 1.3 mm C_S, which are the same probe used to form CBED patterns in Figure 4.11. HAADF-STEM image simulated using existing elastic-only *Multislice* method (Figure 4.13b) is used for comparison. Note that at this thickness, the plasmon scattering intensity is about 37 % of the elastic (or zero-loss) intensity or contributes about 27 % to the total image intensity. This indicates that plasmon scattering should have considerable impact. Inelastic scattering, at first, seems to smear out the high resolution STEM images although overall high-resolution atomic columns are surprisingly preserved in the HAADF-STEM images.

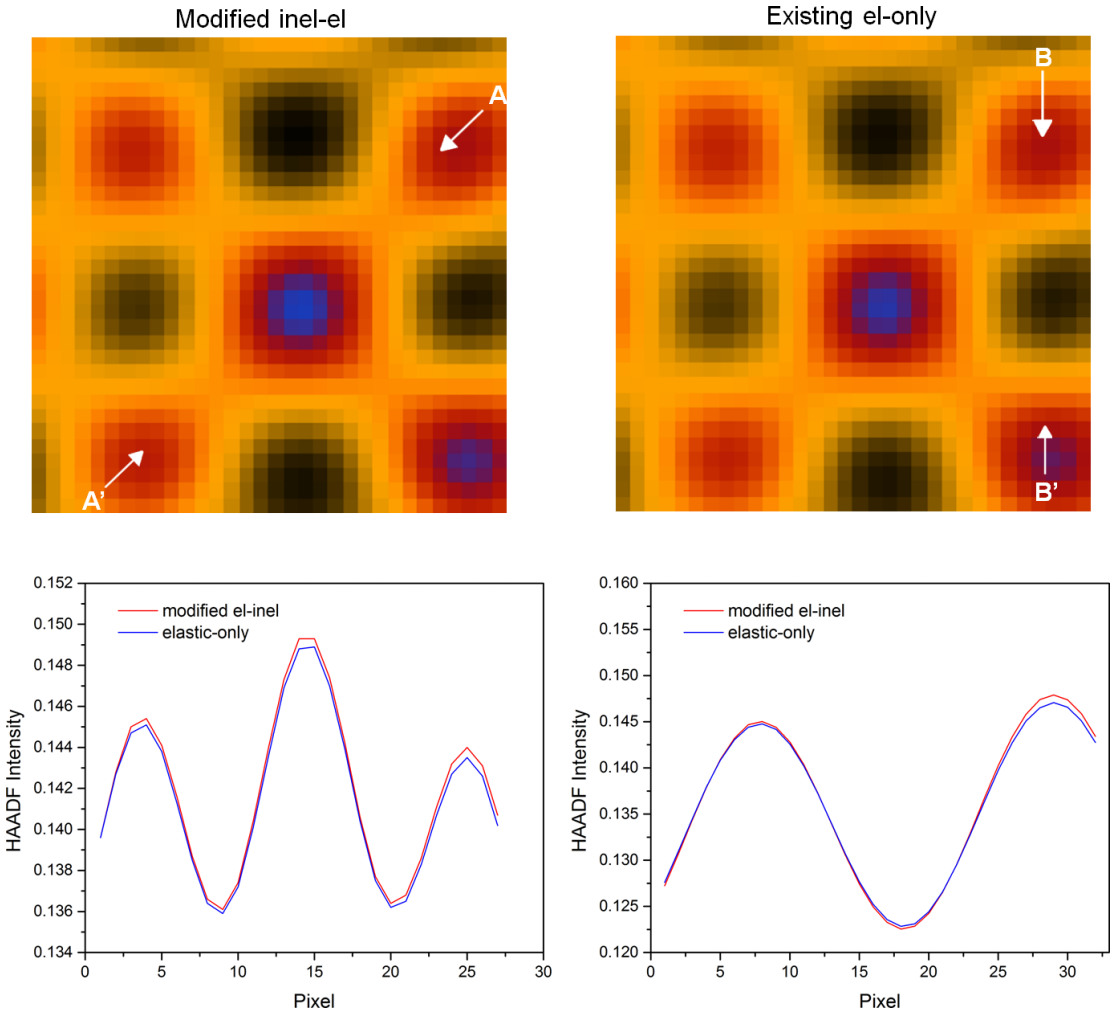

Figure 4.13. Simulated HAADF-STEM images of 50 nm Si<100> using (a) modified elastic-inelastic and (b) existing elastic-only *Multislice* method. The color scale is identical for both images. Intensity linescan profiles along points (c) A-A' and (d) B-B' in figures (a) and (b).

Intensity linescan profiles of the images in Figures 4.13a and b showing the exact intensity on the detectors further illustrate the effect of plasmon scattering (see Figure 4.13c and d). Two types of linescans are shown. Linescan A only goes through the atomic column maxima while linescan B passes through the atomic column maxima and the nearest neighbor background (black pixels) minima. It is apparent that the inclusion of inelastic scattering increases the

intensity in the atomic column maxima and background minima for both linescan profiles. The image contrast of the modified *Multislice* based on Weber definition, $(I_{atomic} - I_{background})/I_{background}$, is 0.239, slightly higher than the elastic-only image contrast at 0.228. In other words, plasmon scattering induces intensity enhancement in the atomic position which is higher than the enhancement in background (black pixels). This is somewhat counterintuitive since inelastic scattering is thought to reduce image contrast.[134] In bright-field TEM imaging, such contrast reduction was observed albeit for only less than 1 %. Another possible explanation is the assumption that the inelastically scattered electrons retain the same coherence as the elastic ones. The modified *Multislice* algorithm treats the inelastic scattering to retain the phase of the elastic part. If some incoherence is introduced by calculating the phase induced by the plasmon inelastic scattering, contrast reduction could be observed.

4.9 Summary and Future Work

In summary, incorporation of inelastic plasmon scattering into *Multislice* method was done by taking into account the plasmon cross section. The results were analyzed based on broadening in the CBED patterns, EELS spectra, and HAADF-STEM imaging. Surprisingly, a slight enhancement in the image contrast simulated using the modified *Multislice* method was obtained. The calculation time of the modified algorithm scales with the number of energy levels. Optimization of the algorithm to minimize calculation time without loss of accuracy is certainly important. Specifically, the use of larger grid size of2 2048 x 2048 can improve the accuracy but results in impractically long simulation time. With improved algorithms, it is expected that more accurate results can be computed within reasonable time. It is also of interest to incorporate other types of inelastic scattering such as surface plasmon loss and core-loss. One only needs to add the expression for the cross section keeping the structure of the algorithm intact. Hence, a complete picture of elastic and inelastic events can be accounted in the image simulation.

5

Imaging Mn Dopant Atoms inside ZnSe Semiconductor Nanocrystals

Nanometer-scale semiconductors that contain a few intentionally added impurity atoms can provide new opportunities for controlling electronic properties. However, since the physics of these materials depends strongly on the exact arrangement of the impurities, or dopants, inside the structure, and many impurities of interest cannot be observed with currently available imaging techniques, new methods are needed to determine their location. We combine electron energy loss spectroscopy with annular dark-field scanning transmission electron microscopy (ADF-STEM) to image individual Mn impurities inside ZnSe nanocrystals. While Mn is invisible to conventional ADF-STEM in this host, our experiments and detailed simulations show consistent detection of Mn. Thus, a general path is demonstrated for atomic-scale imaging and identification of individual dopants in a variety of semiconductor nanostructures.[135]

5.1 A Survey of Dopant Imaging

Electronic devices have long relied on the intentional incorporation of impurities, or dopants, to control semiconducting materials. As the size of these devices shrink, nanometer-scale volumes of semiconductor can contain only a few impurity atoms,[136] presenting new possibilities for doped nanostructures.[137] For example, solotronic devices now exploit solitary dopants in a semiconductor to obtain new electronic, magnetic, and optical capabilities. However, in doped nanostructures, statistical fluctuations in the number and position of the impurities can have a dramatic effect on the overall behavior.[138] Thus, the ability

to locate the dopants through atomic-scale visualization is often critical for understanding the physics of these materials.

Visualization could also address difficulties in the preparation of doped nanostructures. For example, colloidal quantum dots are chemically-synthesized, nanometer-scale crystals of semiconductor that exhibit optical spectra that can be tuned with size,[139] an effect that is useful for many applications.[140-142] To control the optoelectronic properties of these materials further, researchers have worked to incorporate impurities. These materials also allow solotronic behavior to be studied in extremely small volumes.[143-146] However, while progress has been made in the synthesis of doped nanocrystals,[147, 148] the preparation of many systems remains a major challenge. To test different approaches, it would be extremely helpful if the number and location of the dopants could be observed directly.

Although individual impurities can be visualized on a surface with various methods, including scanning probe microscopy,[149] only a few techniques allow imaging of a single dopant within a semiconductor. Atom-probe tomography creates such images by disassembling a material via field emission and detecting the type and origin of the ejected atoms.[150] However, because the sample must be shaped as a tip to obtain the necessary electric field, this approach is best suited to nanostructures with a high aspect ratio (*e.g.*, nanowires). For nanocrystals, which are roughly spherical in shape, it is more challenging to apply. Another technique, scanning transmission electron microscopy (STEM), has potential to be more broadly applicable, especially with the resolution achievable with aberration-correction.[151-153] A highly focused electron beam is scanned across the sample while scattered electrons are collected with an annular-dark-field (ADF) detector. This allows high-resolution images with atomic-number (Z) contrast to be obtained. Indeed, single dopants within a crystalline semiconductor have been imaged with the ADF-STEM approach.[154-156] An atomic column that contains an impurity appears with

slightly different contrast in the image. However, despite its success, this approach suffers from a fundamental limitation. The dopant must have a large *Z*-contrast with the surrounding semiconductor atoms to ensure its visibility.[124] Alternative methods are still needed for the many cases when this condition is not satisfied, including doped semiconductor nanocrystals.

Here we demonstrate such a technique and visualize individual impurities buried in a semiconductor. For our test system, we utilize Mn-doped ZnSe nanocrystals. In this host, Mn will be invisible to standard ADF-STEM imaging. These nanocrystals have also previously been well characterized.[144] In particular, unlike other impurities, the average local environment of the Mn can be easily determined with electron paramagnetic resonance measurements. These have confirmed that Mn substitutes for Zn on the ZnSe lattice. Thus, we know that Mn atoms are incorporated inside the nanocrystal.

5.2. Methods

5.2.1. Preparation of doped ZnSe nanocrystals

Mn-doped ZnSe nanocrystals were prepared following a previously published procedure.[144] In brief, 15 mL of distilled 1-hexadecylamine was placed in a 50 mL 3-neck flask equipped with a septum, a condenser, and a thermocouple. The hexadecylamine was degassed and dried at 90°C for three hours under alternating nitrogen and vacuum. Meanwhile, dimethylmanganese was prepared in a nitrogen-filled glovebox. 12.5 mg of finely ground $MnCl_2$ was suspended in 0.5 mL of anhydrous tetrahyrdrofuran (THF). 0.2 mL of 3.0 M methylmagnesium chloride in THF was added dropwise, and the suspension turned clear and golden. The dimethylmanganese solution was diluted with 1.8 mL of toluene. Next, 4.0 mL of trioctylphosphine, 0.8 mL of 1.00 M trioctylphosphine selenide, 82 μL of diethylzinc, and a variable amount of dimethylmanganese solution were combined in a 10 mL syringe. The amount of dimethylmanganese added ranged from 0 to 0.6 mL. The syringe was swiftly

injected into the 3-neck flask at 310°C under nitrogen, resulting in a puff of smoke. The particles were grown for 30–90 minutes at 240-280°C while the size was monitored by occasionally withdrawing an aliquot of the reaction mixture, diluting in hexanes, and taking the absorption spectrum. The lowest energy absorption peak could be used to estimate the size.[144] Based on earlier measurements, the intensity of the Mn photoluminescence peak at ~580 nm could be used to estimate the amount of Mn incorporation. More quantitative elemental analysis was also performed, as described below. Once the desired size was obtained, the reaction was cooled to 90°C and an equal volume of 1-butanol was added. The particles were precipitated with methanol, centrifuged, and resuspended in hexanes. Then they were precipitated with ethanol and centrifuged twice, resuspending in hexanes each time.[157] Absorbance and photoluminescence spectra from both the doped and undoped samples were acquired to confirm the absence and presence of Mn in each (Figure 5.1).

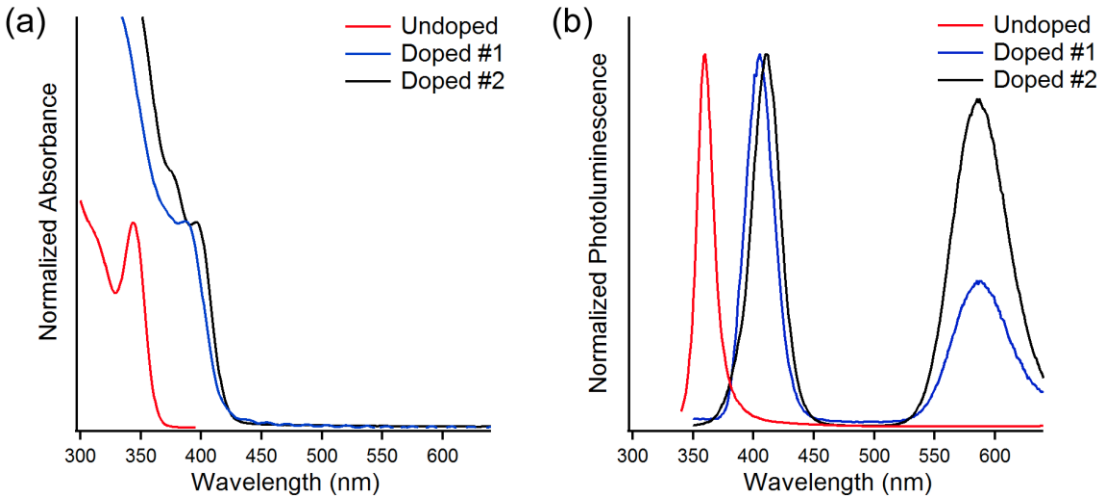

Figure 5.1. Optical properties of ZnSe nanocrystals. (**a**) Absorption and (**b**) photoluminescence data for an undoped and two Mn-doped samples are shown. The spectra labeled "Doped #1" and "Doped #2" are obtained from 2.9-nm-diameter ZnSe nanocrystals with 0.7 ± 0.14 Mn per nanocrystal and 3.7-nm-diameter ZnSe nanocrystals with 6.2 ± 1.5 Mn per nanocrystal, respectively. Spectra labeled "Undoped" are for ~2 nm ZnSe nanocrystals in which no Mn was introduced.

For STEM observations about 5 µl solutions of the as-synthesized ZnSe nanocrystals dispersed in hexane were drop-cast onto standard ultrathin carbon-coated copper TEM grids and left to dry in air. Prior to loading into the STEM column, these samples were subjected to acetone vapor for 5-10 minutes and then heated at 130°C under vacuum for 8 hours to reduce trioctylphosphine oxide surface ligands and other carbon contaminants.

For elemental analysis, only acid-leached plasticware, 18 MΩ deionized water, and trace grade acids were used. Approximately 2-3 mg of particles were dissolved in 2.5 mL of reverse aqua regia (4:1 HCl to HNO_3), then diluted 500-fold with water. Inductively coupled plasma – mass spectrometry (ICP-MS) was carried out on a Thermo Scientific XSeries2 ICP-MS fitted with a hexapole collision/reaction cell. Calibration was achieved by comparing the unknown intensities to a curve prepared by the analysis of 4 multi-element standards purchased from SPEX Industries and diluted accordingly. Elements lighter than mass 39 (potassium) were analyzed at standard mass resolution with no reactive or collision gases used. Elements greater than or equal to mass 39 were analyzed at standard mass resolution using helium/hydrogen collision reaction mode (CCT) with kinetic energy discrimination (KED). Five replicates were used to determine the mean and standard deviation. Sample introduction used an ESI PC3 (Peltier cooler) FAST system with sample loops to reduce oxide formation and carryover between samples. ^{89}Y was added as an internal standard to compensate for matrix effects and instrument signal drift.

5.2.2 STEM-EELS Measurement

All measurements presented in this study were carried out at the Cornell Center of Materials Research using a dedicated aberration-corrected Nion Ultra-STEM. The microscope was equipped with a VG cold-field-emission gun, a Fischione Instruments annular-dark-field (ADF) detector, and a Gatan Enfina-1000 energy loss spectrometer. A STEM probe of 1.2 Å in diameter was achieved

by using an α_{obj} = 30 mrad convergent beam and correcting spherical aberrations of the objective lens up to the 5th order. The STEM was operated with an electron-beam energy of E_0 = 100 keV. It should be noted that aberration coefficients tend to change slightly during the course of the STEM sessions and hence frequent adjustments were made (which result in slightly different sets of coefficients). However, a ~1.2 Å probe was maintained during critical data acquisition. The size of the probe was limited by residual high-order spherical aberrations, chromatic aberrations, and a finite source size.[158-160] The inner angle of the ADF detector for the lens settings used in these experiments was measured to be 91 mrad. The acceptance angle of the EELS spectrometer was estimated to be about 40 mrad. The incident electron-beam current was measured to be 150 - 200 pA and the dwell time at each pixel was 0.2 s. The choice of beam current and dwell time was dictated by limitations due to beam-induced specimen damage. The typical dose of electrons in these experiments was about 50 kC/cm^2. Additional experiments showed that if the beam dose was increased considerably, specimen damage occurred. As in most selenides and sulfides, the electron-beam damage in ZnSe nanocrystals is primarily governed by the "knock-on" process.[161]

Our approach combines aberration-corrected STEM with electron energy loss spectroscopy (EELS) to obtain images based on atom-specific excitations of core-level electrons. The combination of STEM and EELS has previously proven very effective for compositional analysis at the atomic-scale and for measuring local electronic and optical properties of materials.[162] For imaging of buried dopants, it has an additional important advantage. Unlike standard high-resolution ADF-STEM imaging, where the visibility of the dopant is related to the small change in the scattered-electron signal when the beam scans between an atomic column with an impurity and one without, EELS mapping is based on detecting a characteristic core-edge electron-energy-loss signal from the dopant compared to an essentially zero background. Consequently, single-atom

sensitivity with EELS has already been demonstrated.[163, 164] For the specific case of Mn-doped nanocrystals, we measured EELS of the Mn $L_{2,3}$-edge while the STEM probe scans across a nanocrystal. The Mn $L_{2,3}$-edge exhibits an identifiable double-peaked spectrum and is the only EELS feature between 640 and 660 eV in our samples.[165] Thus, atomic columns with (without) a Mn should appear bright (dark) when the EELS signal from this energy range is used for imaging.

To collect the data, we utilized a Nion aberration-corrected Ultra-STEM operated at 100 keV. The microscope was equipped with a cold-field-emission gun, an ADF detector, and a parallel EELS spectrometer. With a 30 mrad convergent beam corrected for spherical aberrations of the objective lens up to 5^{th} order, a STEM probe with a diameter of 1.2 Å was obtained. The incident beam current was measured to be 150-200 pA. Such a high current was necessary to detect the Mn $L_{2,3}$-edge while scanning the probe.[166] From separate measurements, we confirmed that this current was below the sample damage threshold.

5.3 EELS Core-Level Imaging

Three ZnSe samples were examined: (i) 3.7-nm-diameter nanocrystals with 0.58 at.% incorporated Mn (an average of 6.2 ± 1.5 Mn per nanocrystal), (ii) 2.9-nm nanocrystals with 0.13 at.% Mn (0.7 ± 0.14 Mn per nanocrystal), and (iii) a reference sample of ~2-nm undoped nanocrystals. For imaging experiments, nanocrystals were drop-cast from dispersions onto copper microscopy grids coated with thin amorphous carbon. Before loading each specimen into the STEM, it was exposed to acetone vapor and then heated under vacuum at 130°C to remove ligands from the nanocrystal surface.

Figure 5.2 shows a typical high-resolution ADF-STEM image for low-doped ZnSe:Mn nanocrystals. Atomic columns within individual nanocrystals can be clearly seen. From such an image, we then selected one of the nanocrystals and simultaneously collected an ADF-STEM image and an EELS

map. For this, the STEM probe was scanned across the nanocrystal with ~2.5 Å steps and a 0.2 s dwell time. To reduce the possibility of sample damage, the probe was moved during the dwell in 16 x 16 steps within each 2.5 x 2.5 Å^2 pixel. After the full scan, each pixel in the raw EELS map contains an energy loss spectrum in the energy range sensitive to Mn.

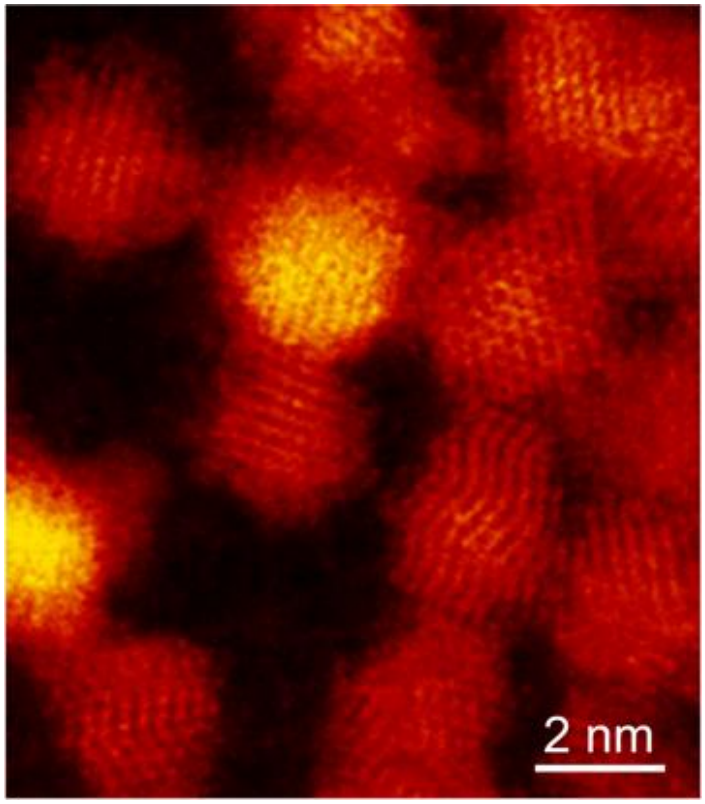

Figure 5.2. Low magnification ADF-STEM images of singly doped ZnSe:Mn nanocrystals obtained using Nion aberration-corrected microscope.

As one might expect, the raw experimental data acquired using our EELS-imaging technique contain considerable noise (statistical and instrumental). Consequently, for the quantitative interpretation of the Mn $L_{2,3}$-edge spectra, further signal processing was employed. We first applied a standard background subtraction using the function $g(E) = B \times E^{-R}$.[165] Then, the high frequency noise was removed from each Mn $L_{2,3}$-edge EELS spectrum using a Fourier-transform-

based low-pass Gaussian filter. This eliminated frequencies above 0.8 eV^{-1}. Figure 5.3a shows an example of an EELS spectrum of the Mn $L_{2,3}$-edge before and after low-pass filtering.

To identify which of the spectra in the recorded EELS data represents detection of Mn, a least-squares-fitting algorithm[167] was then applied. The function $f(E) = S \times EELS_{ref}(E)$ was used, where $EELS_{ref}(E)$ is a reference Mn $L_{2,3}$-edge spectrum obtained from a bulk crystalline PtMn sample using the same microscope and similar conditions, and S is a scaling factor that the fitting algorithm varies to obtain a best fit of the experimental EELS spectrum. In other words, the fitting algorithm compares $f(E) = S \times EELS_{ref}(E)$ with the experimental spectrum. Consequently, for each position of the probe on the sample, this fitting process produces two parameters: the scaling factor S, which is related to how intense the experimental data is in the spectral region that contains the double-peaked Mn $L_{2,3}$-edge, and a "goodness-of-fit" parameter, G. For G, we used the inverse of the reduced chi-squared value[167] that was obtained from the fitting algorithm. Figures 5.3b-d show three examples of filtered EELS spectra and the corresponding best fit obtained with the least-squares algorithm. The values of S and G are also shown for each. S is given in terms of $|S|_{mean}$, the averaged absolute value of the scaling factor, which we used as an indicator of the noise level.

To obtain a two-dimensional map for location of the Mn, we then employed the function $M(i,j) = G(i,j) \cdot S(i,j)$, where i and j are integers that label the pixels. For the successful detection of Mn, we required that $S(i,j) > 2.5 \cdot |S|_{mean}$ and $G(i,j) > G_0$, where G_0 is a critical value for the goodness-of-fit. Typical histograms for S and G obtained from a scan over a Mn-doped nanocrystal are shown in Figure 5.3e and f. By analyzing similar histrograms for undoped particles, we set G_0 to 0.0155. In data from undoped nanocrystals, a value of G_0 larger than this value was not observed. The values of $|S|_{mean}$ were evaluated for each data set separately based on the particular histogram.

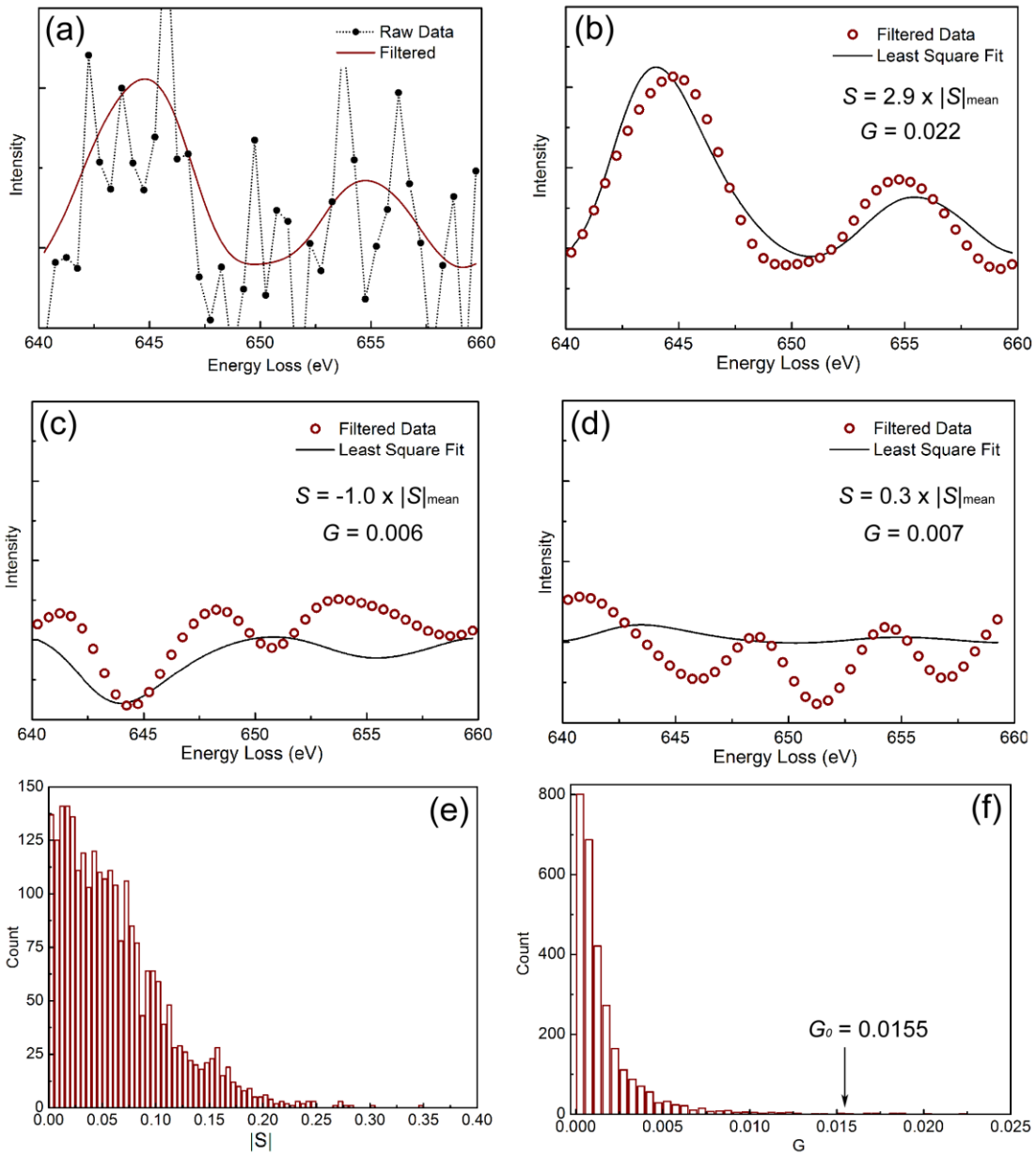

Figure 5.3. Examples of the different steps in the data analysis. (**A**) The EELS spectrum of the Mn $L_{2,3}$-edge (background subtracted) after a Fourier-transform-based low-pass Gaussian filter was applied. (**B**) The result of our least-squares fitting algorithm on the spectrum shown in (A). The extracted values of S and G are indicated in the inset. Our analysis concluded that this pixel contained a Mn impurity. (**C** and **D**) Two other examples of filtered EELS data and the corresponding fit, presented as in (B). Our analysis concluded that these pixels did not contain Mn. (**E** and **F**) Typical histograms of the values $|S|$ and G obtained from the map of a single nanocrystal.

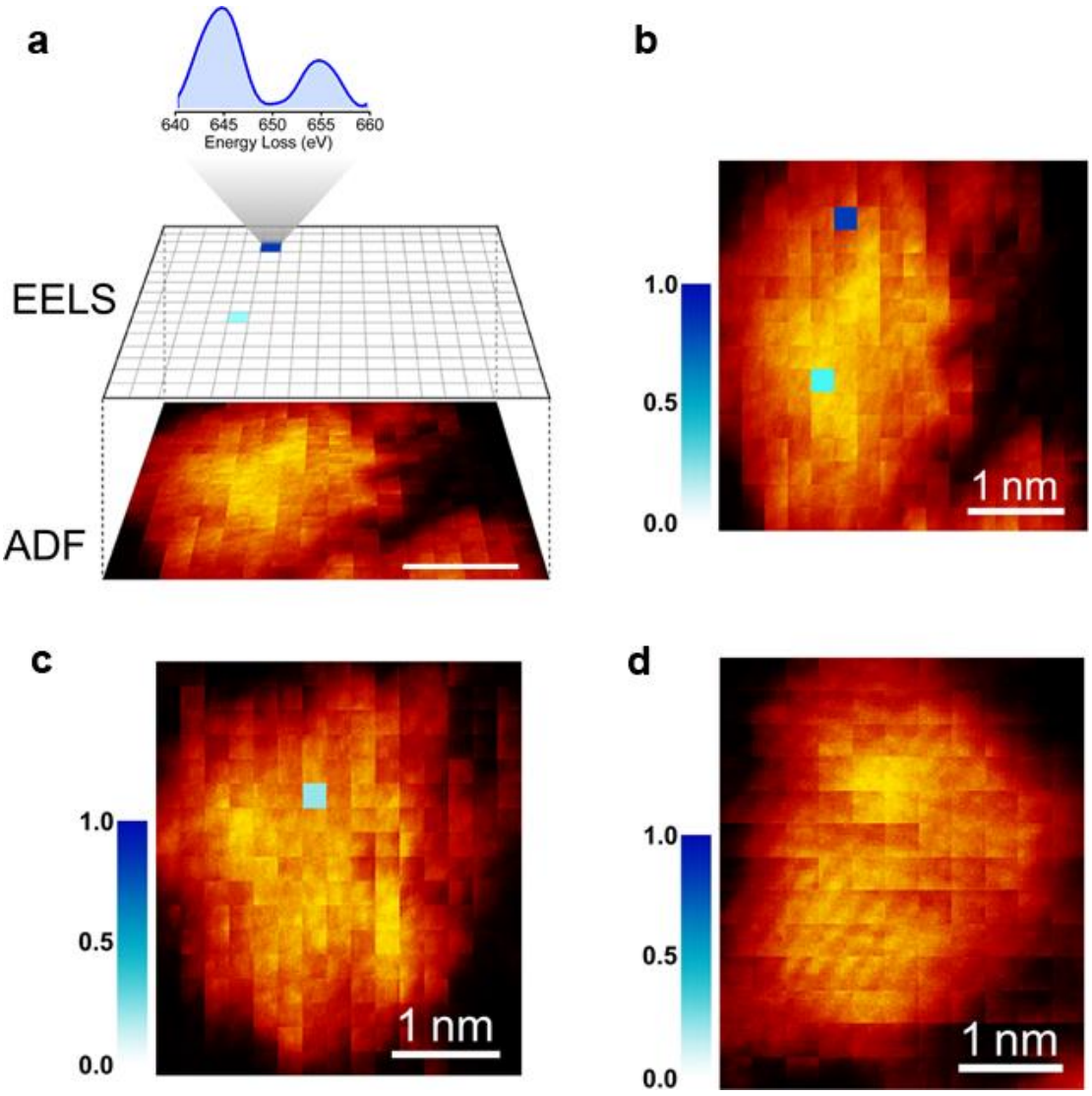

Figure 5.4. (a) The extracted core-level EELS map for the Mn $L_{2,3}$-edge along with the corresponding ADF-STEM image of a Mn-doped ZnSe nanocrystal (Sample 2). The energy loss spectrum for one of the pixels where Mn was detected is shown. The characteristic double-peaked EELS spectrum for the Mn $L_{2,3}$-edge is seen. (b) Overlap of the Mn $L_{2,3}$edge intensity map and the ADF-STEM image, both shown in (b). The atomic-resolution in the ADF-STEM image is lost in this scanning mode. (c) EELS Mn $L_{2,3}$-edge intensity map overlapped with the ADF-STEM image from a different Mn-doped ZnSe nanocrystal (Sample 2). (d) An example of the EELS Mn $L_{2,3}$-edge intensity map overlapped with the ADF-STEM image from an undoped ZnSe nanocrystal (Sample 3) showing no Mn EELS signals, as expected.

Figure 5.4a shows an example of the final $M(i,j)$. It represents the resolved intensity map for the Mn $L_{2,3}$-edge and can be used to locate the dopants in the nanocrystal when overlapped with the ADF-STEM image (Figure 5.4b). If we compare EELS spectra for different spots (Figure 5.5), only the bright pixel in $M(i,j)$ exhibits the double-peaked shape seen in the reference. This indicates that the core-loss imaging is localized within the atomic position of the dopant atoms for the pixel size used in this experiment. When the same detailed analysis was repeated on 10 individual doped nanocrystals, similar results were observed (*e.g.*, see Figure 5.5a). However, we did not detect any Mn in undoped nanocrystals (Figure 5.5b), as expected.

5.4 Comparison with Simulations

We also compared these experimental results with simulations.[168] We utilized the *Multislice* code[91] to describe the electron-beam propagation through the material. *Multislice* uses the frozen-phonon approximation to model the atomic thermal vibrations.[169] The STEM probe was generated using the following parameters for the electron optics: electron beam energy of E_0 = 100 keV, objective aperture of α_{obj} = 30 mrad, defocus of Δf = 52 Å, and spherical aberration coefficients of $C_{3(s)}$ = 0.0167 mm and C_5 = 0.0 mm. These specific values were obtained from the experimental measurements. Additional beam broadening due to the finite size of the source and chromatic aberrations were also included. The final simulated probe with 1.2 Å full-width-at-half-maximum (FWHM) is shown in Figure 5.6. As can be seen, the majority of the probe intensity is located in the middle and the probe has minor tails indicating the capability to perform atomic-resolution STEM imaging. We then combined this with a simple quantum-mechanical description of the core-level electronic transitions of Mn. Thus, both the ADF-STEM images and EELS map could be simulated. More detailed descriptions on the cross section of the core-level excitations in EELS can be found in Section 3.5.

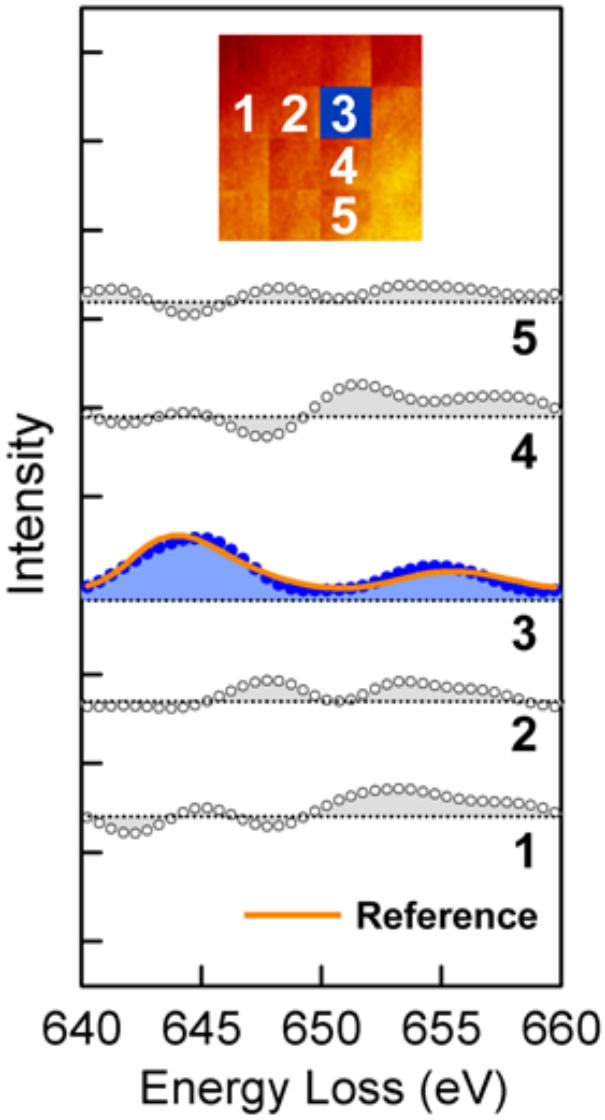

Figure 5.5. Measured EELS Mn $L_{2,3}$-edge from five pixels from the map shown in (c). A low-pass filter was applied to the EELS spectra to remove instrumental noise. A reference EELS Mn $L_{2,3}$-edge is also shown (orange curve).

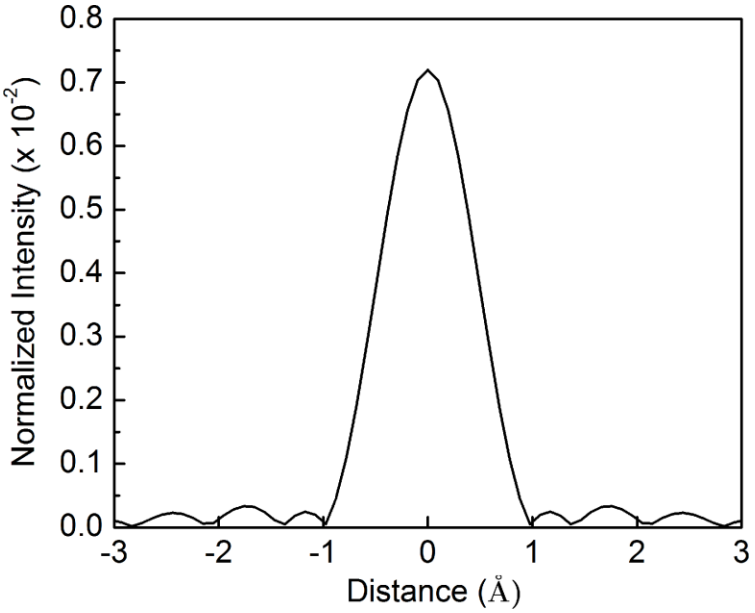

Figure 5.6. The aberration-corrected STEM probe simulated with *Multislice.* The spot size has a full-width-at-half-maximum (FWHM) of about 1.2 Å. The probe was generated for E_0 = 100 keV and α_{obj} = 30 mrad. Spherical aberrations, chomatic aberrations, and the source size were also included.

Figure 5.7 summarizes the results. A faceted 4-nm ZnSe nanocrystal with the zinc-blende crystal structure was first constructed (Figure 5.7a and b). High-resolution ADF-STEM images of this nanocrystal were then generated with the model. The result for an undoped nanocrystal viewed along the [111] crystallographic direction is shown in Figure 5.7c. The same nanocrystal with two Mn atoms, located 1 and 3 nm below the top surface (or beam entry surface) of the nanocrystal, appears in Figure 5.7d. Since the *Z*-contrast between the dopant (Z_{Mn} = 25) and the host atoms (Z_{Zn} = 30) is small, the Mn atoms are not visible in the simulated ADF-STEM images, as summarized in Figure 5.8. Note this occurs even in this simulation where the statistical and instrumental noise that would be present in a real experiment is absent.

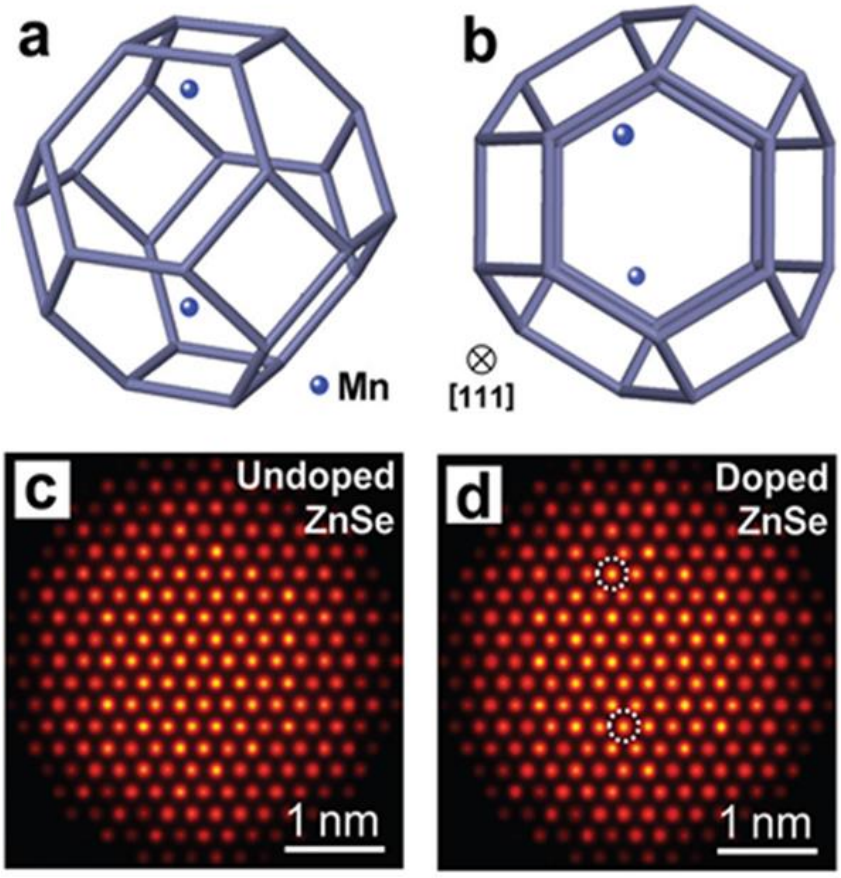

Figure 5.7. (a) Outline of a faceted 4 nm ZnSe nanocrystal with two Mn dopants inside. (b) The structure in (a) viewed along the [111] crystallographic direction. The upper dopant is 1.3 nm below the top surface of the nanocrystal and the lower one is 2.9 nm below. (c) Simulated high-resolution ADF-STEM image of a 4 nm undoped ZnSe nanocrystal viewed along the [111] crystallographic direction. (d) Simulated high-resolution ADF-STEM image of a 4 nm ZnSe nanocrystal with two Mn dopants as in (b). The circles indicate the atomic columns where the Mn are located. Even without the presence of noise in the simulation, the contrast is insufficient to observe the Mn.

To test whether conventional ADF-STEM imaging could resolve the location of Mn dopants, we calculated the visibility, $V = \left(I_H - I_D\right)/I_H \times 100\%$, of Mn atoms at various depths in [111]-, [100]-, and [110]-oriented 4-nm ZnSe nanocrystals. Here, I_D is the intensity of a doped column and I_H is the intensity of an undoped (*i.e.* host) column in the ADF image. The results are summarized in Figure 5.8. Even the highest visibility obtained (12 %), which is along the [111] direction, still falls below what would be necessary (~20 %) to locate the dopant unambiguously in an actual experiment. Therefore, these simulations are consistent with our experiments, where Mn dopants were invisible to the ADF-STEM imaging approach.

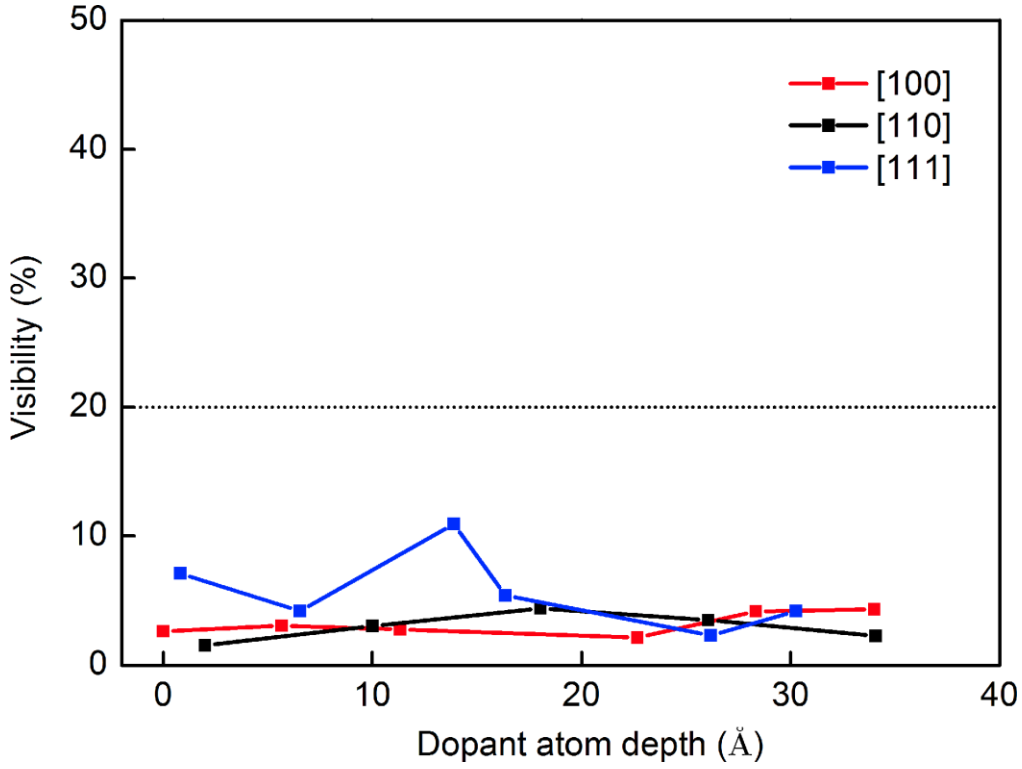

Figure 5.8. The simulated visibility of a Mn dopant in a 4-nm ZnSe nanocrystal in an ADF-STEM image as a function of the depth of the dopant from the top surface of the nanocrystal. The nanocrystal is imaged along the [100], [110], or [111] crystallographic direction. The dotted line at 20 % represents the visibility that is required for detection of Mn in an actual experiment.

To estimate the expected EELS signal for the Mn, the local beam intensity must be multiplied by the probability that a relevant electronic transition in Mn will occur. Electrons are excited from an initial core-level state, $|i\rangle = |2p_{1/2}\rangle$ or $|2p_{3/2}\rangle$, to a final state, $|f\rangle$, which is near or above the Fermi level. The transition probabilities are described by Fermi's golden rule and given by the transition matrix element *T* as:[170]

$$T^2 = \left|\langle f|\exp\left(i\,\vec{q}\times\vec{r}\right)|2p_{1/2} \text{ or } 2p_{3/2}\rangle\right|^2,$$

where $\vec{q}$ is the momentum transfer and $\vec{r}$ is the position vector. Because the 2*p* core-levels of Mn are highly localized [with a radius, r_{2p}, of 0.21 Å[171]], Equation 5.1 implies that the EELS signal will originate from a very small volume. The Mn EELS map can be simulated according to $M_{sim}(i,j) = C \cdot I_{2p}(i,j)$, where $I_{2p}(i,j)$ is the intensity of the incident beam that passes through the spherical volume around Mn with $r < r_{2p}$, and *C* is a constant that includes T^2 and all of the experimental parameters related to the microscope.[168]

To produce theoretical EELS maps, we simulated scans of the STEM probe across individual 4-nm Mn-doped ZnSe nanocrystals. For example, for a [111]-oriented nanocrystal we used 1.2 Å steps in the *x*-direction and 2 Å steps in the *y*-direction. These step sizes were dictated by the symmetry of the crystal. Using *Multislice* a three-dimensional matrix containing the calculated beam intensities as a function of the *x*-, *y*-, and *z*-position inside the nanocrystal was obtained. Room-temperature 10-phonon configurations were used for these calculations.

From these data, we then calculated the expected intensity of the Mn $L_{2,3}$-edge EELS signal at each position of the probe using:

$$M_{sim}(i,j) = C \times I_{2p}(i,j).$$

C is a constant that includes characteristics of the STEM probe, geometrical parameters related to the microscope, and the cross-section for excitation of the Mn $L_{2,3}$-edge. $I_{2p}(i,j)$ is the portion of the incident electron beam that has a finite probability of exciting an electron from the 2p orbitals of Mn at site i, j. $I_{2p}(i,j)$ was obtained by integrating the intensity of the beam that fell within a spherical volume centered at the i, j lattice site with radius r_{2p} = 0.21 Å. The beam must fall within this volume to have overlap with the initial *2p* state of the Mn and excite the electron. This procedure was then repeated for all possible Mn sites to obtain the complete $I_{2p}(i,j)$. Since $M_{sim}(i,j)$ and $I_{2p}(i,j)$ are directly proportional according to Eq. S1, the normalized map of $I_{2p}(i,j)$ can be treated as a normalized map of $M_{sim}(i,j)$. We used this approach to obtain the simulated Mn EELS maps. Note that in the final map, we lowered the resolution to a square grid with 2.5 Å pixels to compare with the experimental results.

Because the experimental maps exhibited Mn signals that were restricted to a single pixel, we also performed calculations to determine if this was consistent with theoretical expectations. In other words, we assessed how localized the EELS signal of the Mn $L_{2,3}$-edge should be. We again calculated the integrated intensity of the probe within the spherical volume with radius r_p = 0.21 Å centered at the Mn. However, we then plotted this value as a function of the incident probe position relative to the atomic column containing the Mn. The results are presented in Figure 5.9. When the probe is located more than 1 Å away from the Mn-containing column, no detectable Mn $L_{2,3}$-edge EELS signal is expected. This result explains why the core-level EELS map measured with 2.5 Å steps produces isolated individual pixels.

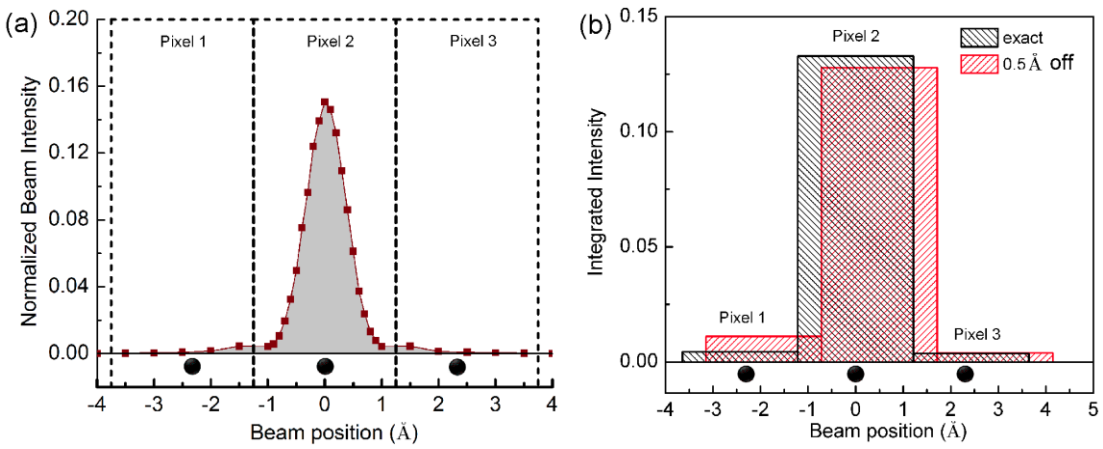

Figure 5.9. The localization of the Mn signal in the EELS map. (**A**) Integrated intensity of the probe within the spherical volume with radius r_{2p} = 0.21 Å centered at the Mn as a function of the incident probe position. The atomic column with the Mn is located at position 0. The Mn atom is 13 Å below the top (beam entry) surface of the nanocrystal. The positions of the neighboring atomic columns are indicated with the solid black circles along the *x*-axis. (**B**) The integrated intensity within each pixel calculated from (A). Two cases are shown: (i) where the pixel is centered over the atomic column containing the Mn, and (ii) where the pixel is shifted by 0.5 Å.

Our *Multislice* simulations also show that the intensity of the electron beam depends on the crystal orientation. In Fig. 5.10a, the electron beam is first focused on the top surface of the nanocrystal. The beam intensity is then plotted as it propagates through the ZnSe crystal for three main crystallographic orientations, [100], [110], and [111]. The results indicate that the EELS signal from the Mn should be stronger if the nanocrystal is oriented along the [111] direction. The arrangement of the atoms for this direction is beneficial for beam propagation.[168] In addition, for the [111] direction, the intensity is maximized at a depth of ~10 Å. Thus, the technique is more sensitive to dopants buried than at the surface. This is particularly relevant for doped nanocrystals, where methods are needed to distinguish the impurities that are actually incorporated in the semiconductor from those that are simply decorating the surface.[148]

The final simulated EELS map for the 4-nm, [111]-oriented ZnSe nanocrystal with two dopant atoms (as depicted in Figure 5.7b) is shown in Figure 5.10b. The EELS map is overlaid with the simulated ADF-STEM image from Figure 5.7d, but with the resolution reduced to match the conditions in Figure 5.4b. The simulation confirms the detectability of the Mn with the STEM-EELS approach and reproduces the experimental results. In particular, a detailed analysis [168] indicates that when the incident STEM probe is located more than 1 Å from the center of the atomic column containing the dopant in the ZnSe nanocrystal, the portion of the beam that overlaps the *2p* core-levels is practically negligible (Figure 5.9). This explains why, even without experimental noise, the EELS maps show only one pixel per Mn.

Finally, we used our model to estimate the detection probability. Since the dopant can be located at many different lattice sites inside the nanocrystal, the frequency of detection could be analyzed statistically. Using binomial statistics, the probability of finding a nanocrystal with at least one detected dopant can be expressed as $P = 1 - (1 - p_s)^N$, where p_s is the probability of detecting the dopant and *N* is the average number of dopants per nanocrystal. It should be noted that since the beam propagation is different along different crystallographic directions, the probability p_s also varies with direction. Figure 5.10c shows the estimated probability *P* including uncertainties in the estimation of p_s and the corresponding weights of all possible crystallographic directions.[168] The results are in good agreement with our experimental observations for the two doped samples.

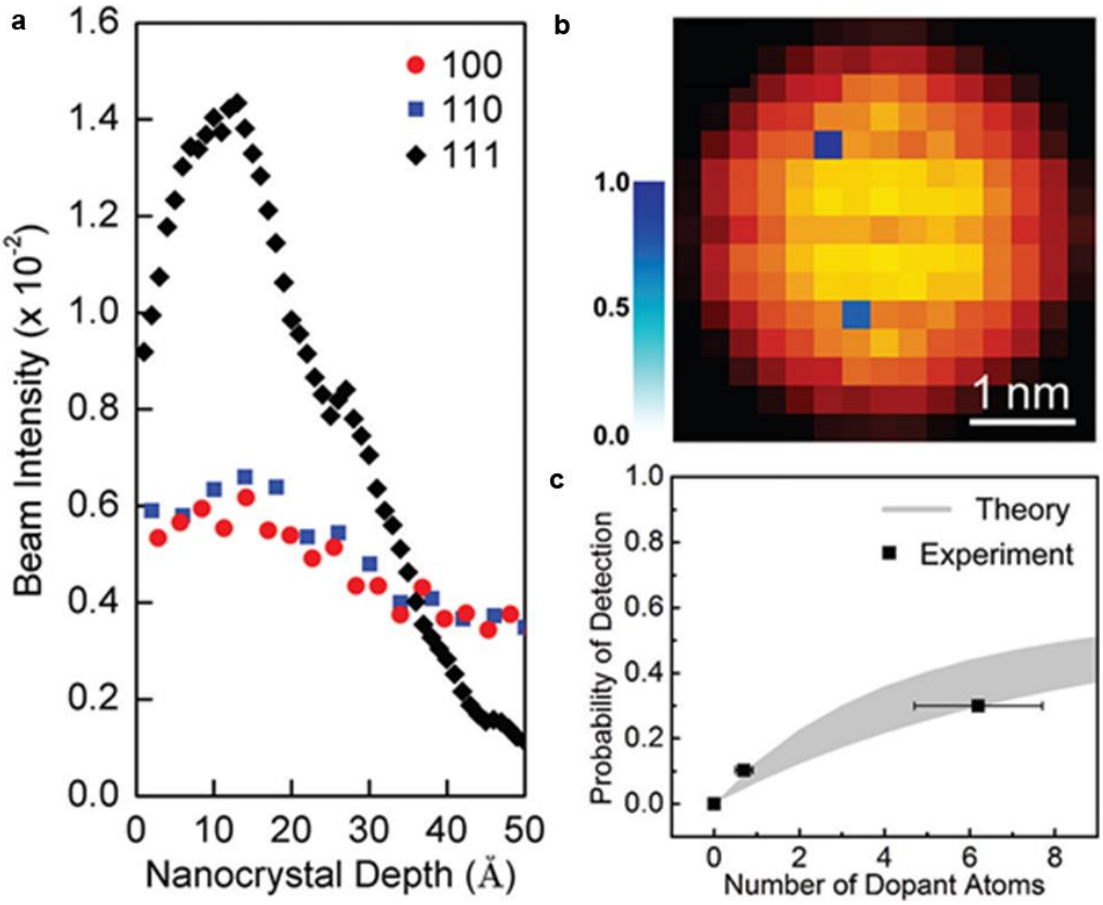

Figure 5.10. (a) Calculated STEM electron beam intensity at the atomic column as the beam propagates along the [100], [110], and [111] crystallographic directions. (b) Overlap of the simulated normalized Mn $L_{2,3}$-edge intensity map with the ADF-STEM image under the experimental conditions used in Figure 5.6. (c) Calculated probability of finding a nanocrystal with at least one detected Mn dopant in the ZnSe nanocrystal using core-level EELS under the experimental conditions. Experimental measurements (Samples 1 and 2) are shown for comparison.

5.5 Summary and Future Work

These results indicate that STEM-EELS present an alternative to conventional techniques for imaging dopants in semiconductors. The sensitivity of this new approach can be improved even further if the dopants have higher cross-sections for core-level excitations or if the electron dose of the scanning probe can be increased without inducing sample damage. In addition to revealing the location of previously invisible dopants, which can aid in the fabrication and characterization of doped nanostructures, this technique can potentially provide new opportunities, such as the study of dopant dynamics due to diffusion.

Since in these samples the Mn atoms are known to be inside the nanocrystals and not simply on their surfaces, These results indicate that STEM-EELS presents a technique for imaging individual dopants in semiconductor nanostructures. It should be broadly applicable to the many impurities that have a suitable EELS edge, typically those with an energy less than 1 keV. This includes elements from Li (Z_{Li} = 2) to Cu (Z_{Cu} = 29) with strong EELS signals for the K- or $L_{2,3}$-edges, elements from Kr (Z_{Kr} = 36) to Ru (Z_{Ru} = 44) with a strong $M_{4,5}$-edge between 80 and 300 eV, and elements from Cs (Z_{Cs} = 55) to Yb (Z_{Yb} = 70) with strong $M_{4,5}$- or $N_{4,5}$-edges. The sensitivity of the approach can be improved even further for dopants that have a higher cross-section for core-level excitations or if the host semiconductor can sustain a higher electron dose from the scanning probe without damage. This suggests that the use of an aberration-corrected STEM with a high-brightness gun and low beam-accelerating voltage will be preferable. In addition to revealing the location of previously invisible dopants, which can aid in the fabrication and characterization of doped nanostructures, this technique can potentially allow other studies, such as the analysis of dopant diffusion.

6

Plasmonic Interactions through Conjugated Bonds of Ligands on PbSe Nanocrystals

The focus of this chapter is on the geometric understanding of the ligand orientation using HAADF-STEM imaging and the surface plasmon interaction supported in the modified chemical bonds of the ligands. When functional films are cast from colloidal dispersions of semiconductor nanocrystals, the length and structure of the ligands capping their surfaces determine the electronic coupling between the nanocrystals. Long chain oleic acid ligands on the surface of IV-VI semiconductor nanocrystals such as PbSe are typically considered to be insulating. Consequently, these ligands are either removed or replaced with short ones to bring the nanocrystals closer to each other for increased electronic coupling. Herein, using high-angle annular dark-field scanning transmission electron microscopy imaging combined with electron energy loss spectroscopy, we show that partial oxidation of PbSe nanocrystals forms conjugated double bonds within the oleic ligands, which then facilitates enhanced plasmonic interaction amongst the nanocrystals. The changes in the geometric configurations of the ligands are imaged directly and correlated with the changes in the surface plasmon intensities as they oxidize and undergo structural modifications.

6.1 Surface Ligands on PbSe Nanocrystals

Colloidal semiconductor nanocrystals are the building blocks for a variety of optoelectronic devices including photodetectors,[172] light emitting diodes,[173] sensors[174] and solar cells.[97] Commonly used synthesis methods produce nanocrystals with surfaces capped with organic ligands. These ligands stabilize

the colloidal dispersions of the nanocrystals and often electronically passivate the defects on their surfaces.[175] The ligands are particularly important when the nanocrystal size is so small that their surface–to-volume ratio is large and electrons and holes are quantum confined within the periodic atomic lattice of the semiconductor.[176] Consequently, the ligands on semiconductor nanocrystal surfaces play a critical role in determining their individual, as well as collective, electronic and optical properties. A technologically important example is lead salt (e.g., PbSe and PbS) nanocrystals, which have been used widely in quantum dot solar cells and infrared detectors.[97, 172-174] Films cast from dispersions of as-synthesized PbSe nanocrystals are insulating because the nanocrystals are capped with long oleate ligands that form a shell around the nanocrystals and keep them too far apart from each other for facile charge transport. The oleate ligands are often removed with hydrazine,[177] or replaced with shorter ligands such as ethanedithiol[178] or pyridine[179] to decrease the distance between the nanocrystals and to improve electronic coupling between the neighboring nanocrystals.[122] This ligand-exchange approach results in enhanced electrical conduction in thin nanocrystal films[180] without loss of quantum confinement and enables novel solar cells that produce multiple electron-hole pairs per absorbed photon.[97] The latter is attributed to multiple exciton generation (MEG) and leads to greater than 100% external quantum yields in solar cells.[181] Interestingly, although simple description of the MEG suggests that the process should be independent of the choice of ligands,[182] there is significant evidence that nanocrystal-ligand interactions and ligand-mediated inter-nanocrystal electronic coupling affect the MEG efficiency,[183] with most reports demonstrating high MEG efficiency in PbSe nanocrystals when short ligands are used.[97, 184]

The importance of the ligands attached to PbSe nanocrystals has motivated various studies of their structural properties. A variety of different techniques such as photoluminescence (PL), nuclear magnetic resonance (NMR), and

molecular dynamics simulations were used to understand the bonding, stability, and geometric arrangements of these ligands on the PbSe nanocrystal surfaces.[185-188] However, direct imaging of the ligands has not been reported. Transmission electron microscopy (TEM) operated in scanning mode (STEM) with ~ 1-2 Å electron probe is capable of such molecular scale imaging. Moreover, STEM equipped with an electron energy loss spectrometer (EELS) can be used to simultaneously image and probe the electronic coupling between nanocrystals when this coupling manifests itself as changes in the localized surface plasmon resonance (LSPR) within the nanocrystals. Such STEM-EELS studies have been reported for ligand-free Au and Ag metallic nanocrystals where high free electron densities allow probing of LSPR modes.[189, 190]

Herein, we show direct imaging of oleic acid ligands attached to the surface of semiconductor PbSe nanocrystals and observe chemical reactions within the ligands that lead to enhanced coupling between the nanocrystals. Specifically, the oleic acid ligands undergo oxidative dehydrogenation initiated by oxide layers on the nanocrystal surfaces. Surprisingly, this chemical reaction leads to enhanced coupling between the nanocrystals and facilitates surface plasmon interactions. Comparisons of oleic-acid-capped oxidized PbSe nanocrystals with hydrazine-treated nanocrystals verify this conclusion.

6.2. Sample Preparation

6.2.1. Synthesis of Colloidal PbSe Nanocrystals

PbSe nanocrystal synthesis was based on the protocol developed by Murphy, et al.[175] and Luther, et al.[178] In a typical synthesis, PbO (2.5 g), oleic acid (9 mL), and 1-octadecene (35 mL) were degassed three times on a Schlenk line at 40 °C and 15 mTorr, while stirring. The solution was then heated to 185 °C under N_2. A 1.00 M solution of selenium in trioctylphosphine (21 mL) and diphenylphospine (0.3 mL), which was prepared inside an N_2-filled glovebox, was then swiftly injected. The solution turned black immediately. The

temperature of the solution was maintained at 140-150 °C for 1 minute. Then, 15 mL of ice-cold anhydrous octane was injected and the heat source was quickly replaced with an ice bath. The reaction mixture was extracted via cannula to a degassed Schlenk flask, which was then brought into the N_2-filled glovebox. The reaction mixture was then precipitated using anhydrous 200-proof ethanol via centrifuge and redispersed in anhydrous hexane, three times. The resulting particles were dispersed in hexane and stored in the glovebox. The size of the particles was determined from optical absorption of the colloidal dispersion using a published calibration curve in Moreels, et al.[191]

6.2.2. Optical Properties of PbSe Nanocrystals

The optical absorbance spectrum collected from the as-synthesized PbSe nanocrystals dispersed in hexane is shown in Figure 6.1. The absorbance was measured using a Varian Cary 5E UV-Vis spectrophotometer. The exciton peak detected at 1720 nm (0.72 eV) corresponds to PbSe nanocrystals with 6 nm diameter, determined using the empirical fit described by Moreels et al.[191] The FWHM of the peak is 50 meV, which translates to approximately ± 0.2 nm size dispersion.

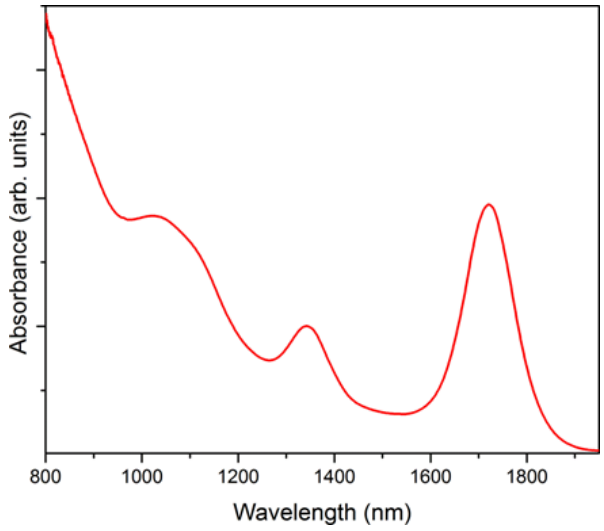

Figure 6.1. Optical absorption spectrum from as-synthesized 6 nm diameter PbSe nanocrystals dispersed in hexane.

6.2.3 Amorphous Si Substrates

The TEM grids used for annular dark-field scanning transmission electron microscopy (ADF-STEM) imaging and electron energy-loss spectroscopy (EELS) analysis were purchased from SIMPore, Inc. Grids with sputter deposited ~ 5 nm amorphous Si (a:Si) film on crystalline Si (c:Si) substrate with 50 nm windows were chosen (Figure 6.2). These grids are particularly suitable for obtaining carbon K-edge EELS signal, as there is no background from the typical amorphous carbon based TEM grids. However, these grids are not suitable for recording oxygen K-edge EELS signal, since some native oxide is present on the a:Si films.

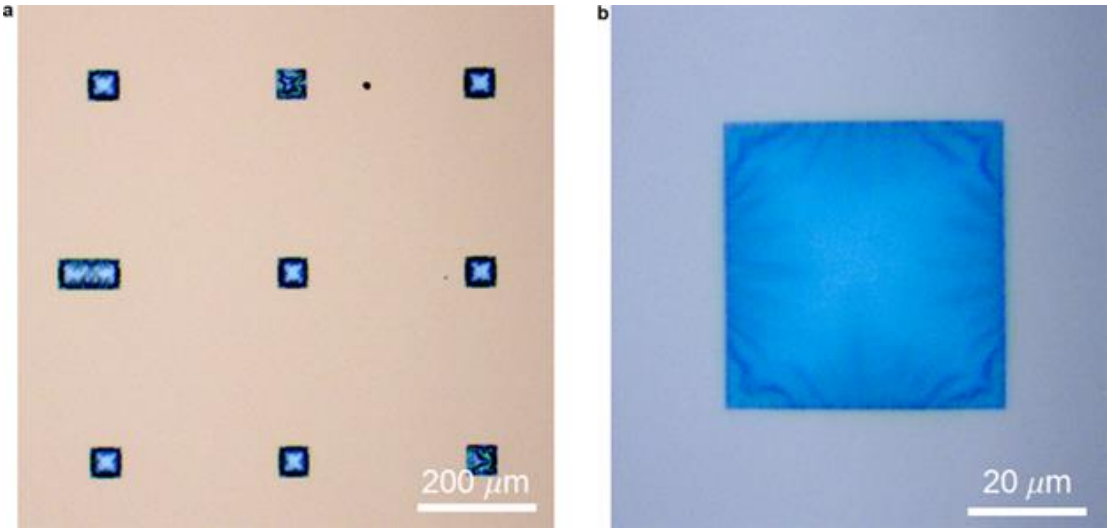

Figure 6.2. (a) Top-view optical micrograph of TEM grids used in these experiments with a:Si substrate. (b) A higher magnification image of one of the windows in (a) showing a:Si substrate in blue. The grids were purchased from SIMPore, Inc.

6.2.4 Preparation of Nanocrystal Films on TEM Grids

The as-synthesized PbSe nanocrystals were dispersed into hexane solution with 10 mg/mL concentration and dropcast onto TEM grids inside a

glovebox. Non-porous amorphous Si from SIMPore, Inc. was used as the substrate for obtaining the images of oleic acid ligands and measuring LSPR and carbon K-edge signals. The substrates consist of nine windows of etched 3.5-5 nm thick a:Si sputter deposited on 100 μm frames. Ultrathin amorphous carbon (< 5 nm) from Ted Pella, Inc. was used for acquiring bulk plasmon loss of the nanocrystal films since the bulk plasmon loss of the a:Si substrate at 17 eV, close to the bulk plasmon loss of PbSe.

6.2.5 Oxidation of Nanocrystals

The data from the as-synthesized samples were obtained from the freshly dropcast samples on TEM grids inside a glovebox that were transferred into TEM column without being exposed to air for more than 10 seconds. After collecting images and EELS data in TEM, these as-synthesized samples on TEM grids were stored in a low-humidity desiccator (24 % RH). The samples were then re-examined with TEM at 5-day intervals. The signals from the partially oxidized samples were obtained after the third/fourth week. Samples typically become completely oxidized after two months.

6.3 Ligand Imaging

High-angle annular dark field-STEM (HAADF-STEM) images and EELS spectra were acquired using FEI Tecnai G2 F30 S-TEM operated at 200 kV accelerating voltage and 60-300 mrad HAADF detector geometry. STEM is equipped with Gatan Enfina-1000 spectrometer with 30 mrad collection angle. HAADF-STEM imaging of oleic acid ligands requires suitable substrates. Thin a:Si substrate with 3.5 – 5 nm thickness, which is thinner than the available ultrathin amorphous carbon substrates, appears to be suitable for imaging the ligands. STEM operated at 200 kV accelerating voltage was chosen to produce the optimal spatial resolution with minimal beam damage.

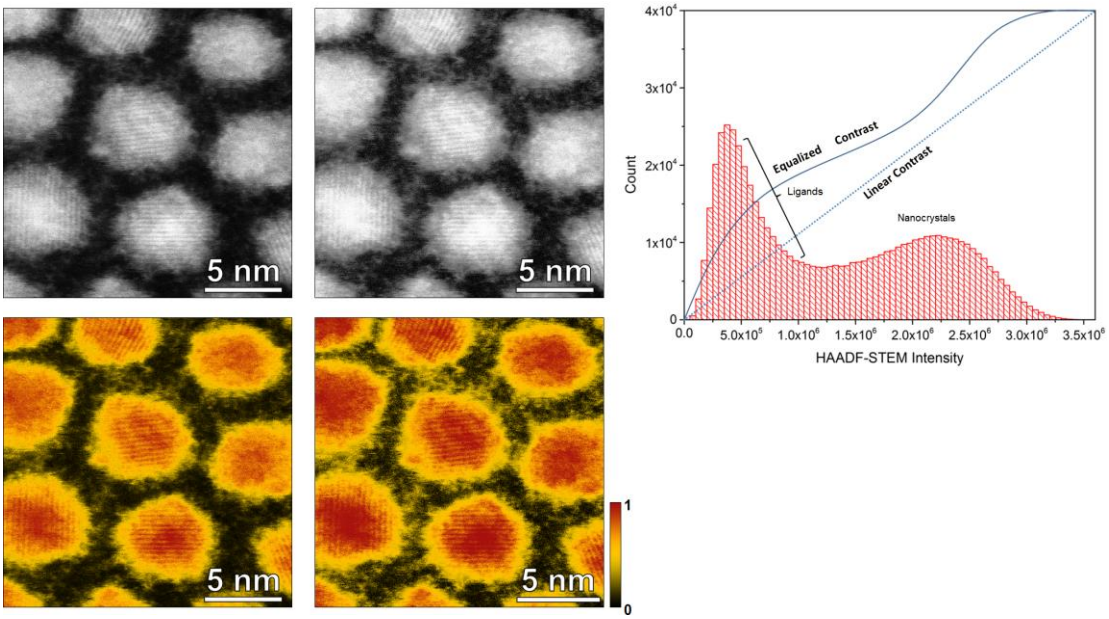

Figure 6.3. Raw HAADF-STEM image of the as-synthesized PbSe nanocrystals: (a) in grayscale and (b) in color. (c,d) The same images as in (a) and (b) after applying a contrast equalization algorithm. Improvement in visibility of ligands can be seen. (e) Histogram of intensities in image in (a) with linear and applied non-linearly equalizing contrast lines.

HAADF-STEM images of PbSe nanocrystals with ligands were processed to improve the visibility of the surface ligands. The raw image of the as-synthesized PbSe nanocrystals in grayscale is shown 6.3a. In these typical raw images, the contrast is linear. Under these conditions, the surface ligands are already visible. However, the visibility of the ligands can be enhanced by applying a contrast equalization algorithm, which is available in *Digital Micrograph* software (Gatan, Inc.). The image of the as-synthesized PbSe nanocrystals shown in Figure 6.3a is shown in Figure 6.3c after contrast equalization. The algorithm improves the visibility of the surface ligands.

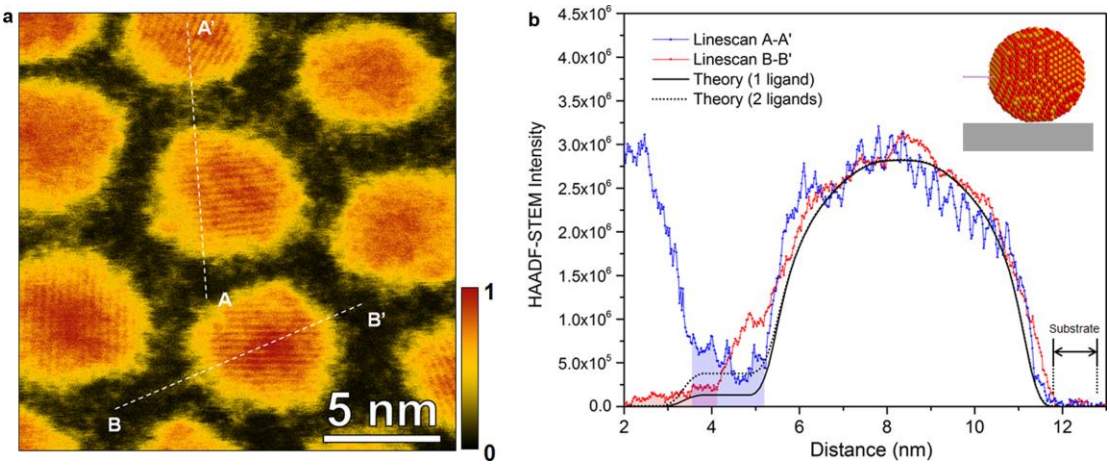

Figure 6.4. (a) HAADF-STEM image of as-synthesized PbSe nanocrystals from Figure 6.3b with positions of linescans A-A' and B-B'. (b) Intensity profiles of the linescan A-A' and B-B'. Calculated theoretical linescans based on the model shown in the inset are also shown: with 1 (solid black line) and 2 ligands (dotted black line) along the beam direction. The linescan A-A' appears to contain 2 and B-B' only 1 ligand along the beam direction.

The intensity profiles across the as-synthesized PbSe nanocrystals with ligands were also obtained from the raw HAADF-STEM image shown in Figure 6.3 (a or b). These are presented in Figure 6.4. The line profiles represent the raw HAADF-STEM image intensities without any contrast equalization. The intensity of the a:Si substrate has been subtracted from these linescan profiles resulting in zero average intensity from the substrate region. The linescan A-A' shows the intensity profile of a few wrapping oleic acid ligands between two PbSe nanocrystals. Linescan B-B' contains signal from 2.0 nm extended ligand measuring half of the intensity of the wrapping ligands in linescan A-A'. The extended ligand is more likely to consist of only one molecule of the oleic acid. This was confirmed using theoretical HAADF-STEM linescans calculated from a simple model containing oleic acid surface ligands attached to a ~ 6 nm PbSe nanocrystal sitting on a:Si TEM grids (inset in Figure 6.4b). The theoretical linescans were calculated based on the assumption that the intensity of HAADF-STEM image is roughly proportional to thickness of the sample the power of the atomic number, Z, of the materials, $I_{HAADF} \sim Z^{1.7}$.[192] The experimental linescan A-

A’ and B-B’ are in good agreement with these theoretical linescans. One and two ligands along the incident beam direction were considered here.

6.4 Geometric Arrangement of Ligands

The geometric arrangements of surface ligands were studied previously using molecular dynamics simulations of ligands bound to Pb atoms on perfectly faceted PbSe nanocrystals. These studies suggested that, generally, the ligands prefer to wrap around the surface when the number of the ligands is small. The same simulations showed that the ligands might stand in a more upright configuration (45^{o} off the normal to the surface) when the Pb atom density on the facet is large and the configuration space is limited.[187] The ratio of upright and wrapped ligands is determined by the balance between the van der Waals forces that tend to wrap the ligand around the surface and the entropic forces that tend to straighten the chains. This prediction is consistent with our experimental observations. Thickness and composition sensitive HAADF-STEM images of 6 nm as-synthesized PbSe nanocrystals (Figure 6.5) cast on thin a:Si TEM grids show that the oleic acid ligands form a corona around the nanocrystal surface. Most of the ligands are confined to a region less than 1 nm from the surface. Only a small fraction of the ligands are stretched and extend the entire length of the ligand, ~ 2 nm indicating that most of the ligands prefer conformations where the molecules stand at relatively small angles off the surface normal or lie against, and wrap around, the surface of the nanocrystals.

6.5 Partial Oxidation

Surprisingly, the appearance and structure of the oleate ligands on PbSe nanocrystals was a strong function of the period of time the nanocrystals were

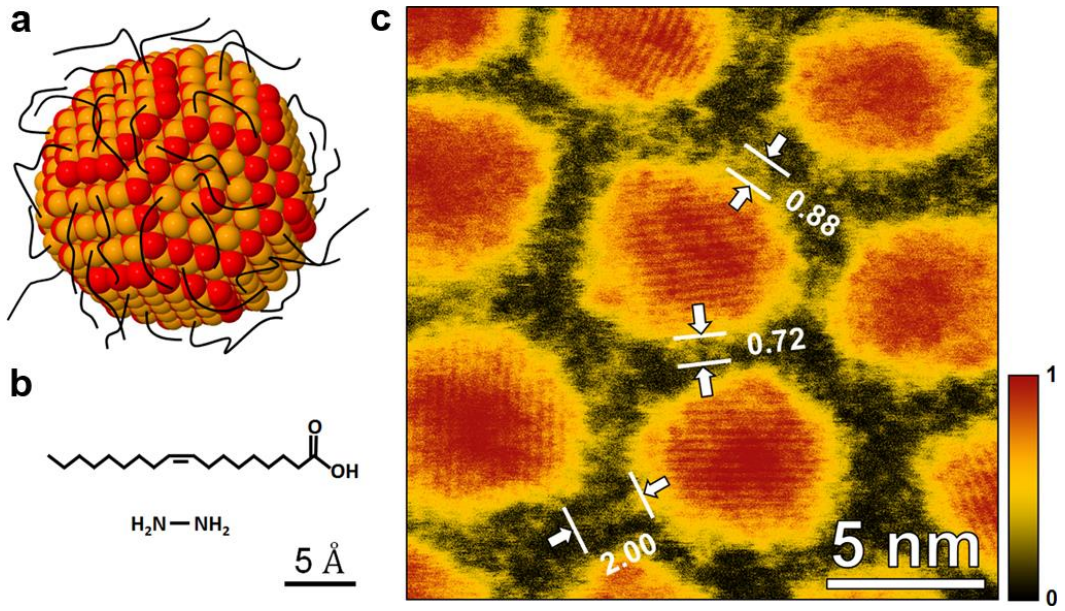

Figure 6.5. Geometric arrangements of the oleic acid ligands. (a) A schematic representation of the as-synthesized PbSe nanocrystal with oleic acid ligands. (b) Chemical structures of oleic acid and hydrazine molecules. (c) Atomic-resolution HAADF-STEM image of PbSe nanocrystals suspended on a ~ 5 nm thick a:Si TEM grids. Atomic planes along different crystallographic directions are visible for majority of the nanocrystals. The oleic acid ligands are attached to nanocrystals and extend to less than 1 nm radially from the surface of the nanocrystals. Indicated dimensions are in nanometers.

exposed to air. While it is well known that PbSe nanocrystals oxidize when exposed to air, the changes in the ligands surrounding the nanocrystals have not been examined before. Oxidation of the PbSe nanocrystals blue shifts their photoluminescence spectrum[193] and changes the electronic conductivities of the nanocrystal films.[194] We examined the structural changes within the oleic acid ligands upon oxidation. We exposed the PbSe nanocrystals to air for different durations and examined their surfaces and interfaces with other PbSe nanocrystals. HAADF-STEM images show that upon oxidation, the region between the PbSe core and the oleate ligand corona becomes blurry and the diameter of the core decreases by approximately 1 nm (Figure 6.6). These

changes are attributed to the formation of a self-limiting oxide shell on the nanocrystal surfaces.[188] During the early stages, when surface oxidation is minimal, the ligands are more stretched than those on the as-synthesized nanocrystals resulting in the interdigitation of the ligands with ones on adjacent nanocrystals (Figure 6.6b).

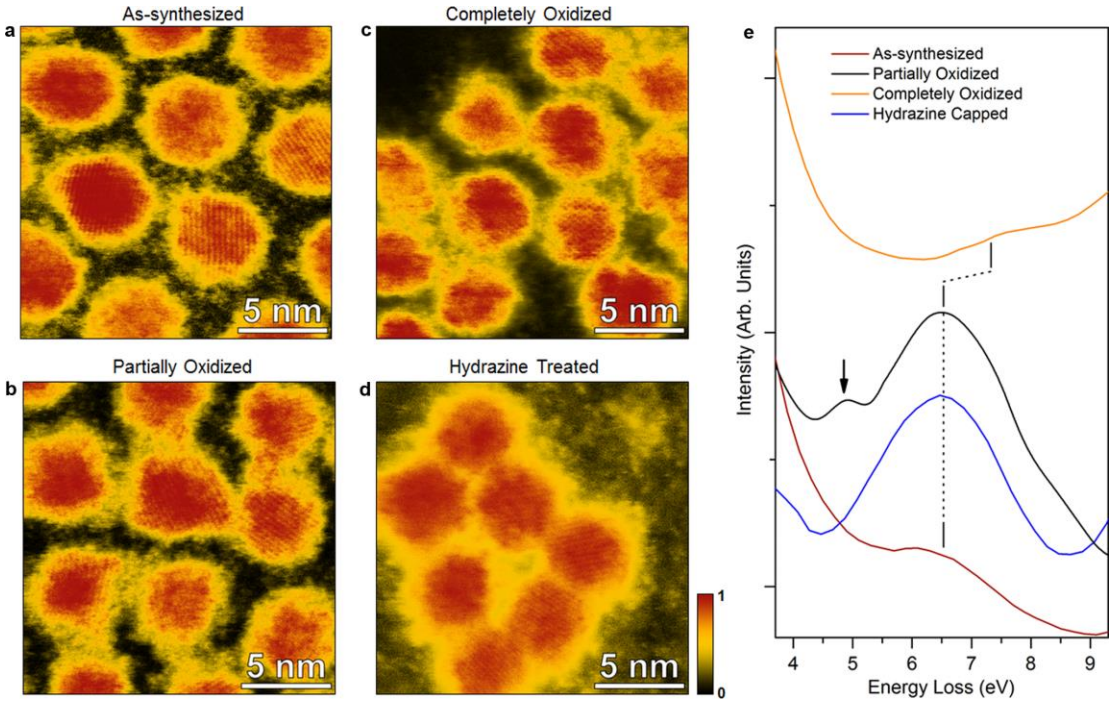

Figure 6.6. Atomic-resolution HAADF-STEM images and low-loss EELS of PbSe nanocrystals at different stages of oxidation. (a) as-synthesized, (b) partially oxidized, and (c) completely oxidized PbSe nanocrystals. Changes in ligands and reduction of nanocrystal size are visible as oxidation progresses. In the completely oxidized samples, the STEM probe beam first passes through the oxide shells on the outer surface resulting in additional spreading of the probe and hence the observed blurriness. (d) HAADF-STEM images of PbSe nanocrystals after hydrazine treatment. In hydrazine treated samples, the oleic acid ligands were removed and nanocrystals are structurally modified. The residuals of the hydrazine treatment can be seen on a:Si substrate. (e) Low-loss EELS measurements from oleic acid-capped PbSe nanocrystal at different stages of oxidation and when the ligands treated with hydrazine. The spectra are vertically shifted for clarity. Narrowing of the LSPR EELS peak at 6.5 eV at the early stage of oxidation is seen. After complete oxidation, the LSPR EELS peak shifts to 7.5 eV. When nanocrystals are partially oxidized, an additional peak due to π-plasmons at 4.5 eV (arrow) is also detected.

To understand the effects of oxidation on the nanocrystals and ligands we examined the nanocrystals with low energy loss EELS. The as-synthesized PbSe nanocrystals exhibit an EELS peak at 6.5 eV, which arises from the generation of LSPR in individual nanocrystals. The location of this peak agrees well with the frequency at which the Frölich condition is satisfied.[195] During the early stages of oxidation, LSPR EELS peak narrows and its intensity increases significantly (Figure 6.6e), which suggests that the plasmon lifetime also increases. However, when oxidation is complete, the LSPR EELS peak broadens again. The decrease in the plasmon lifetime with surface oxidation is easily understood because the oxide shell acts as an insulating barrier for the dephasing of the plasmons. The blue shift of the peak to 7.5 eV is also expected, due to changes in the size of nanocrystals after oxidation. However, the increase in the plasmon lifetime during the early stages of oxidation is unexpected.

The characteristic energy (or frequency) of localized surface plasmon resonance (LSPR) for PbSe nanocrystals can be estimated theoretically from the expression of complex polarizability of small spherical particles under the influence of excitation field of electron beam:[113]

$$\alpha(E) = \frac{\pi}{2} d^3 \frac{\varepsilon(E)-\epsilon_m}{\varepsilon(E)+2\epsilon_m}, \quad \text{(S1)}$$

where d is the nanocrystal diameter, $\varepsilon(E)$ is the dielectric function of PbSe nanocrystal and ε_m is the dielectric constant of the medium. The polarizability reaches the maximum value under resonant condition, when $|\varepsilon(E) + 2\epsilon_m|$ is at minimum or when $Re\big(\varepsilon(E)\big) = -2\epsilon_m$. This condition is called the Fröhlich criterion and occurs at 2.6 and 6.5 eV for PbSe nanocrystals in vacuum, for which $Re\big(\varepsilon(E)\big) \equiv \varepsilon_R = -2$, as estimated using the measured dielectric function of PbSe nanocrystals (Figure 6.7). While the resonance at 2.6 eV is hard to detect in

our low-loss EELS measurements due to lack of energy resolution and proximity to zero-loss peak, the resonance at 6.5 eV was readily observed.

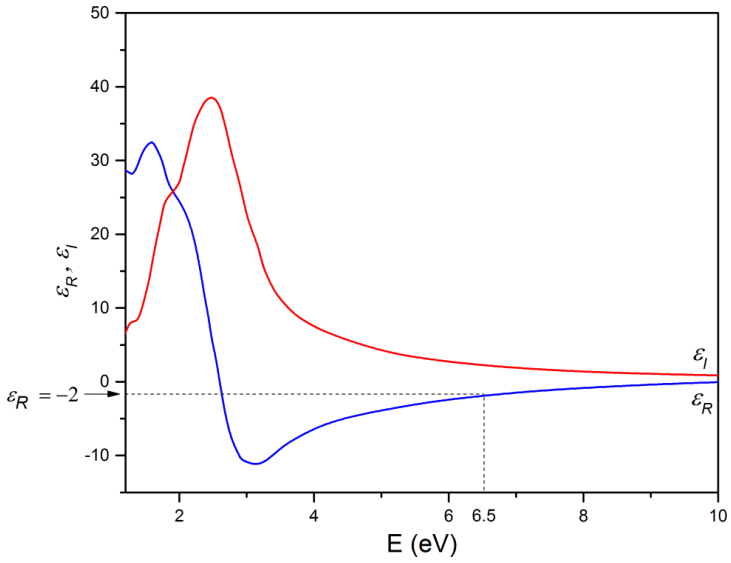

Figure 6.7. The $\boldsymbol{Re}(\varepsilon(\boldsymbol{E})) \equiv \boldsymbol{\varepsilon_R}(\boldsymbol{E})$ and $\boldsymbol{Im}(\boldsymbol{\varepsilon}(\boldsymbol{E})) \equiv \boldsymbol{\varepsilon_I}(\boldsymbol{E})$ parts of the dielectric function of PbSe nanocrystals deduced from complex dielectric function reported by Moreels, *et al.*[191]

6.6 EELS Carbon K-edge

A detailed core-level EELS study of the changes in bonding within the ligands during oxidation revealed the surprising reason for the plasmon lifetime increase. Figure 6.8 shows the carbon K-edge spectra collected from the oleic acid ligands on (i) as-synthesized, (ii) partially oxidized, (iii) completely oxidized, and (iv)hydrazine treated PbSe nanocrystals. The spectrum from as-synthesized nanocrystals shows a π* peak at 286 eV and a σ* onset around 288.5 eV (see Figure 6.8) with relative intensities similar to those recorded from oleic acid molecules not attached to a nanocrystal (recorded from dried molecules deposited on a:Si TEM grid). The oleic acid molecule has 16 carbon-carbon σ bonds and 1 carbon-carbon π bond. Apparently, in as-synthesized nanocrystals, the oleic acid ligands position, fold and wrap around the nanocrystals but do not

undergo any dramatic chemical changes when they are attached to the PbSe nanocrystals. However, changes in the internal bonds of the ligand are detected upon partial oxidation of the PbSe surface: specifically, the π* peak dramatically increases, indicating the formation of new π bonds.

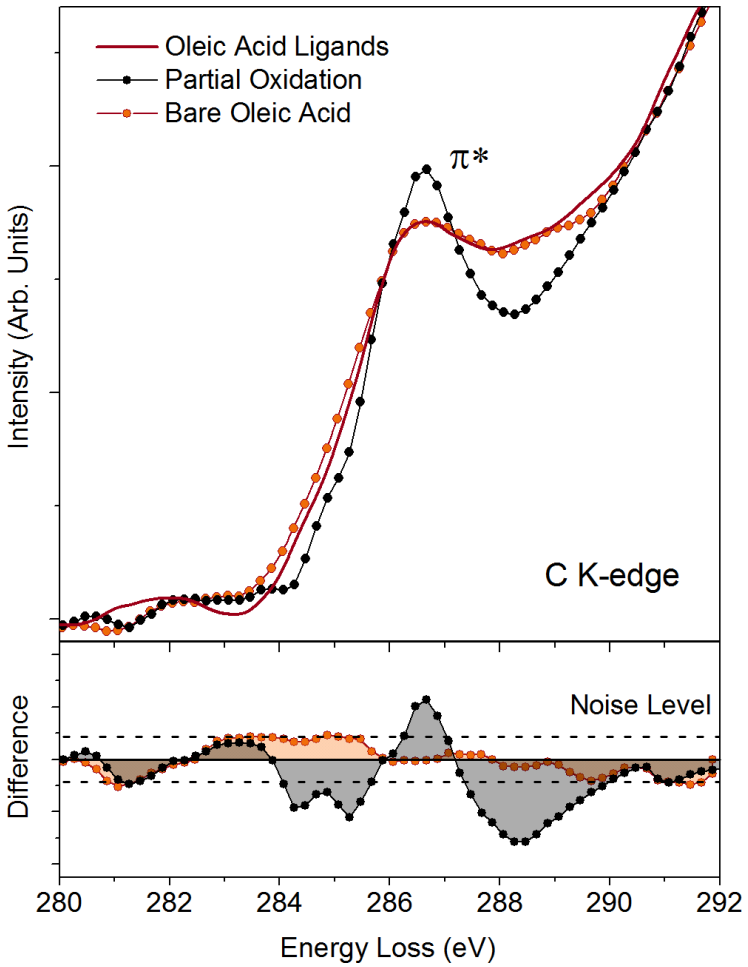

Figure 6.8 EELS carbon K-edges from ligands on PbSe nanocrystals before and after partial oxidation. Fine structures of the C K-edge recorded from oleic acid ligands when they are attached to the as-synthesized and partially oxidized PbSe nanocrystals. Spectrum from bare oleic acid molecules not attached to nanocrystals are also shown for comparison. Changes in π* peak are visible. Differences with respect to the C K-edge spectrum from oleic acid ligands on as-synthesized PbSe nanocrystal are shown at the bottom. The noise levels are indicated by the dashed lines.

In order to quantify the increase in π bonds in oleic acid ligands after partial oxidation, the fine structure of carbon K-edge EELS signal was analyzed. The fractions of sp^2 hybridized carbon-carbon bonds with respect to sp^3 hybridized bonds were computed. Here we calculate the ratio of the π* peak in C K-edge, after removing Gaussian tails from the σ* peak extending to the π* region (red-shaded are in Figure 6.9), to entire C K-edge (grey shaded area). As a reference we also measured, under similar conditions, the ratio of π* peak intensity to total (π* + σ*) intensity in a sample with known fractions of sp^2 and sp^3 bonds. Amorphous carbon substrate was used as such reference material (Table 6.1). The fractions of sp^2 carbon-carbon bonds in the oleic acid ligands for as-synthesized and partially oxidized samples were determined to be 13% and 55% respectively. The sp^2 fraction of carbon-carbon bonds in ligands of the as-synthesized nanoparticles is consistent with that in bare oleic acid molecules. Partially oxidized ligands contain about 4 times more sp^2 bonds than bare oleic acid molecule, or alternatively, about four π bonds on average.

Table 6.1. Summary of calculated sp^2 fractions for as-synthesized and partially oxidized ligands. For comparison the results from amorphous carbon and bare oleic acid molecules are also presented.

	$\frac{I_{\pi*}}{I_{\pi*} + I_{\sigma*}}$	$\% \, sp^2$
As Synthesized	0.028	13±2%
Partially Oxidized	0.038	55±2%
Oleic Acid	0.028	13±2%*
Amorphous Carbon	0.039	55%

*In oleic acid molecules with 18 carbon atoms %sp^2 is expected to be 11%.

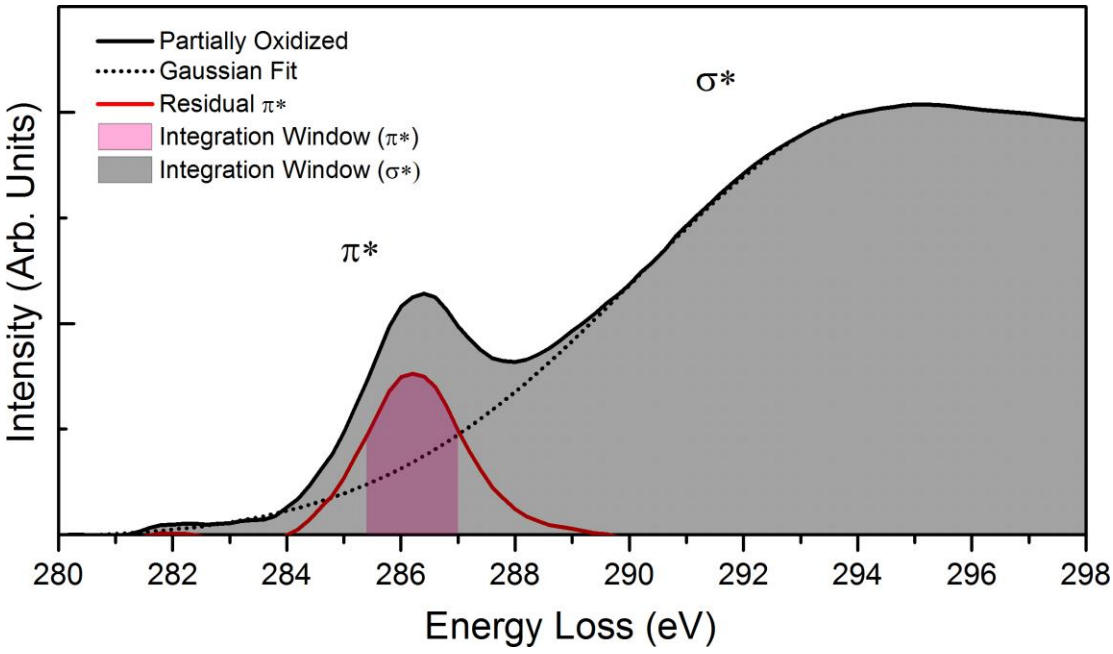

Figure 6.9. Quantification of the fraction of sp^2 carbon-carbon bonds in oleic acid ligands. The σ* region of C K-edge EELS data is fitted with a Gaussian function and subtracted. The residual signal (red curve) is the intensity of π* peak. To minimize the error, the ratios of the integrated intensity of the π* peak (red shaded area within 4 eV energy) to entire C K-edge intensity (gray shaded area within 20 eV energy window) were evaluated.

Additional evidence for appearance of new π bonds in the oleic acid ligands upon oxidation of the PbSe surface comes from the low-loss EELS (see Figure 6.6e). When the as-synthesized PbSe nanocrystals are partially oxidized, in addition to the LSPR peak at 6.5 eV, they also exhibit a weaker feature at 4.5 eV. This feature arises from the resonant oscillations of the delocalized π electrons, known as "π-plasmons". They are readily observed in graphene[196] and C_{60}.[197] Observation of π-plasmons and enhanced π* loss at the carbon K-edge within oleic acid ligands is conclusive evidence for the formation of new π bonds. Moreover, the presence of π-plasmons indicates that these new π bonds are conjugated and their electrons are delocalized.

6.7 Oxidative Dehydrogenation

Formation of conjugated double bonds on carboxylic acids such as oleic acid typically occurs through oxidative dehydrogenation mechanism. Oxygen reacts with saturated carbon bonds in oleic acid to produce H_2O and form π bonds between the adjacent carbon atoms.[198] The presence of catalysts has been shown to reduce the activation energy for such dehydrogenation reaction.[199] In the case of partially oxidized PbSe nanocrystals, the oxygen on the surface of the nanocrystals can act as an initiator for the oxidative dehydrogenation. Specifically, we surmise that the oxidized PbSe surface provides the oxygen atoms to the ligands that are in close proximity of the surface as they wrap around the nanocrystal. As conjugated double bonds form, the ligands stiffen,

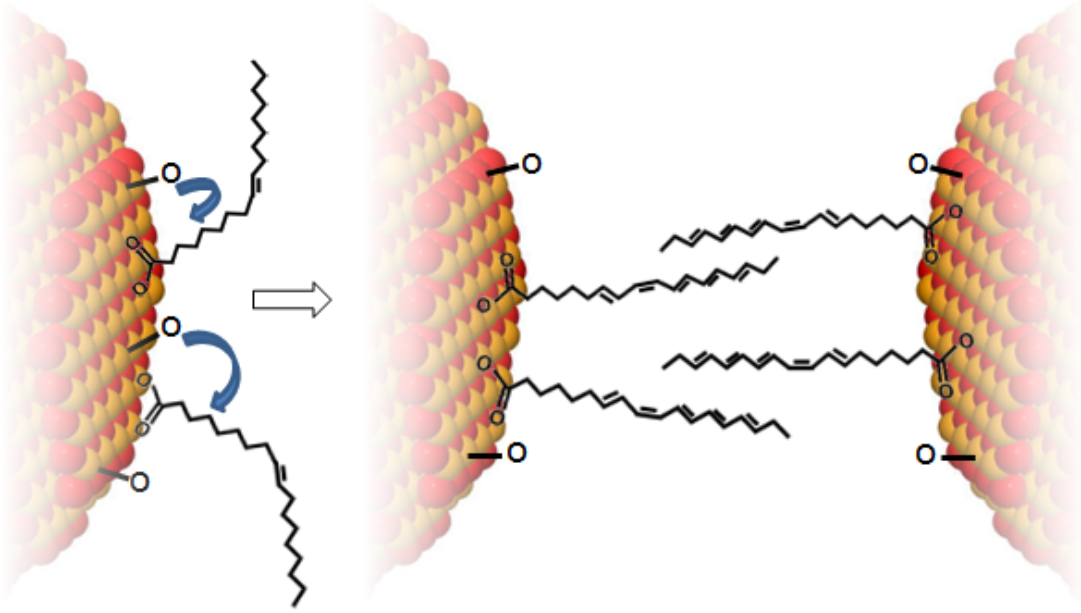

Figure 6.10. Schematic illustration of the changes in oleic acid ligands with oxidation. Oxidized PbSe nanocrystal acts as a catalyst for the wrapped ligands to undergo oxidative dehydrogenation by providing oxygen atoms. This dehydrogenation reaction with the formation of additional conjugated double bonds results in the disruption of the equilibrium wrapping arrangement and increase in the rigidity of the ligands facilitating interdigitation with neighboring ligands.

straighten out, and interdigitate with the ligands on neighboring nanocrystals (Figure 6.10). In the absence of PbSe nanocrystals, there is no detectable oxidative dehydrogenation as evident from EELS data from oleic acid molecules cast on the same TEM grids: there are no significant changes in the π* peak of the carbon K-edge in oleic acid molecules after they undergo similar oxidation treatment.

Oxidative dehydrogenation reaction typically occurs catalytically as well as non-catalytically. In the absence of catalysts, dehydrogenation in oleic acid molecules are initiated by heating to overcome the actvation energy, while in the presence of catalysts the reaction can proceed even at room temperature. The oxidative dehydrogenation of oleic acid ligands can be catalyzed by the oxidizing PbSe nanocrystal surfaces. The process occurs successively on each ligand with varying extent, producing ligands with different numbers of conjugated π bonds .[200] Examples of different successive oxidative dehydrogenations of oleic acid ligand are shown in Figure 6.11.

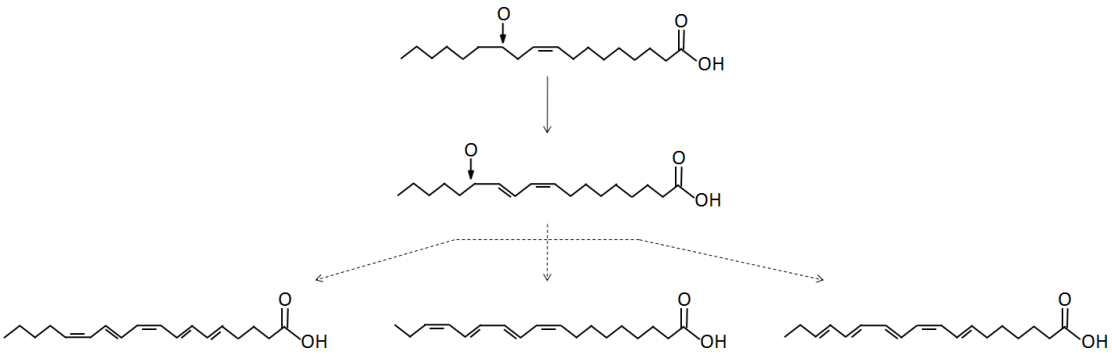

Figure 6.11. Examples of oxidative dehydrogenation processes occurring on the oleic acid ligands producing a varying extent of conjugated double carbon-carbon bonds.

When bare oleic acid molecules were exposed to identical oxidation environment as oleic acid ligands on PbSe nanocrystal, no detectable changes in the fine structure of the C K-edge EELS were observed (Figure 6.12), which

indicates that the oxidative dehydrogenation does not occur significantly in these molecules in the absence of catalysts at room temperature.

6.8 Energy Band Diagram

As illustrated in Figure 6.13, the oleic acid ligands on the as-synthesized nanocrystals passivate the dangling bonds of surface Pb atoms and introduce ligand states near the conduction band edge.[188, 201] The HOMO level of the ligands accepts electrons from the nanocrystals and act as dephasing routes for surface plasmons (see Figure 6.13). This dephasing is responsible for the broadening of the LSPR peak.[202] This decay mechanism is often referred to as "chemical interface damping". As the oxidation of the surface begins and surface oxygen facilitates the formation of conjugated ligands, conducting channels form between the nanocrystals. The conjugated ligands can support plasmonic interactions amongst the nanocrystals through charge transfer plasmons[203] (Figure 6.13b) and the plasmon decay mechanism via dephasing is removed. Consequently, the plasmon lifetime becomes longer, the LSPR peak narrows and the LSPR peak intensity in the low-loss EELS measurements increases (see Figure 6.6e). Similar LSPR peak narrowing and intensity enhancement with minimal red shift (<10 meV) have been observed previously when arrays of gold nanocrystals were brought closer together to induce electronic coupling.[204] We note that this charge transfer plasmon interaction is different from the more common dipolar interaction observed in metal nanocrystals at larger separation distances.[203]

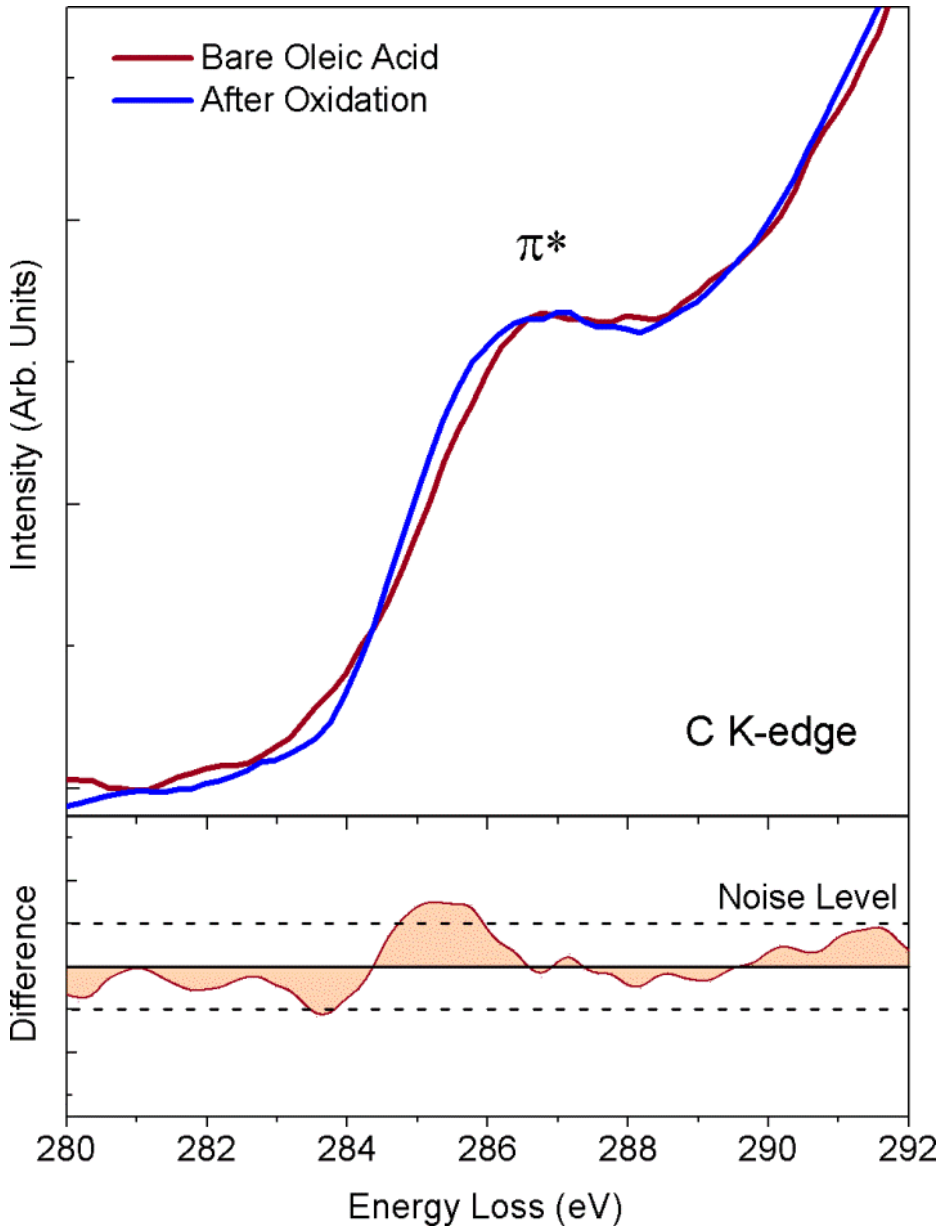

Figure 6.12. Carbon K-edge EELS from bare oleic acid molecules not attached to PbSe nanocrystals before and after exposure to oxidative environment showing no significant changes in the spectra (the difference of these to spectra with noise levels is shown at the bottom). This implies that, in the absence of catalysts, oxidative dehydrogenation does not occur at room temperature in these bare molecules when they are not attached to PbSe nanocrystals.

PbSe nanocrystals treated with hydrazine can be an excellent benchmark for evaluation of the surface plasmon lifetime and the LSPR peak, since hydrazine removes the oleic acid ligands and brings the nanocrystals as close to each other as possible (see Figures 6.6d and e). These touching nanocrystals have conducting channels between both the conduction bands and the valence bands of the neighboring nanocrystals through overlapping electronic wave-functions (Figure 6.13c).[122] Indeed, the LSPR excitations of the electrons in the conduction bands of the hydrazine-treated PbSe nanocrystals exhibit narrower and more intense LSPR peak than the LSPR of the as-synthesized and unoxidized PbSe nanocrystals. Remarkably, the intensities and widths of the LSPR peaks from hydrazine-treated and partially-oxidized PbSe nanocrystals are very similar indicating similar plasmon lifetimes and coupling between the nanocrystals. This is despite the significant distance (~ 1.5 nm) between the partially oxidized nanocrystals, which are still covered with long and conjugated ligands. The bulk plasmons, which originate from excitations of the valence band electrons, also exhibit the same behavior (Figure 6.13d).

The bulk plasmon in as-synthesized PbSe nanocrystals appears at 16 eV with FWHM of 11.5 eV. This peak increases in intensity and narrows upon hydrazine treatment (FWHM = 9 eV). Such narrowing of bulk plasmon peaks has been observed in Si nanocrystals[205] and polycrystalline Au films.[206] The hydrazine treatment also red shifts the bulk plasmon peak to 15 eV, closer to the value for bulk PbSe (14.9 eV).[207] This shift is associated with the loss of quantum confinement as the individual nanocrystals electronically couple to each other.[122, 205] In ensembles of partially oxidized nanocrystals, coupling of the valence band electrons between neighboring nanocrystals is not expected (Figure 6.13b) and no changes should be observed in the FWHM of the bulk plasmon excitations. Indeed, our EELS measurements show that FWHM of the bulk plasmon signal from partially oxidized nanocrystals is practically the same as that from as-synthesized oleic acid capped PbSe nanocrystals (Figure 6.13d).

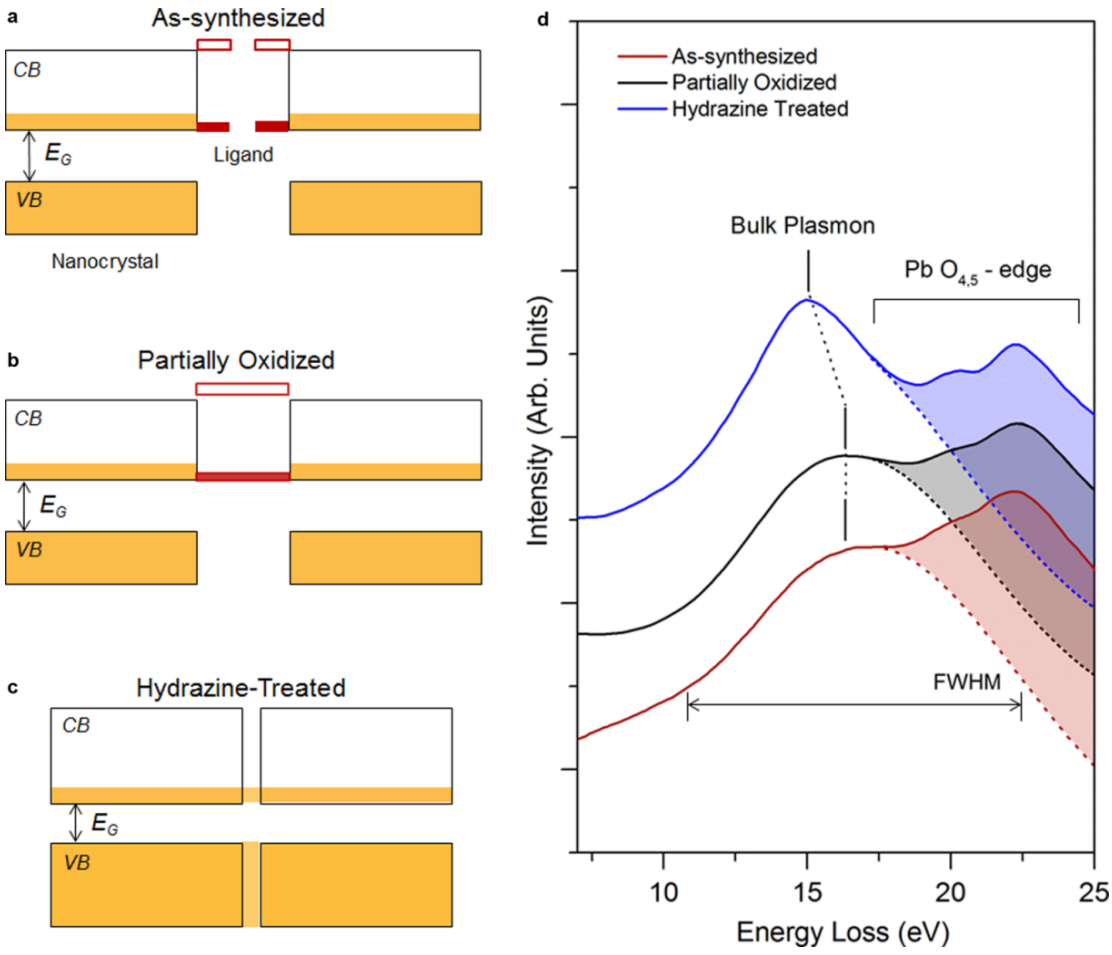

Figure 6.13. Schematic energy band diagrams for the PbSe nanocrystals and the ligands. (a) as-synthesized PbSe nanocrystal with oleic acid ligands, (b) partially oxidized PbSe nanocrystal with modified oleic acid ligands and (c) nanocrystals after hydrazine treatment. (d) Low-loss EELS measurements from oleic acid-capped PbSe nanocrystal at different stages of oxidation and when nanocrystals are treated with hydrazine. The spectra are vertically shifted for clarity. The FWHM of the bulk plasmon EELS peak narrows from 11.5 eV for as-synthesized and partially oxidized nanocrystals with oleic acid ligands to 9 eV for nanocrystals when treated with hydrazine. The Pb $O_{4,5}$-edge with onset at 17.5 eV is also detected in this EELS energy window.

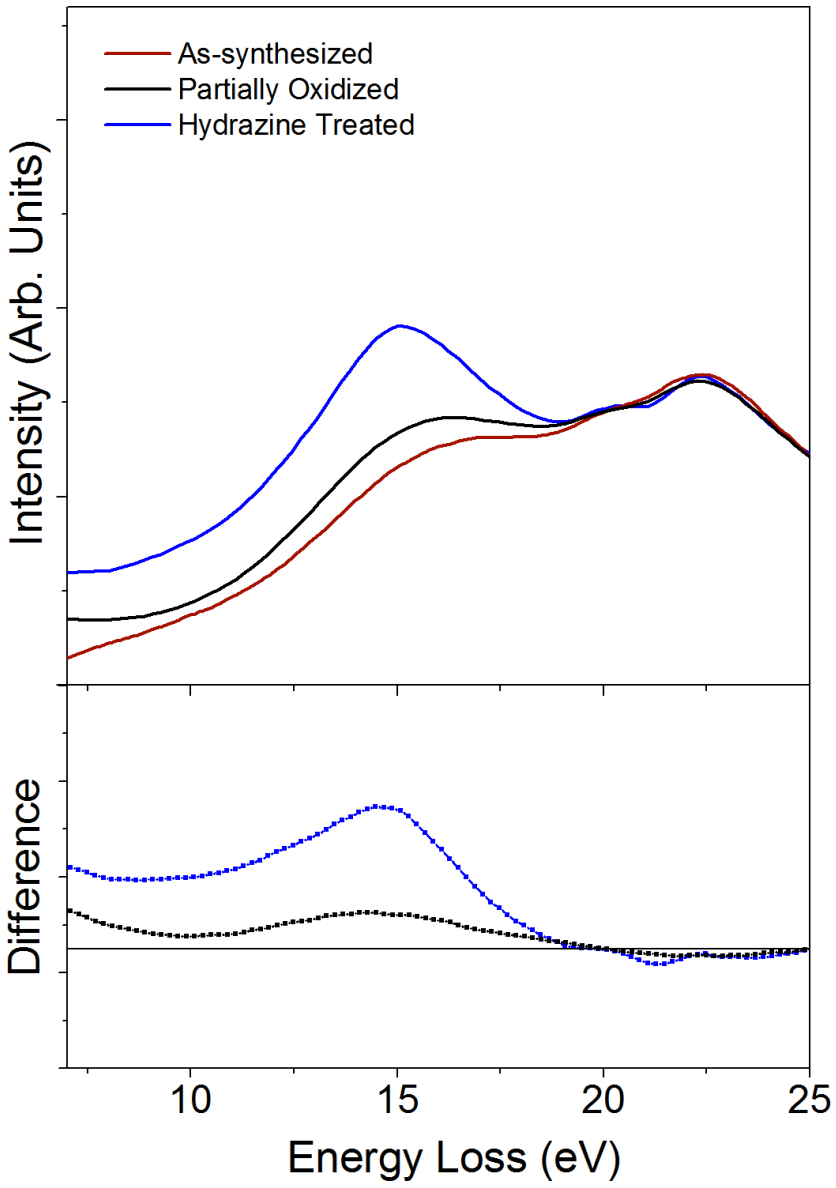

Figure 6.14. Bulk plasmon spectral differences. All three spectra were normalized to the intensity at 25 eV. This energy loss was chosen to normalize the spectra to core-level Pb $O_{4,5}$–edge intensity with minimal tail contribution from the bulk plasmon.

In order to highlight the differences in the bulk plasmon low-loss EELS, presented in Figure 6.13d in main text, spectral differences were evaluated and shown in Figure 6.14. The differences in bulk plasmon EELS from hydrazine-

treated and as-synthesized samples can be clearly seen. It is considerably larger than the differences in bulk plasmon EELS from partially oxidized and as-synthesized samples.

6.9 Summary and Future Work

Using analytical HAADF-STEM we have successfully imaged oleic acid ligands on PbSe nanocrystals and studied their chemical and conformational changes as the PbSe surface is oxidized. In as-synthesized nanocrystals, the ligands tend to wrap around the nanocrystal surface to maximize the nanocrystal core-ligand interaction. When exposed to atmosphere, PbSe nanocrystals begin to oxidize and the ligands undergo structural and chemical changes through oxidative dehydrogenation catalyzed by oxygen atoms on the nanocrystal surface. This oxidative dehydrogenation forms conjugated π bonds, which has profound effects on the electronic coupling between the nanocrystals. The π bonds stiffen the ligands enabling them to extend out and interdigitate with the ligands from neighboring nanocrystals. This provides enhanced electronic coupling between the nanocrystals. The effects of this coupling are detected with low-loss EELS measurements as enhanced plasmon lifetime and enhanced plasmon coupling between the nanocrystals.

It is interesting to study the electrical transport of these partially oxidized nanocrystals and observe whether enhancement in electrical conductivity is observed. Different types of chalcogenide based nanocrystals such as PbS could also be of interest. A better control of the amount of oxygen needed to induce the formation of conjugated bonds could also help in tuning these enhanced plasmonic interaction.

Bibliography

1. Huijben, M.; Brinkman, A.; Koster, G.; Rijnders, G.; Hilgenkamp, H.; Blank, D. H. A., Structure–Property Relation of $SrTiO_3/LaAlO_3$ Interfaces. *Advanced Materials* **2009,** *21*, 1665-1677.
2. Jeong, J. S.; Ambwani, P.; Jalan, B.; Leighton, C.; Mkhoyan, K. A., Observation of Electrically-Inactive Interstitials in Nb-Doped $SrTiO_3$. *ACS Nano* **2013,** *7*, 4487-4494.
3. Mkhoyan, K. A.; Kirkland, E. J.; Silcox, J.; Alldredge, E. S., Atomic level scanning transmission electron microscopy characterization of GaN/AlN quantum wells. *Journal of Applied Physics* **2004,** *96*, 738-746.
4. Mkhoyan, K. A.; Silcox, J.; Wu, H.; Schaff, W. J.; Eastman, L. F., Nonuniformities in GaN/AlN quantum wells. *Applied Physics Letters* **2003,** *83*, 2668-2670.
5. Mkhoyan, K. A.; Silcox, J.; Yu, Z.; Schaff, W. J.; Eastman, L. F., Formation of a quasi-two-dimensional electron gas in $GaN/Al_xGa_{1-x}N$ heterostructures with diffuse interfaces. *Journal of Applied Physics* **2004,** *95*, 1843-1848.
6. Muller, D. A.; Kourkoutis, L. F.; Murfitt, M.; Song, J. H.; Hwang, H. Y.; Silcox, J.; Dellby, N.; Krivanek, O. L., Atomic-Scale Chemical Imaging of Composition and Bonding by Aberration-Corrected Microscopy. *Science* **2008,** *319*, 1073-1076.
7. Lancin, M.; Marhic, C., TEM study of carbon fibre reinforced aluminium matrix composites: influence of brittle phases and interface on mechanical properties. *Journal of the European Ceramic Society* **2000,** *20*, 1493-1503.
8. Demczyk, B. G.; Wang, Y. M.; Cumings, J.; Hetman, M.; Han, W.; Zettl, A.; Ritchie, R. O., Direct mechanical measurement of the tensile strength and elastic modulus of multiwalled carbon nanotubes. *Materials Science and Engineering: A* **2002,** *334*, 173-178.
9. Haque, M. A.; A Saif, M. T., Mechanical behavior of 30–50 nm thick aluminum films under uniaxial tension. *Scripta Materialia* **2002,** *47*, 863-867.
10. Wei, Q.; Jiao, T.; Ramesh, K. T.; Ma, E.; Kecskes, L. J.; Magness, L.; Dowding, R.; Kazykhanov, V. U.; Valiev, R. Z., Mechanical behavior and dynamic failure of high-strength ultrafine grained tungsten under uniaxial compression. *Acta Materialia* **2006,** *54*, 77-87.
11. Meguid, S. A.; Sun, Y., On the tensile and shear strength of nano-reinforced composite interfaces. *Materials & Design* **2004,** *25*, 289-296.
12. Dai, J. Y.; Tee, S. F.; Tay, C. L.; Song, Z. G.; Ansari, S.; Er, E.; Redkar, S., Development of a rapid and automated TEM sample preparation method in semiconductor failure analysis and the study of the relevant TEM artifact. *Microelectronics Journal* **2001,** *32*, 221-226.
13. Bicaïis-Lépinay, N.; André, F.; Pantel, R.; Jullian, S.; Margain, A.; Kwakman, L. F. T., Lift-out techniques coupled with advanced TEM characterization

methods for electrical failure analysis. *Microelectronics Reliability* **2002,** *42*, 1747-1752.
14. Liu, X. H.; Huang, J. Y., In situ TEM electrochemistry of anode materials in lithium ion batteries. *Energy & Environmental Science* **2011,** *4*, 3844-3860.
15. Chowdhury, U.; Jimenez, J. L.; Lee, C.; Beam, E.; Saunier, P.; Balistreri, T.; Seong-Yong, P.; Taehun, L.; Wang, J.; Kim, M. J.; Jungwoo, J.; del Alamo, J. A., TEM Observation of Crack- and Pit-Shaped Defects in Electrically Degraded GaN HEMTs. *Electron Device Letters, IEEE* **2008,** *29*, 1098-1100.
16. Xu, Z.; Golberg, D.; Bando, Y., In Situ TEM-STM Recorded Kinetics of Boron Nitride Nanotube Failure under Current Flow. *Nano Letters* **2009,** *9*, 2251-2254.
17. Murakami, Y.; Shindo, D.; Oikawa, K.; Kainuma, R.; Ishida, K., Magnetic domain structure in a ferromagnetic shape memory alloy $Ni_{2+x}Fe_{1-x}Ga$ studied by electron holography and Lorentz microscopy. *Applied Physics Letters* **2003,** *82*, 3695-3697.
18. De Graef, M.; Willard, M. A.; McHenry, M. E.; Yimei, Z., In-situ Lorentz TEM cooling study of magnetic domain configurations in Ni_2MnGa. *Magnetics, IEEE Transactions on* **2001,** *37*, 2663-2665.
19. Marshall, A. F.; Klein, L.; Dodge, J. S.; Ahn, C. H.; Reiner, J. W.; Mieville, L.; Antagonazza, L.; Kapitulnik, A.; Geballe, T. H.; Beasley, M. R., Lorentz transmission electron microscope study of ferromagnetic domain walls in $SrRuO_3$ Statics, dynamics, and crystal structure correlation. *Journal of Applied Physics* **1999,** *85*, 4131-4140.
20. Yu, R. H.; Basu, S.; Zhang, Y.; Xiao, J. Q., Magnetic domains and coercivity in FeCo soft magnetic alloys. *Journal of Applied Physics* **1999,** *85*, 6034-6036.
21. Yu, X. Z.; Kanazawa, N.; Onose, Y.; Kimoto, K.; Zhang, W. Z.; Ishiwata, S.; Matsui, Y.; Tokura, Y., Near room-temperature formation of a skyrmion crystal in thin-films of the helimagnet FeGe. *Nat Mater* **2011,** *10*, 106-109.
22. Kuwahara, M.; Kusunoki, S.; Jin, X. G.; Nakanishi, T.; Takeda, Y.; Saitoh, K.; Ujihara, T.; Asano, H.; Tanaka, N., 30-kV spin-polarized transmission electron microscope with GaAs-GaAsP strained superlattice photocathode. *Applied Physics Letters* **2012,** *101*, 033102-033102-4.
23. Perkins, G. A.; Renken, C. W.; Song, J. Y.; Frey, T. G.; Young, S. J.; Lamont, S.; Martone, M. E.; Lindsey, S.; Ellisman, M. H., Electron Tomography of Large, Multicomponent Biological Structures. *Journal of Structural Biology* **1997,** *120*, 219-227.
24. Aoyama, K.; Takagi, T.; Hirase, A.; Miyazawa, A., STEM tomography for thick biological specimens. *Ultramicroscopy* **2008,** *109*, 70-80.
25. Marko, M.; Hsieh, C.; Schalek, R.; Frank, J.; Mannella, C., Focused-ion-beam thinning of frozen-hydrated biological specimens for cryo-electron microscopy. *Nat Meth* **2007,** *4*, 215-217.
26. McMahon, P. J.; Barone-Nugent, E. D.; Allman, B. E.; Nugent, K. A., Quantitative phase-amplitude microscopy II: differential interference

contrast imaging for biological TEM. *Journal of Microscopy* **2002,** *206*, 204-208.
27. McEwen, B. F.; Marko, M., The Emergence of Electron Tomography as an Important Tool for Investigating Cellular Ultrastructure. *Journal of Histochemistry & Cytochemistry* **2001,** *49*, 553-563.
28. Koon, H. E. C.; Nicholson, R. A.; Collins, M. J., A practical approach to the identification of low temperature heated bone using TEM. *Journal of Archaeological Science* **2003,** *30*, 1393-1399.
29. Wilson, A. S.; Dodson, H. I.; Janaway, R. C.; Pollard, A. M.; Tobin, D. J., Selective biodegradation in hair shafts derived from archaeological, forensic and experimental contexts. *British Journal of Dermatology* **2007,** *157*, 450-457.
30. Leech, R. W.; Freeman, T.; Johnson, R., Colloid cyst of the third ventricle. *Journal of Neurosurgery* **1982,** *57*, 108-113.
31. Lunetta, P.; Penttilä, A.; Hällfors, G., Scanning and transmission electron microscopical evidence of the capacity of diatoms to penetrate the alveolo-capillary barrier in drowning. *Int J Leg Med* **1998,** *111*, 229-237.
32. Lim, D. J.; Melnick, W., Acoustic damage of the cochlea: A scanning and transmission electron microscopic observation. *Archives of Otolaryngology* **1971,** *94*, 294-305.
33. Lavker, R. M.; Zheng, P.; Dong, G., Aged Skin: A Study by Light, Transmission Electron, and Scanning Electron Microscopy. *J Investig Dermatol* **1987,** *88*, 44-51.
34. Dvorak, A. M.; Monahan, R. A.; Osage, J. E.; Dickersin, G. R., Crohn's disease: Transmission electron microscopic studies: II. Immunologic inflammatory response. Alterations of mast cells, basophils, eosinophils, and the microvasculature. *Human Pathology* **1980,** *11*, 606-619.
35. Hashimoto, M.; Ohno, H.; Sano, H.; Kaga, M.; Oguchi, H., In vitro degradation of resin–dentin bonds analyzed by microtensile bond test, scanning and transmission electron microscopy. *Biomaterials* **2003,** *24*, 3795-3803.
36. Wittman, C. L.; Meyers, M. A.; Pak, H. R., Observation of an adiabatic shear band in AISI 4340 steel by high-voltage transmission electron microscopy. *MTA* **1990,** *21*, 707-716.
37. Cherns, D., Direct resolution of surface atomic steps by transmission electron microscopy. *Philosophical Magazine* **1974,** *30*, 549-556.
38. Mahon, G. J.; Howe, J. M., Transmission electron microscopy investigation of interfaces in a two-phase TiAl alloy. *MTA* **1990,** *21*, 1655-1662.
39. Dobrzhinetskaya, L. F.; Green, H. W.; Weschler, M.; Darus, M.; Wang, Y.-C.; Massonne, H.-J.; Stöckhert, B., Focused ion beam technique and transmission electron microscope studies of microdiamonds from the Saxonian Erzgebirge, Germany. *Earth and Planetary Science Letters* **2003,** *210*, 399-410.

40. Wang, X.; Liu, F.; Tan, W.; Feng, X.; Koopal, L. K., Transformation of hydroxycarbonate green rust into crystalline iron (hydr)oxides: Influences of reaction conditions and underlying mechanisms. *Chemical Geology* **2013,** *351*, 57-65.
41. Wang, A.; Dhamenincourt, P.; Dubessy, J.; Guerard, D.; Landais, P.; Lelaurain, M., Characterization of graphite alteration in an uranium deposit by micro-Raman spectroscopy, X-ray diffraction, transmission electron microscopy and scanning electron microscopy. *Carbon* **1989,** *27*, 209-218.
42. Eggleton, R.; Buseck, P., The orthoclase-microcline inversion: A high-resolution transmission electron microscope study and strain analysis. *Contr. Mineral. and Petrol.* **1980,** *74*, 123-133.
43. Zuo, J. M.; Kim, M.; O'Keeffe, M.; Spence, J. C. H., Direct observation of d-orbital holes and Cu-Cu bonding in Cu2O. *Nature* **1999,** *401*, 49-52.
44. Asaka, T.; Yamada, S.; Tsutsumi, S.; Tsuruta, C.; Kimoto, K.; Arima, T.; Matsui, Y., Charge/Orbital Ordering Structure of $Pr_{1-x}Ca_xMnO3$ (x=3/8) Examined by Low-Temperature Transmission Electron Microscopy. *Physical Review Letters* **2002,** *88*, 097201.
45. Nakashima, P. N. H.; Smith, A. E.; Etheridge, J.; Muddle, B. C., The Bonding Electron Density in Aluminum. *Science* **2011,** *331*, 1583-1586.
46. Wang, Z. L.; Poncharal, P.; de Heer, W. A., Measuring physical and mechanical properties of individual carbon nanotubes by in situ TEM. *Journal of Physics and Chemistry of Solids* **2000,** *61*, 1025-1030.
47. Legros, M.; Gianola, D. S.; Hemker, K. J., In situ TEM observations of fast grain-boundary motion in stressed nanocrystalline aluminum films. *Acta Materialia* **2008,** *56*, 3380-3393.
48. Crozier, P. A.; Wang, R.; Sharma, R., In situ environmental TEM studies of dynamic changes in cerium-based oxides nanoparticles during redox processes. *Ultramicroscopy* **2008,** *108*, 1432-1440.
49. Gai, P. L.; Boyes, E. D., Advances in atomic resolution in situ environmental transmission electron microscopy and 1Å aberration corrected in situ electron microscopy. *Microscopy Research and Technique* **2009,** *72*, 153-164.
50. Chenna, S.; Banerjee, R.; Crozier, P. A., Atomic-Scale Observation of the Ni Activation Process for Partial Oxidation of Methane Using In Situ Environmental TEM. *ChemCatChem* **2011,** *3*, 1051-1059.
51. Gai, P. L., Development of Wet Environmental TEM (Wet-ETEM) for In Situ Studies of Liquid-Catalyst Reactions on the Nanoscale. *Microscopy and Microanalysis* **2002,** *8*, 21-28.
52. Chuvilin, A.; Kaiser, U., On the peculiarities of CBED pattern formation revealed by multislice simulation. *Ultramicroscopy* **2005,** *104*, 73-82.
53. A. Muller, D.; Edwards, B.; J. Kirkland, E.; Silcox, J., Simulation of thermal diffuse scattering including a detailed phonon dispersion curve. *Ultramicroscopy* **2001,** *86*, 371-380.

54. Lupini, A. R.; Pennycook, S. J., Localization in elastic and inelastic scattering. *Ultramicroscopy* **2003,** *96*, 313-322.
55. Egerton, R. F.; Cheng, S. C., Measurement of local thickness by electron energy-loss spectroscopy. *Ultramicroscopy* **1987,** *21*, 231-244.
56. Iakoubovskii, K.; Mitsuishi, K.; Nakayama, Y.; Furuya, K., Thickness measurements with electron energy loss spectroscopy. *Microscopy Research and Technique* **2008,** *71*, 626-631.
57. Malis, T.; Cheng, S. C.; Egerton, R. F., EELS log-ratio technique for specimen-thickness measurement in the TEM. *Journal of Electron Microscopy Technique* **1988,** *8*, 193-200.
58. Smith, B. W.; Luzzi, D. E., Electron irradiation effects in single wall carbon nanotubes. *Journal of Applied Physics* **2001,** *90*, 3509-3515.
59. Csencsits, R.; Gronsky, R., Damage of zeolite Y in the TEM and its effects on TEM images. *Ultramicroscopy* **1987,** *23*, 421-431.
60. Muller, D. A., Structure and bonding at the atomic scale by scanning transmission electron microscopy. *Nat Mater*\ **2009,** *8*, 263-270.
61. Alem, N.; Erni, R.; Kisielowski, C.; Rossell, M. D.; Gannett, W.; Zettl, A., Atomically thin hexagonal boron nitride probed by ultrahigh-resolution transmission electron microscopy. *Physical Review B* **2009,** *80*, 155425.
62. Ugurlu, O.; Haus, J.; Gunawan, A. A.; Thomas, M. G.; Maheshwari, S.; Tsapatsis, M.; Mkhoyan, K. A., Radiolysis to knock-on damage transition in zeolites under electron beam irradiation. *Physical Review B* **2011,** *83*, 113408.
63. Park, K.; Salamanca-Riba, L.; Jonker, B. T., Microstructural properties of (ZnSe/FeSe) and (ZnSe/MnSe) diluted magnetic semiconductor superlattices (abstract). *Journal of Applied Physics* **1996,** *79*, 5195-5195.
64. Jin, C.; Zhang, B.; Ling, Z.; Wang, J.; Hou, X.; Segawa, Y.; Wang, X., Growth and optical characterization of diluted magnetic semiconductor $Zn_{1-x}Mn_xSe$/ZnSe strained-layer superlattices. *Journal of Applied Physics* **1997,** *81*, 5148-5150.
65. Kuo, M. C.; Hsu, J. S.; Shen, J. L.; Chiu, K. C.; Fan, W. C.; Lin, Y. C.; Chia, C. H.; Chou, W. C.; Yasar, M.; Mallory, R.; Petrou, A.; Luo, H., Photoluminescence studies of type-II diluted magnetic semiconductor ZnMnTe/ZnSe quantum dots. *Applied Physics Letters* **2006,** *89*, 263111-3.
66. Triki, M.; Afia, S. B.; Jaziri, S., Electron states in CdMnSe/ZnSe and in CdSe/ZnMnSe diluted magnetic semiconductor quantum dots. *physica status solidi (c)* **2009,** *6*, 845-848.
67. Sato, K.; Katayama-Yoshida, H., Ab initio Study on the Magnetism in ZnO-, ZnS-, ZnSe- and ZnTe-Based Diluted Magnetic Semiconductors. *physica status solidi (b)* **2002,** *229*, 673-680.
68. van Benthem, K.; Lupini, A. R.; Kim, M.; Hion-Suck, B.; Doh, S.; Jong-Ho, L.; Oxley, M. P.; Findlay, S. D.; Allen, L. J.; Luck, J. T.; Pennycook, S. J., Three-dimensional imaging of individual hafnium atoms inside a semiconductor device. *Applied Physics Letters* **2005,** *87*, 034104-034104-3.

69. Weis, C. D.; Schuh, A.; Batra, A.; Persaud, A.; Rangelow, I. W.; Bokor, J.; Lo, C. C.; Cabrini, S.; Sideras-Haddad, E.; Fuchs, G. D.; Hanson, R.; Awschalom, D. D.; Schenkel, T. In *Single atom doping for quantum device development in diamond and silicon*, AVS: 2008; pp 2596-2600.
70. Lansbergen, G. P.; Rahman, R.; Wellard, C. J.; Woo, I.; Caro, J.; Collaert, N.; Biesemans, S.; Klimeck, G.; Hollenberg, L. C. L.; Rogge, S., Gate-induced quantum-confinement transition of a single dopant atom in a silicon FinFET. *Nat Phys* **2008,** *4*, 656-661.
71. Wang, S.; Borisevich, A. Y.; Rashkeev, S. N.; Glazoff, M. V.; Sohlberg, K.; Pennycook, S. J.; Pantelides, S. T., Dopants adsorbed as single atoms prevent degradation of catalysts. *Nat Mater* **2004,** *3*, 143-146.
72. Shinada, T.; Okamoto, S.; Kobayashi, T.; Ohdomari, I., Enhancing semiconductor device performance using ordered dopant arrays. *Nature* **2005,** *437*, 1128-1131.
73. Schofield, S. R.; Curson, N. J.; Simmons, M. Y.; Rueß, F. J.; Hallam, T.; Oberbeck, L.; Clark, R. G., Atomically Precise Placement of Single Dopants in Si. *Physical Review Letters* **2003,** *91*, 136104.
74. Pradhan, N.; Peng, X., Efficient and Color-Tunable Mn-Doped ZnSe Nanocrystal Emitters: Control of Optical Performance via Greener Synthetic Chemistry. *Journal of the American Chemical Society* **2007,** *129*, 3339-3347.
75. Zeng, R.; Rutherford, M.; Xie, R.; Zou, B.; Peng, X., Synthesis of Highly Emissive Mn-Doped ZnSe Nanocrystals without Pyrophoric Reagents. *Chemistry of Materials* **2010,** *22*, 2107-2113.
76. Zu, L.; Norris, D. J.; Kennedy, T. A.; Erwin, S. C.; Efros, A. L., Impact of Ripening on Manganese-Doped ZnSe Nanocrystals. *Nano Letters* **2005,** *6*, 334-340.
77. Acharya, S.; Sarma, D. D.; Jana, N. R.; Pradhan, N., An Alternate Route to High-Quality ZnSe and Mn-Doped ZnSe Nanocrystals. *The Journal of Physical Chemistry Letters* **2009,** *1*, 485-488.
78. Pradhan, N.; Goorskey, D.; Thessing, J.; Peng, X., An Alternative of CdSe Nanocrystal Emitters: Pure and Tunable Impurity Emissions in ZnSe Nanocrystals. *Journal of the American Chemical Society* **2005,** *127*, 17586-17587.
79. Pietryga, J. M.; Schaller, R. D.; Werder, D.; Stewart, M. H.; Klimov, V. I.; Hollingsworth, J. A., Pushing the Band Gap Envelope: Mid-Infrared Emitting Colloidal PbSe Quantum Dots. *Journal of the American Chemical Society* **2004,** *126*, 11752-11753.
80. H. Sargent, E., Infrared Quantum Dots. *Advanced Materials* **2005,** *17*, 515-522.
81. Schaller, R. D.; Petruska, M. A.; Klimov, V. I., Tunable Near-Infrared Optical Gain and Amplified Spontaneous Emission Using PbSe Nanocrystals. *The Journal of Physical Chemistry B* **2003,** *107*, 13765-13768.

82. Luther, J. M.; Law, M.; Beard, M. C.; Song, Q.; Reese, M. O.; Ellingson, R. J.; Nozik, A. J., Schottky Solar Cells Based on Colloidal Nanocrystal Films. *Nano Letters* **2008,** *8*, 3488-3492.
83. Law, M.; Beard, M. C.; Choi, S.; Luther, J. M.; Hanna, M. C.; Nozik, A. J., Determining the Internal Quantum Efficiency of PbSe Nanocrystal Solar Cells with the Aid of an Optical Model. *Nano Letters* **2008,** *8*, 3904-3910.
84. Leschkies, K. S.; Beatty, T. J.; Kang, M. S.; Norris, D. J.; Aydil, E. S., Solar Cells Based on Junctions between Colloidal PbSe Nanocrystals and Thin ZnO Films. *ACS Nano* **2009,** *3*, 3638-3648.
85. Choi, J. J.; Lim, Y.-F.; Santiago-Berrios, M. E. B.; Oh, M.; Hyun, B.-R.; Sun, L.; Bartnik, A. C.; Goedhart, A.; Malliaras, G. G.; Abruña, H. c. D.; Wise, F. W.; Hanrath, T., PbSe Nanocrystal Excitonic Solar Cells. *Nano Letters* **2009,** *9*, 3749-3755.
86. Liu, Y.; Gibbs, M.; Puthussery, J.; Gaik, S.; Ihly, R.; Hillhouse, H. W.; Law, M., Dependence of Carrier Mobility on Nanocrystal Size and Ligand Length in PbSe Nanocrystal Solids. *Nano Letters* **2010,** *10*, 1960-1969.
87. Luther, J. M.; Beard, M. C.; Song, Q.; Law, M.; Ellingson, R. J.; Nozik, A. J., Multiple Exciton Generation in Films of Electronically Coupled PbSe Quantum Dots. *Nano Letters* **2007,** *7*, 1779-1784.
88. Ruska, E., *The Early Development of Electron Lenses and Electron Microscopy (translated by T Mulvey)* S Hirzel Verlag Stuttgart.: 1980.
89. Williams, D. B., Carter, C. Barry, *Transmission Electron Microscopy*. Springer: 2009.
90. http://ncem.lbl.gov/frames/tecnai.htm.
91. Kirkland, E. J., *Advanced Computing in Electron Microscopy*. Springer: 2010.
92. Pennycook, S. J., Nellist, P. D. , *Scanning Transmission Electron Microscopy: Imaging and Analysis*. Springer: 2011.
93. Crewe, A. V.; Wall, J., A scanning microscope with 5 Å resolution. *Journal of Molecular Biology* **1970,** *48*, 375-393.
94. Crewe, A. V.; Wall, J.; Langmore, J., Visibility of Single Atoms. *Science* **1970,** *168*, 1338-1340.
95. Edgerton, R. F., *Electron Energy Loss Spectroscopy in the Electron Microscope*. Springer: 2011.
96. Ruthemann, G., Diskrete Energieverluste schneller Elektronen in Festkörpern. *Naturwissenschaften* **1941,** *29*, 648-648.
97. Semonin, O. E.; Luther, J. M.; Choi, S.; Chen, H.-Y.; Gao, J.; Nozik, A. J.; Beard, M. C., Peak External Photocurrent Quantum Efficiency Exceeding 100% via MEG in a Quantum Dot Solar Cell. *Science* **2011,** *334*, 1530-1533.
98. Haider, M.; Uhlemann, S.; Zach, J., Upper limits for the residual aberrations of a high-resolution aberration-corrected STEM. *Ultramicroscopy* **2000,** *81*, 163-175.
99. Haider, M.; Rose, H.; Uhlemann, S.; Schwan, E.; Kabius, B.; Urban, K., A spherical-aberration-corrected 200 kV transmission electron microscope. *Ultramicroscopy* **1998,** *75*, 53-60.

100. Krivanek, O. L.; Dellby, N.; Lupini, A. R., Towards sub-Å electron beams. *Ultramicroscopy* **1999,** *78*, 1-11.
101. http://www.ceos-gmbh.de/.
102. Image courtesy of Prashant Kumar
103. Image courtesy of Dan Schaub
104. Ritchie, R. H., Plasma Losses by Fast Electrons in Thin Films. *Physical Review* **1957,** *106*, 874-881.
105. Grosso, G. a. P., G., *Solid State Physics*. Academic Press: 2000.
106. Mkhoyan, K. A.; Babinec, T.; Maccagnano, S. E.; Kirkland, E. J.; Silcox, J., Separation of bulk and surface-losses in low-loss EELS measurements in STEM. *Ultramicroscopy* **2007,** *107*, 345-355.
107. Gordon, D. J., Mie scattering by optically active particles. *Biochemistry* **1972,** *11*, 413-420.
108. Pines, D.; Bohm, D., A Collective Description of Electron Interactions: II. Collective vs Individual Particle Aspects of the Interactions. *Physical Review* **1952,** *85*, 338-353.
109. Atwater, H. A.; Polman, A., Plasmonics for improved photovoltaic devices. *Nat Mater* **2010,** *9*, 205-213.
110. Ferry, V. E.; Sweatlock, L. A.; Pacifici, D.; Atwater, H. A., Plasmonic Nanostructure Design for Efficient Light Coupling into Solar Cells. *Nano Letters* **2008,** *8*, 4391-4397.
111. Homola, J.; Yee, S. S.; Gauglitz, G., Surface plasmon resonance sensors: review. *Sensors and Actuators B: Chemical* **1999,** *54*, 3-15.
112. Haes, A. J.; Van Duyne, R. P., A Nanoscale Optical Biosensor: Sensitivity and Selectivity of an Approach Based on the Localized Surface Plasmon Resonance Spectroscopy of Triangular Silver Nanoparticles. *Journal of the American Chemical Society* **2002,** *124*, 10596-10604.
113. Maier, S., *Plasmonics Fundamentals and Applications*. Springer: 2007.
114. García de Abajo, F. J., Optical excitations in electron microscopy. *Reviews of Modern Physics* **2010,** *82*, 209-275.
115. Chen, K.-P.; Drachev, V. P.; Borneman, J. D.; Kildishev, A. V.; Shalaev, V. M., Drude Relaxation Rate in Grained Gold Nanoantennas. *Nano Letters* **2010,** *10*, 916-922.
116. Mitome, M.; Yamazaki, Y.; Takagi, H.; Nakagiri, T., Size dependence of plasmon energy in Si clusters. *Journal of Applied Physics* **1992,** *72*, 812-814.
117. Anatoliy, P.; Uwe, K., Interface decay channel of particle surface plasmon resonance. *New Journal of Physics* **2003,** *5*, 151.
118. Garcia, M. A.; de la Venta, J.; Crespo, P.; Llopis, J.; Penadés, S.; Fernández, A.; Hernando, A., Surface plasmon resonance of capped Au nanoparticles. *Physical Review B* **2005,** *72*, 241403.
119. Bosman, M.; Ye, E.; Tan, S. F.; Nijhuis, C. A.; Yang, J. K. W.; Marty, R.; Mlayah, A.; Arbouet, A.; Girard, C.; Han, M.-Y., Surface Plasmon Damping Quantified with an Electron Nanoprobe. *Sci. Rep.* **2013,** *3*.

120. Zuloaga, J.; Prodan, E.; Nordlander, P., Quantum Description of the Plasmon Resonances of a Nanoparticle Dimer. *Nano Letters* **2009,** *9*, 887-891.
121. Liljeroth, P.; Overgaag, K.; Urbieta, A.; Grandidier, B.; Hickey, S. G.; Vanmaekelbergh, D., Variable Orbital Coupling in a Two-Dimensional Quantum-Dot Solid Probed on a Local Scale. *Physical Review Letters* **2006,** *97*, 096803.
122. Williams, K. J.; Tisdale, W. A.; Leschkies, K. S.; Haugstad, G.; Norris, D. J.; Aydil, E. S.; Zhu, X. Y., Strong Electronic Coupling in Two-Dimensional Assemblies of Colloidal PbSe Quantum Dots. *ACS Nano* **2009,** *3*, 1532-1538.
123. Ahn, C. C., *Transmission Electron Energy Loss Spectroscopy in Materials Science and EELS Atlas*. Wiley: 2004.
124. Mittal, A.; Mkhoyan, K. A., Limits in detecting an individual dopant atom embedded in a crystal. *Ultramicroscopy* **2011,** *111*, 1101-1110.
125. Mittal, A.; Zhang, D. B.; Teresi, C.; Dumitrică, T.; Mkhoyan, K. A., Routes to identification of intrinsic twist in helical MoS_2 nanotubes by electron diffraction and annular dark-field scanning transmission electron microscopy imaging. *Physical Review B* **2011,** *84*, 153401.
126. Odlyzko, M. L.; Mkhoyan, K. A., Identifying Hexagonal Boron Nitride Monolayers by Transmission Electron Microscopy. *Microscopy and Microanalysis* **2012,** *18*, 558-567.
127. Howie, A.; Whelan, M. J., Diffraction Contrast of Electron Microscope Images of Crystal Lattice Defects. II. The Development of a Dynamical Theory. *Proceedings of the Royal Society of London. Series A. Mathematical and Physical Sciences* **1961,** *263*, 217-237.
128. Cowley, J. M.; Moodie, A. F., The scattering of electrons by atoms and crystals. I. A new theoretical approach. *Acta Crystallographica* **1957,** *10*, 609-619.
129. Lynch, D. F.; O'Keefe, M. A., n-Beam lattice images. II. Methods of calculation. *Acta Crystallographica Section A* **1972,** *28*, 536-548.
130. Loane, R. F.; Xu, P.; Silcox, J., Thermal vibrations in convergent-beam electron diffraction. *Acta Crystallographica Section A* **1991,** *47*, 267-278.
131. Howie, A., Hunting the Stobbs factor. *Ultramicroscopy* **2004,** *98*, 73-79.
132. Xu, P.; Loane, R. F.; Silcox, J., Energy-filtered convergent-beam electron diffraction in STEM. *Ultramicroscopy* **1991,** *38*, 127-133.
133. Mkhoyan, K. A.; Maccagnano-Zacher, S. E.; Thomas, M. G.; Silcox, J., Critical Role of Inelastic Interactions in Quantitative Electron Microscopy. *Physical Review Letters* **2008,** *100*, 025503.
134. Lee, Z.; Rose, H.; Hambach, R.; Wachsmuth, P.; Kaiser, U., The influence of inelastic scattering on EFTEM images—exemplified at 200 kV for graphene and silicon. *Ultramicroscopy*.

135. Gunawan, A. A.; Mkhoyan, K. A.; Wills, A. W.; Thomas, M. G.; Norris, D. J., Imaging "Invisible" Dopant Atoms in Semiconductor Nanocrystals. *Nano Letters* **2011,** *11*, 5553-5557.
136. Asenov, A.; Brown, A. R.; Davies, J. H.; Kaya, S.; Slavcheva, G., Simulation of intrinsic parameter fluctuations in decananometer and nanometer-scale MOSFETs. *Electron Devices, IEEE Transactions on* **2003,** *50*, 1837-1852.
137. Koenraad, P. M.; Flatté, M. E., Single dopants in semiconductors. *Nature Mater.* **2011,** *10*, 91.
138. Hoeneise, B.; Mead, C. A., Fundamental limitations in microelectronics. 1. MOS technology. *Solid State Electron.* **1972,** *15*, 819.
139. Klimov, V. I., *Nanocrystal Quantum Dots*. 2nd ed.; CRC Press: Boca Raton, 2010.
140. Klimov, V. I.; Ivanov, S. A.; Nanda, J.; Achermann, M.; Bezel, I.; McGuire, J. A.; Piryatinski, A., Single-exciton optical gain in semiconductor nanocrystals. *Nature* **2007,** *447*, 441-446.
141. Michalet, X.; Pinaud, F. F.; Bentolila, L. A.; Tsay, J. M.; Doose, S.; Li, J. J.; Sundaresan, G.; Wu, A. M.; Gambhir, S. S.; Weiss, S., Quantum dots for live cells, in vivo imaging, and diagnostics. *Science* **2005,** *307*, 538-544.
142. Gur, I.; Fromer, N. A.; Geier, M. L.; Alivisatos, A. P., Air-stable all-inorganic nanocrystal solar cells processed from solution. *Science* **2005,** *310*, 462-465.
143. Hoffman, D. M.; Meyer, B. K.; Ekimov, A. I.; Merkulov, I. A.; Al. L. Efros; Rosen, M.; Couino, G.; Gacoin, T.; Boilot, J. P., Giant internal magnetic fields in Mn doped nanocrystal quantum dots. *Solid State Commun.* **2000,** *114*, 547-550.
144. Norris, D. J.; Yao, N.; Charnock, F. T.; Kennedy, T. A., High quality manganese-doped ZnSe nanocrystals. *Nano Lett.* **2001,** *1*, 3-7.
145. Bussian, D. A.; Crooker, S. A.; Yin, M.; Brynda, M.; Efros, A. L.; Klimov, V. I., Tunable magnetic exchange interactions in manganese-doped inverted core-shell ZnSe-CdSe nanocrystals. *Nature Mater.* **2009,** *8*, 35-40.
146. Beaulac, R.; Schneider, L.; Archer, P. I.; Bacher, G.; Gamelin, D. R., Light-Induced Spontaneous Magnetization in Doped Colloidal Quantum Dots. *Science* **2009,** *325*, 973-976.
147. Bryan, J. D.; Gamelin, D. R., Doped semiconductor nanocrystals: synthesis, characterization, physical properties, and applications. *Prog. Inorg. Chem.* **2005,** *54*, 47-126.
148. Norris, D. J.; Al. L. Efros; Erwin, S. C., Doped nanocrystals. *Science* **2008,** *319*, 1776-1779.
149. Johnson, M. B.; Albrektsen, O.; Feenstra, R. M.; Salemink, H. W. M., DIRECT IMAGING OF DOPANTS IN GAAS WITH CROSS-SECTIONAL SCANNING-TUNNELING-MICROSCOPY. *Appl. Phys. Lett.* **1993,** *63*, 2923-2925.
150. Perea, D. E.; Allen, J. E.; May, S. J.; Wessels, B. W.; Seidman, D. N.; Lauhon, L. J., Three-dimensional nanoscale composition mapping of semiconductor nanowires. *Nano Lett.* **2006,** *6*, 181-185.

151. Pennycook, S. J.; Boatner, L. A., CHEMICALLY SENSITIVE STRUCTURE-IMAGING WITH A SCANNING-TRANSMISSION ELECTRON-MICROSCOPE. *Nature* **1988,** *336*, 565-567.
152. Batson, P. E.; Dellby, N.; Krivanek, O. L., Sub-angstrom resolution using aberration corrected electron optics. *Nature* **2002,** *418*, 617-620.
153. Nellist, P. D.; Chisholm, M. F.; Dellby, N.; Krivanek, O. L.; Murfitt, M. F.; Szilagyi, Z. S.; Lupini, A. R.; Borisevich, A.; Sides, W. H.; Pennycook, S. J., Direct sub-angstrom imaging of a crystal lattice. *Science* **2004,** *305*, 1741-1741.
154. Voyles, P. M.; Muller, D. A.; Grazul, J. L.; Citrin, P. H.; Gossmann, H. J. L., Atomic-scale imaging of individual dopant atoms and clusters in highly n-type bulk Si. *Nature* **2002,** *416*, 826-829.
155. Shibata, N.; Findlay, S. D.; Azuma, S.; Mizoguchi, T.; Yamamoto, T.; Ikuhara, Y., Atomic-scale imaging of individual dopant atoms in a buried interface. *Nature Mater.* **2009,** *8*, 654-658.
156. Krivanek, O. L.; Chisholm, M. F.; Nicolosi, V.; Pennycook, T. J.; Corbin, G. J.; Dellby, N.; Murfitt, M. F.; Own, C. S.; Szilagyi, Z. S.; Oxley, M. P.; Pantelides, S. T.; Pennycook, S. J., Atom-by-atom structural and chemical analysis by annular dark-field electron microscopy. *Nature* **2010,** *464*, 571-574.
157. Zu, L.; Wills, A. W.; Kennedy, T. A.; Glaser, E. R.; Norris, D. J., Effect of different manganese precursors on the doping efficiency in ZnSe nanocrystals. *J. Phys. Chem. C* **2010,** *114*, 21969-21975.
158. Dellby, N.; Krivanek, O. L.; Nellist, P. D.; Batson, P. E.; Lupini, A. R., *J. Electron Microsc.* **2001,** *50*, 177.
159. Krivanek, O. L.; Nellist, P. D.; Dellby, N.; Murfitt, M. F.; Szilagyi, Z., *Ultramicroscopy* **2003,** *96*, 229.
160. Baston, P. E., *Ultramicroscopy* **2003,** *96*, 239.
161. Maccagnano, S.; Mkhoyan, K. A.; Calcines, J.; Krauss, T. D.; Silcox, J., *Microsc. microanal.* **2006,** *12*, 498.
162. Daniels, J.; Festenberg, C. V.; Raether, H.; Zeppenfeld, K., Optical Constants of Solids by Electron Spectroscopy. In *Springer Tracts in Modern Physics*, Hohler, G., Ed. Springer-Verlag: Berlin, 1970; Vol. 54, pp 77-135.
163. Suenaga, K.; Sato, Y.; Liu, Z.; Kataura, H.; Okazaki, T.; Kimoto, K.; Sawada, H.; Sasaki, T.; Omoto, K.; Tomita, T.; Kaneyama, T.; Kondo, Y., Visualizing and identifying single atoms using electron energy-loss spectroscopy with low accelerating voltage. *Nature Chem.* **2009,** *1*, 415-418.
164. Suenaga, K.; Koshino, M., Atom-by-atom spectroscopy at graphene edge. *Nature* **2010,** *468*, 1088-1090.
165. Egerton, R. F., *Electron Energy Loss Spectroscopy in the Electron Microscope*. 2nd ed.; Plenum Press: New York, 1996.
166. Krivanek, O. L.; Dellby, N.; Murfitt, M. F.; Chisholm, M. F.; Pennycook, T. J.; Suenaga, K.; Nicolosi, V., Gentle STEM: ADF imaging and EELS at low primary energies. *Ultramicroscopy* **2010,** *110*, 935-945.

167. Press, W. H.; Teukolsky, S. A.; Vetterling, W. T.; Flannery, B. P., *Numerical Recipes: The Art of Scientific Computing*. 3rd ed.; Cambridge University Press: New York, 2007.
168. Note9A *Nagpal 3: Note to online material*; 2009.
169. Loane, R. F.; Xu, P. R.; Silcox, J., *Acta Crystallogr.* **1991,** *A 47*, 267.
170. Inokuti, M., Inelastic collisions of fast charged particles with atoms and molecules - Bethe theory revisited. *Rev. Mod. Phys.* **1971,** *43*, 297.
171. Cohen-Tannoudji, C.; Diu, B.; Laloë, F., *Quantum Mechanics*. John Wiley & Sons: New York, 1977.
172. Konstantatos, G.; Howard, I.; Fischer, A.; Hoogland, S.; Clifford, J.; Klem, E.; Levina, L.; Sargent, E. H., Ultrasensitive solution-cast quantum dot photodetectors. *Nature* **2006,** *442*, 180-183.
173. Sun, L.; Choi, J. J.; Stachnik, D.; Bartnik, A. C.; Hyun, B.-R.; Malliaras, G. G.; Hanrath, T.; Wise, F. W., Bright infrared quantum-dot light-emitting diodes through inter-dot spacing control. *Nature Nanotech* **2012,** *7*, 369-373.
174. Somers, R. C.; Bawendi, M. G.; Nocera, D. G., CdSe nanocrystal based chem-/bio- sensors. *Chem. Soc. Rev.* **2007,** *36*, 579-591.
175. Murphy, J. E.; Beard, M. C.; Nozik, A. J., Time-Resolved Photoconductivity of PbSe Nanocrystal Arrays. *J. Phys. Chem. B* **2006,** *110*, 25455-25461.
176. Tang, J.; Kemp, K. W.; Hoogland, S.; Jeong, K. S.; Liu, H.; Levina, L.; Furukawa, M.; Wang, X.; Debnath, R.; Cha, D.; Chou, K. W.; Fischer, A.; Amassian, A.; Asbury, J. B.; Sargent, E. H., Colloidal-quantum-dot photovoltaics using atomic-ligand passivation. *Nature Mater.* **2011,** *10*, 765-771.
177. Law, M.; Luther, J. M.; Song, Q.; Hughes, B. K.; Perkins, C. L.; Nozik, A. J., Structural, Optical, and Electrical Properties of PbSe Nanocrystal Solids Treated Thermally or with Simple Amines. *J. Am. Chem. Soc.* **2008,** *130*, 5974-5985.
178. Luther, J. M.; Law, M.; Song, Q.; Perkins, C. L.; Beard, M. C.; Nozik, A. J., Structural, Optical, and Electrical Properties of Self-Assembled Films of PbSe Nanocrystals Treated with 1,2-Ethanedithiol. *ACS Nano* **2008,** *2*, 271-280.
179. Hanrath, T.; Veldman, D.; Choi, J. J.; Christova, C. G.; Wienk, M. M.; Janssen, R. A. J., PbSe Nanocrystal Network Formation during Pyridine Ligand Displacement. *ACS Appl. Mater. Interfaces* **2009,** *1*, 244-250.
180. Talapin, D. V.; Murray, C. B., PbSe Nanocrystal Solids for n- and p-Channel Thin Film Field-Effect Transistors. *Science* **2005,** *310*, 86-89.
181. Ellingson, R. J.; Beard, M. C.; Johnson, J. C.; Yu, P.; Micic, O. I.; Nozik, A. J.; Shabaev, A.; Efros, A. L., Highly Efficient Multiple Exciton Generation in Colloidal PbSe and PbS Quantum Dots. *Nano Lett.* **2005,** *5*, 865-871.
182. Luther, J. M.; Beard, M. C.; Song, Q.; Law, M.; Ellingson, R. J.; Nozik, A. J., Multiple Exciton Generation in Films of Electronically Coupled PbSe Quantum Dots. *Nano Lett.* **2007,** *7*, 1779-1784.

183. Beard, M. C.; Midgett, A. G.; Law, M.; Semonin, O. E.; Ellingson, R. J.; Nozik, A. J., Variations in the Quantum Efficiency of Multiple Exciton Generation for a Series of Chemically Treated PbSe Nanocrystal Films. *Nano Lett.* **2009,** *9*, 836-845.
184. Kim, S. J.; Kim, W. J.; Sahoo, Y.; Cartwright, A. N.; Prasad, P. N., Multiple exciton generation and electrical extraction from a PbSe quantum dot photoconductor. *Appl. Phys. Lett.* **2008,** *92*, 031107-3.
185. Stouwdam, J. W.; Shan, J.; van Veggel, F. C. J. M.; Pattantyus-Abraham, A. G.; Young, J. F.; Raudsepp, M., Photostability of Colloidal PbSe and PbSe/PbS Core/Shell Nanocrystals in Solution and in the Solid State. *J. Phys. Chem. C* **2006,** *111*, 1086-1092.
186. Sapra, S.; Nanda, J.; Pietryga, J. M.; Hollingsworth, J. A.; Sarma, D. D., Unraveling Internal Structures of Highly Luminescent PbSe Nanocrystallites Using Variable-Energy Synchrotron Radiation Photoelectron Spectroscopy. *J. Phys. Chem. B* **2006,** *110*, 15244-15250.
187. Kaushik, A. P.; Clancy, P., Explicit all-atom modeling of realistically sized ligand-capped nanocrystals. *J Chem. Phys.* **2012,** *136*, 114702-12.
188. Moreels, I.; Fritzinger, B.; Martins, J. C.; Hens, Z., Surface Chemistry of Colloidal PbSe Nanocrystals. *J. Am. Chem. Soc.* **2008,** *130*, 15081-15086.
189. Chu, M.-W.; Myroshnychenko, V.; Chen, C. H.; Deng, J.-P.; Mou, C.-Y.; García de Abajo, F. J., Probing Bright and Dark Surface-Plasmon Modes in Individual and Coupled Noble Metal Nanoparticles Using an Electron Beam. *Nano Lett.* **2008,** *9*, 399-404.
190. Koh, A. L.; Bao, K.; Khan, I.; Smith, W. E.; Kothleitner, G.; Nordlander, P.; Maier, S. A.; McComb, D. W., Electron Energy-Loss Spectroscopy (EELS) of Surface Plasmons in Single Silver Nanoparticles and Dimers: Influence of Beam Damage and Mapping of Dark Modes. *ACS Nano* **2009,** *3*, 3015-3022.
191. Moreels, I.; Lambert, K.; De Muynck, D.; Vanhaecke, F.; Poelman, D.; Martins, J. C.; Allan, G.; Hens, Z., Composition and Size-Dependent Extinction Coefficient of Colloidal PbSe Quantum Dots. *Chem. Mater.* **2007,** *19*, 6101-6106.
192. Fan, X.; Dickey, E. C.; Pennycook, S. J.; Sunkara, M. K., Z-contrast imaging and electron energy-loss spectroscopy analysis of chromium-doped diamond-like carbon films. *Appl. Phys. Lett.* **1999,** *75*, 2740-2742.
193. Sykora, M.; Koposov, A. Y.; McGuire, J. A.; Schulze, R. K.; Tretiak, O.; Pietryga, J. M.; Klimov, V. I., Effect of Air Exposure on Surface Properties, Electronic Structure, and Carrier Relaxation in PbSe Nanocrystals. *ACS Nano* **2010,** *4*, 2021-2034.
194. Leschkies, K. S.; Kang, M. S.; Aydil, E. S.; Norris, D. J., Influence of Atmospheric Gases on the Electrical Properties of PbSe Quantum-Dot Films. *J. Phys. Chem. C* **2010,** *114*, 9988-9996.
195. Moreels, I.; Allan, G.; De Geyter, B.; Wirtz, L.; Delerue, C.; Hens, Z., Dielectric function of colloidal lead chalcogenide quantum dots obtained by a

Kramers-Krönig analysis of the absorbance spectrum. *Phys. Rev. B* **2010,** *81*, 235319.
196. Eberlein, T.; Bangert, U.; Nair, R. R.; Jones, R.; Gass, M.; Bleloch, A. L.; Novoselov, K. S.; Geim, A.; Briddon, P. R., Plasmon spectroscopy of free-standing graphene films. *Phys. Rev. B* **2008,** *77*, 233406.
197. Hunt, M. R. C.; Rudolf, P.; Modesti, S., Photoemission and electron-energy-loss-spectroscopy study of C_{60} monolayers adsorbed on Cs-precovered Au(110) and of bulk distilled Cs_xC_{60}. *Phys. Rev. B* **1997,** *55*, 7889-7903.
198. Fukudome, K.; Ikenaga, N.-o.; Miyake, T.; Suzuki, T., Oxidative dehydrogenation of propane using lattice oxygen of vanadium oxides on silica. *Catal. Sci. Tech.* **2011,** *1*, 987-998.
199. Botella, P.; García-González, E.; Dejoz, A.; López Nieto, J. M.; Vázquez, M. I.; González-Calbet, J., Selective oxidative dehydrogenation of ethane on MoVTeNbO mixed metal oxide catalysts. *J. Catal.* **2004,** *225*, 428-438.
200. Buist, P. H., Fatty acid desaturases: selecting the dehydrogenation channel. *Natural Product Reports* **2004,** *21*, 249-262.
201. Bryant, G. W.; Jaskolski, W., Surface Effects on Capped and Uncapped Nanocrystals. *J. Phys. Chem. B* **2005,** *109*, 19650-19656.
202. Anatoliy, P.; Uwe, K., Interface decay channel of particle surface plasmon resonance. *New J. Phys.* **2003,** *5*, 151.
203. Zuloaga, J.; Prodan, E.; Nordlander, P., Quantum Description of the Plasmon Resonances of a Nanoparticle Dimer. *Nano Lett.* **2009,** *9*, 887-891.
204. Liljeroth, P.; Vanmaekelbergh, D.; Ruiz, V.; Kontturi, K.; Jiang, H.; Kauppinen, E.; Quinn, B. M., Electron Transport in Two-Dimensional Arrays of Gold Nanocrystals Investigated by Scanning Electrochemical Microscopy. *J. Am. Chem. Soc.* **2004,** *126*, 7126-7132.
205. Mitome, M.; Yamazaki, Y.; Takagi, H.; Nakagiri, T., Size dependence of plasmon energy in Si clusters. *J. Appl. Phys.* **1992,** *72*, 812-814.
206. Chen, K.-P.; Drachev, V. P.; Borneman, J. D.; Kildishev, A. V.; Shalaev, V. M., Drude Relaxation Rate in Grained Gold Nanoantennas. *Nano Lett.* **2010,** *10*, 916-922.
207. Büchner, U., Wave-vector dependence of the electron energy losses of PbS, PbSe, and PbTe. *Phys. Status Solidi B* **1977,** *83*, 493-500.

Appendix

A Modified Inelastic-Elastic *Multislice* Code

Sample modified source codes of the inelastic elastic *Multislice* algorithm are shown in the following pages. These codes are part of the autostem.c source codes developed by Earl Kirkland which calculates the modified transmission and propagation with the inclusion of plasmon scattering. The codes calculating the plasmon cross section are not shown.

```
for( ip=0; ip<npos; ip++) {
    for(iE=0;iE<nE;iE++){ /* new line */
       /* apply transmission function if there are atoms in this slice */
       if( na > 0 ) {
            if (iE!=0 ){
                if( nslice == 0){
                    for( ix=0; ix<nxprobe; ix++){
                        j=ix*nyprobe;
                        for( iy=0; iy<nyprobe; iy++){
                            probe[ip][iy+j][0]=amp[ip][iy + j]*cos(phase[ip][0][iy+j]);
                            probe[ip][iy+j][1]=amp[ip][iy + j]*sin(phase[ip][0][iy+j]);
                        }
                    }
                }
                fftwf_execute_dft( planPi, probe[ip], probe[ip] );
                scaleW( probe[ip], nxprobe, nyprobe );

                for( ix=0; ix<nxprobe; ix++){
                    j=ix*nyprobe;
                    for( iy=0; iy<nyprobe; iy++){
                        waveoutr[ip][iE][iy+j]=(float)(betaSi1*probe[ip][iy+j][0]*fbulk[iE][iy+j][0]);
                        waveouti[ip][iE][iy+j]=(float)(betaSi1*probe[ip][iy+j][1]*fbulk[iE][iy+j][0]);

                    }
                }
                fftwf_execute_dft( planPf, probe[ip], probe[ip] );
                for( ix=0; ix<nxprobe; ix++){
                    j=ix*nyprobe;
                    for( iy=0; iy<nyprobe; iy++){
                            probe[ip][iy+j][0]=probeADFr[ip][iE][iy+j];
                            probe[ip][iy+j][1]=probeADFi[ip][iE][iy+j];
                    }
                }
                fftwf_execute_dft( planPi, probe[ip], probe[ip] );
                scaleW( probe[ip], nxprobe, nyprobe );

                for( ix=0; ix<nxprobe; ix++){
                    j=ix*nyprobe;
                    for( iy=0; iy<nyprobe; iy++){
                        probedoubamprs[ip][iE][iy+j]=probe[ip][iy+j][0];
                        probedoubampis[ip][iE][iy+j]=probe[ip][iy+j][1];
```

```
                if (nslice == 0){
                    probe[ip][iy+j][0]=(float)(waveoutr[ip][iE][iy+j]);
                    probe[ip][iy+j][1]=(float)(waveouti[ip][iE][iy+j]);
                }
                else {
                    for (iEnergy=1;iEnergy<iE;iEnergy++){
                        if (iEnergy < iE  && (iE-iEnergy)<30 ){
                            waveoutr[ip][iE][iy+j]+=(float)(betaSi2
                            *probedoubamprs[ip][iEnergy][iy+j]*fbulk[iE-iEnergy][iy+j][0]);
                            waveouti[ip][iE][iy+j]+=(float)(betaSi2
                            *probedoubampis[ip][iEnergy][iy+j]*fbulk[iE-iEnergy][iy+j][0]);

                        }
                    }
                    probe[ip][iy+j][0]=(float)(betaSiel*probe[ip][iy+j][0]+waveoutr[ip][iE][iy+j]);
                    probe[ip][iy+j][1]=(float)(betaSiel*probe[ip][iy+j][1]+waveouti[ip][iE][iy+j]);
                }

            }
        }
        fftwf_execute_dft( planPf, probe[ip], probe[ip] );
    }

    if (iE == 0){
        for( ix=0; ix<nxprobe; ix++){
            j=ix*nyprobe;
            for( iy=0; iy<nyprobe; iy++){
                probe[ip][iy+j][0]*=(float)(betaSiel);
                probe[ip][iy+j][1]*=(float)(betaSiel);
            }
        }
    }
    fftwf_execute_dft( planPi, probe[ip], probe[ip] );
    scaleW( probe[ip], nxprobe, nyprobe );
    for( ix=0; ix<nxprobe; ix++) {
        ixt = ix + ixoff[ip];
        if( ixt >= nx ) ixt = ixt - nx;
        else if( ixt < 0 ) ixt = ixt + nx;
        j = ix*nyprobe;
        jt = ixt*ny;
        for( iy=0; iy<nyprobe; iy++) {
```

```
                        iyt = iy + iyoff[ip];
                        if( iyt >= ny ) iyt = iyt - ny;
                        else if( iyt < 0 ) iyt = iyt + ny;
                        prr = probe[ip][iy + ix*nyprobe][0];
                        pri = probe[ip][iy + ix*nyprobe][1];
                        probe[ip][iy+j][0] =  prr*trans[iyt+jt][0]
                                            - pri*trans[iyt+jt][1];  /* real */
                        probe[ip][iy+j][1] =  prr*trans[iyt+jt][1]
                                            + pri*trans[iyt+jt][0];  /* imag */
                    } /* end for(iy...) */
                }  /* end for(ix...) */
                fftwf_execute_dft( planPf, probe[ip], probe[ip] );
            }
             /*  multiplied by the propagator function */
             propagateW( probe[ip], propxr, propxi, propyr, propyi,
                 kxp2, kyp2, (float)k2maxp, nxprobe, nyprobe );
             for( ix=0; ix<nxprobe; ix++){
                 j=ix*nyprobe;
                 for( iy=0; iy<nyprobe; iy++){
                     probeADFr[ip][iE][iy + j] = probe[ip][iy+j][0];
                     probeADFi[ip][iE][iy + j] = probe[ip][iy+j][1];
                     probe[ip][iy+j][0]=probeADFr[ip][0][iy + j];
                     probe[ip][iy+j][1]=probeADFi[ip][0][iy + j];
                     waveoutr[ip][iE][iy+j]=0.0F;
                     waveouti[ip][iE][iy+j]=0.0F;
                 }
             }
        } /*end for (iE =... */
    }  /* end  for( ip=... */
```

B Additional Analysis of Oxidized PbSe Nanocrystal

Two HAADF-STEM images of 2D-arranged nanocrystals which are shown in Figure 6.5a and 6.6a and one additional image are analyzed by putting annular discs with inner diameter of 6.5 nm (the average size of nanocrystals) and the difference between outer and inner diameter of 0.8 nm as shown in Figure B-1. Most of the image intensity from the ligands is confined to within the annulus. There are more images but we chose these three for representations. None of the ligands from images in Figure B-1 and other images not shown form interdigitation, particularly as shown in the partial oxidation case in Figure 2b.

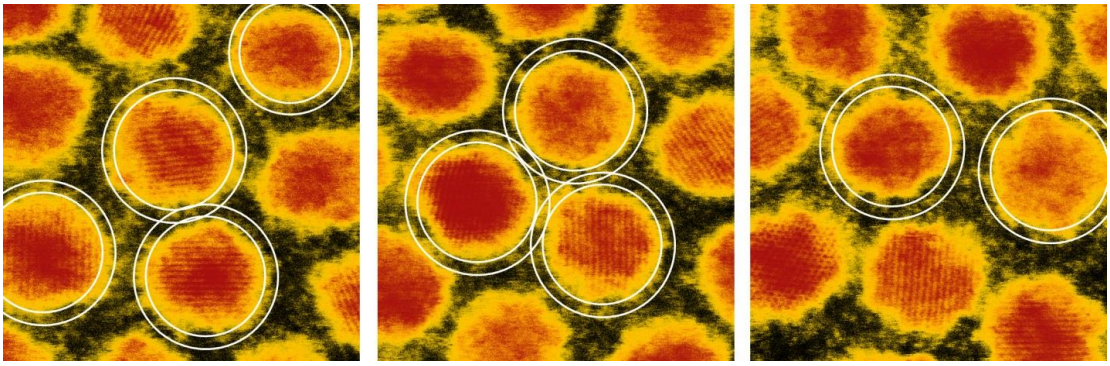

Figure B- 1. Three images for ligand length analysis in as-synthesized nanocrystals. Discs with 0.8 nm annular region are used to quantify the extent of the ligands.

The images after partial and extended oxidization are shown in top and bottom panels of Figure B-2. The same 6.5 nm inner discs are put in the images. The partially oxidized samples have shrunk by less than 0.5 nm indicating that some oxidation has taken place. In the complete oxidation cases (bottom panels), the nanocrystals clearly show a decrease in the size of the nanocrystals of about 0.5 – 1 nm. The images also look blurry due to the presence of oxide shells.

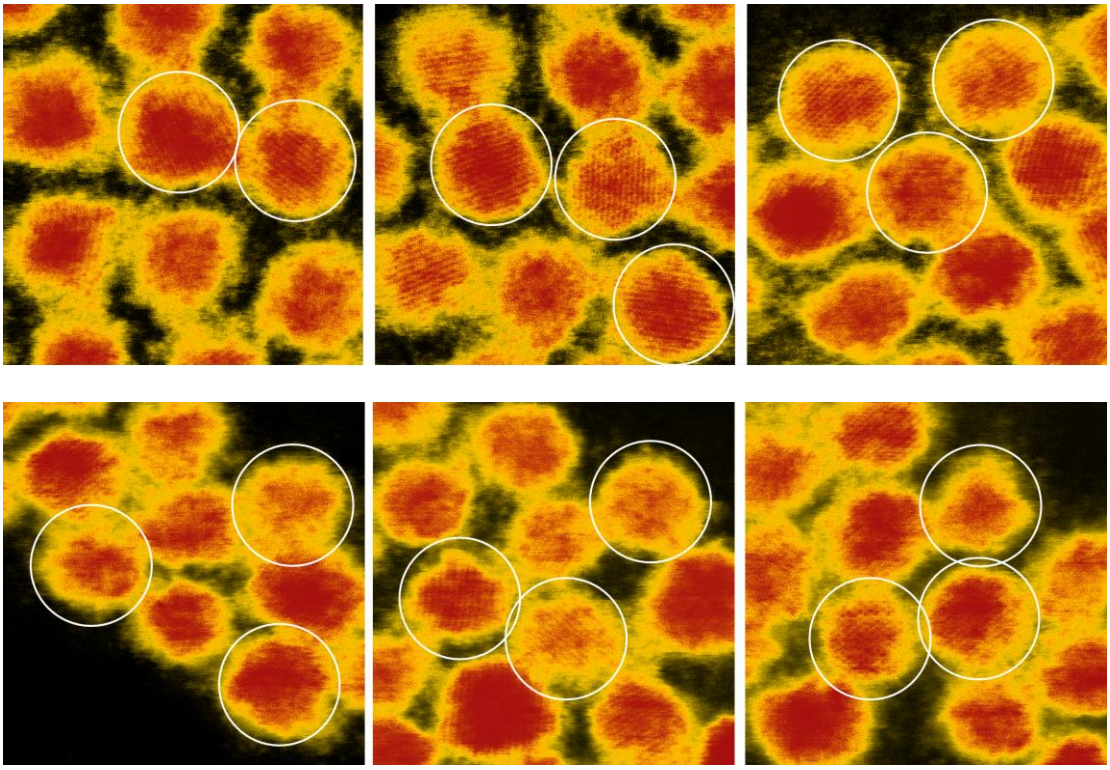

Figure B-2. Three images for ligand length analysis in the partially oxidized (top panel) and completely oxidized (bottom panel) nanocrystals. Discs with 6.5 nm diameter are used to quantify the shrinking size of the nanocrystals.